

Experimental and Theoretical Study of Microwave Heating of Thermal Runaway Materials

by

Xiaofeng Wu, M.S.

Dissertation submitted to the Faculty of the
Virginia Polytechnic Institute and State University
in partial fulfillment of the requirements for the degree of

Doctor of Philosophy

in

Mechanical Engineering

James R. Thomas, Jr., Chair
William A. Davis
William C. Thomas
Elaine P. Scott
David E. Clark

December 2002

Blacksburg, Virginia

Key Words: Microwave processing materials, Thermal runaway, Thermal runaway control

Copyright© 2002, Xiaofeng Wu

Experimental and Theoretical Study of Microwave Heating of Thermal Runaway Materials

Xiaofeng Wu, Ph.D.

Virginia Polytechnic Institute and State University, 2002

Advisor: James R. Thomas, Jr.,

ABSTRACT

There is growing interest in the use of microwaves to process materials. The main application of microwave processing of materials is in heating. The most important characteristic of microwave heating is *volumetric* heating, which is quite different from conventional heating where the heat must diffuse in from the surface of the material. Volumetric heating means that materials can absorb microwave energy directly and internally and convert it to heat. It is this characteristic that leads to advantages such as rapid, controlled, selective, and uniform heating.

However, some problems hinder the widespread use of microwave energy. One of these problems is called thermal runaway, which is a type of thermal instability due to the interaction between the electromagnetic waves and materials. As thermal runaway occurs, the temperature of the heated material rises uncontrollably. The normal consequence of thermal runaway is the damage of the processed materials.

The origins of thermal runaway are different under different processing conditions. When processing ceramic materials, thermal runaway is mainly due to the positive temperature dependence of dielectric loss of the material. These materials absorb more microwave energy as they are being heated. The most plausible explanation of this phenomenon is the so-called "S-curve" theory. However, prior to this work, no direct experimental evidence has been published to verify this theory.

In this dissertation, we report the direct experimental evidence of the so-called "S-curve" by heating thermal runaway materials in a microwave resonant cavity ap-

plicator. A complete discussion of how the experimental results were achieved is presented. From the experimental results, we find that by the use of the cavity effects thermal runaway can be controlled.

To explain the experimental findings, a theoretical model based on equivalent circuit theory is developed. Also, a coupled heat transfer and electromagnetic field model is developed to simulate the heating process. Both models give reasonably good comparison with our experimental results. Finally, a method to control thermal runaway is described.

To my parents, Shen Wu and Duohua Liu.

Acknowledgments

I would like express particular gratitude to my advisor, Dr. James R. Thomas Jr., for his guidance, patience, and advice. During the time I spent at Virginia Tech, once I encountered problems, he was always there to give me help. He opened the door of the microwave world for me. After that, he tried his best to help me, in both experimental and theoretical study. When I discussed questions with him, he always tried to understand what I were saying and then gave me his opinions. Whenever possible, he always provided as many choices as possible to let me choose. As I remembered, he never pushed me to work on anything. When the research was in slow progress, his understanding gave me the most strong encouragement.

I would like to thank Dr. William A. Davis for his guidance on my experimental and theoretical study. As a mechanical engineering student, I knew little of the theory of electromagnetic fields. He kept explaining some concepts to me during these years. His help is essential to my work. Actually, the models we developed in this dissertation mainly came from his original ideas.

I would like to thank Dr. William C. Thomas for his help on setting up and repairing the cooling system in the experiment. I also enjoyed our discussions on other subjects

I would like to thank Dr. Elaine P. Scott and Dr. David E. Clark for serving on my committee.

I would like to thank Dr. Thomas E. Diller. He gave me the opportunity to study at Virginia Tech. Also, he was a member of my committee for almost four years.

I would like to thank Dr. Brian Vick for his help on some mathematical

problems.

I would like to thank Mr. Max Savransky. Our discussion on microwaves, heat transfer and math helped me a lot.

Finally, I want to express special thanks to my wife, Zheng, for her constant support and understanding.

XIAOFENG WU

Virginia Polytechnic Institute and State University

December 2002

Contents

Abstract	ii
Acknowledgments	v
List of Tables	x
List of Figures	xi
Chapter 1 Introduction	1
Chapter 2 Literature Review	8
2.1 Experimental Observations of Thermal Runaway	10
2.2 Theoretical Models to Explain Thermal Runaway	11
2.3 Control of Thermal Runaway	15
2.4 Prior Work at Virginia Tech	16
2.5 Research Objective	17
Chapter 3 Microwave Power Absorption	18
3.1 A uniform plane wave traveling in half infinite space	19
3.2 A TE_{10} wave traveling in waveguide to heat a finite size material . . .	21
Chapter 4 Experiment Setup	33
4.1 Overall System	33
4.2 Electric Field Measurement	35
4.3 The Short with a Spin Dial	37

4.4	Cavity	37
4.5	Data Acquisition	42
Chapter 5 Experimental Results		43
5.1	Experimental Results for 4.5 mm Mullite Rod	43
5.1.1	Typical Heating Processes	46
5.2	Experimental Results for 4.5 mm Alumina Rod	49
5.3	Power Level Effects	49
5.4	Rod Size Effects	50
5.5	Summary	51
Chapter 6 Equivalent Circuit Model for the Microwave Heating System		54
6.1	S-matrix Simplifications	55
6.2	Equivalent Circuit for a Two-port Microwave Network	58
6.3	Analysis of the Cavity from an Equivalent Circuit Viewpoint	62
6.4	The Equivalent Circuit for the Microwave Heating System	64
Chapter 7 Computation of the Electric Field in the Cavity		67
7.1	Iris Problem	67
7.1.1	Integral equation	70
7.1.2	Moment methods	75
7.1.3	Solutions	80
7.2	Electric Field in the Rod	84
7.2.1	Orthogonal expansion method	85
7.2.2	Line source approximation	100
Chapter 8 Interpretation of the Experimental Results		116
8.1	Equivalent Circuit Model	116
8.2	Numerical Model	123
8.2.1	S-shaped curve	125
8.2.2	Temperature and electric field distribution in the rod	127

Chapter 9 Summary, Conclusions and Recommendations	132
9.1 Summary	132
9.2 Conclusions	138
9.3 Recommendations	138
Vita	148

List of Tables

3.1	Properties and parameters of materials	31
4.1	The relation between dial reading and cavity length	37
7.1	Computation results for a double step iris by FEM	83

List of Figures

2.1	Stability analysis using S-shaped curve	12
3.1	A slab heated by the TE ₁₀ mode in a waveguide.	22
3.2	Variation of phase constant and attenuation constant with dielectric constant.	25
3.3	Variation of absorbed power with dielectric constant, where $A_1 = 1$, $B_3 = 0$, and $d = 1$ cm.	26
3.4	Effect of phase constant on power density distribution in the slab, where $A_1 = 1$, $B_3 = 0$, and $d = 1$ cm.	27
3.5	Variation of phase constant and attenuation constant with loss factor.	28
3.6	Variation of absorbed power with loss factor, where $A_1 = 1$, $B_3 = 0$, and $d = 1$ cm.	29
3.7	Variation of average dissipated power density with slab thickness. The relative complex permittivities of beef and Al ₂ O ₃ are 30.5-9.60j and 9.5-0.0009j, respectively.	30
3.8	Comparison of dissipated power density along slab. In the E case, $A_1 = 1$ and $B_3 = 1$; In the H case, $A_1 = 1$ and $B_3 = -1$	31
3.9	f_1 , f_2 and \bar{p} for Al ₂ O ₃ in the E case and H case. The relative complex permittivity of Al ₂ O ₃ is 9.5-0.0009j. f_1 and f_2 are measures of the electric and magnetic fields at the center of the slab, respectively.	32
3.10	f_1 , f_2 and \bar{p} for beef in the E case and H case. The relative complex permittivity of beef is 30.5-9.60j. f_1 and f_2 are measures of the electric and magnetic fields at the center of the slab, respectively.	32

3.11	f_1 , f_2 and \bar{p} for an imaginary material in the E case and H case. The relative complex permittivity of this imaginary material is 1-j1000. f_1 and f_2 are measures of the electric and magnetic fields at the center of the slab, respectively.	32
4.1	Schematic of experimental setup (top view). (1) Power Source; (2) Magnetron; (3) Circulator; (4) Water Load; (5) Waveguide Extension; (6) Four Stub Tuner; (7) Impedance Analyzer; (8) Waveguide with Wedge; (9) Iris; (10) Power Meter for Electric Field Measurement (11) Cavity; (12) Sample; (13) Pyrometer; (14) Adjustable End-wall Short.	34
4.2	Schematic of TE ₁₀₃ mode cavity.	35
4.3	Equipment setup for electric field calibration. (1) Power Source; (2) Magnetron; (3) Circulator; (4) Water Load; (5) Waveguide Extension; (7) Impedance Analyzer; (10) Power Meter for Electric Field Measurement (11) Cavity; (15) Steel load.	36
4.4	Cavity. (1) Location to measure electric field; (2) Location to insert heated rods; (3) Location of the short plane such that the cavity length is minimum; (4) Location of the short plane such that the cavity length is maximum.	38
4.5	A single mode cavity	39
4.6	Cavity: multiple reflection viewpoint	40
4.7	Peak electric field inside the cavity varied with the cavity length . . .	41
5.1	Behavior of the rod temperature when the position of the shorting plane was adjusted. In the figure, the stable states obtained by decreasing and increasing the cavity length are denoted by the “ × ” and “ o ” symbols, respectively.	44
5.2	Behavior of the electric field for the same experiment shown in Figure 5.1.	45
5.3	Plot of the temperature versus electric field for a mullite rod with a 4.5 mm diameter heated at 600 W.	46

5.4	The transient behavior of electric field and temperature for decreasing cavity length. This behavior is illustrated for two different starting points. The arrows illustrate the dynamic heating process observed in the experiments.	47
5.5	The transient behavior of electric field and temperature for increasing cavity length. This behavior is illustrated for two different starting points. The arrows illustrate the dynamic heating process observed in the experiments.	48
5.6	Behavior of the electric field and temperature when the cavity length is increased from critical point <i>c</i> . The temperature excursion mimics thermal runaway, but a stable equilibrium point is achieved at high temperature.	49
5.7	Rapid temperature decrease following a decrease in cavity length from critical point <i>b</i>	50
5.8	Behavior of the alumina rod temperature and the electric field when the position of the shorting plane was adjusted. In the figure, the stable states obtained by decreasing and increasing the cavity length are denoted by the “ × ” and “ o ” symbols, respectively.	51
5.9	Plot of the temperature versus electric field for an alumina rod with a 4.5 mm diameter heated at 300 W. In the figure, the stable states obtained by decreasing and increasing the cavity length are denoted by the “ × ” and “ o ” symbols, respectively.	52
5.10	Part of the middle branch of the S-curve becomes unstable when heating the mullite rod with 2000 W input power. In the figure, the stable states obtained by decreasing and increasing the cavity length are denoted by the “ × ” and “ o ” symbols, respectively.	52
5.11	The middle branch of the S-curve becomes unstable when heating the alumina rod with 700 W input power. In the figure, the stable states obtained by decreasing and increasing the cavity length are denoted by the “ × ” and “ o ” symbols, respectively.	53

5.12	Plot of the temperature versus electric field for an alumina rod with a 9.0 mm diameter.	53
6.1	Cavity	55
6.2	Imaginary Plane	56
6.3	An arbitrary obstacle in the waveguide	59
6.4	An equivalent circuit for a two-port microwave network	61
6.5	Cavity: transmission line model	62
6.6	The equivalent circuit for the microwave heating system. In the model, the incident electric field is assumed to be a constant during the heating process.	64
6.7	Four planes are defined in the equivalent circuit model. In the model, the incident electric field is assumed to be a constant during the heating process.	65
7.1	The iris used in the experiment	68
7.2	Capacitive Iris	68
7.3	Inductive Iris	69
7.4	Double Step Iris	70
7.5	Inductive Iris - An Example	76
7.6	The reactance of the double step iris	82
7.7	The geometry of the computation region	84
7.8	Meshing result	84
7.9	Geometry of the rod and waveguide	86
7.10	Dielectric property of mullite	96
7.11	Comparison of the normalized impedance z_b	97
7.12	Comparison of the normalized impedance z_c	98
7.13	Electric field (y component) inside a cavity.	99
7.14	Electric field (y component) around the rod.	100
7.15	Comparison of the fields calculated by different methods.	101
7.16	Comparison of the local fields calculated by different methods.	102

7.17	Comparison of the electric field at $\rho=0$ calculated by different methods.	103
7.18	Comparison of the fields calculated by different methods.	104
7.19	Comparison of the local fields calculated by different methods.	105
7.20	Comparison of the electric field at $\rho=0$ calculated by different methods.	106
7.21	Electric field variation along ρ direction inside the rod.	107
7.22	Electric field variation along ϕ direction inside the rod.	108
7.23	Comparison of the convergence rate by different summation methods.	112
7.24	Comparison of the electric field at $\rho=0$ calculated by OEM and line source methods.	113
7.25	Comparison of the electric field at $\rho=0$ calculated by OEM and line source methods.	114
8.1	The equivalent circuit for the microwave heating system	117
8.2	Four planes in the equivalent circuit model	117
8.3	The variation of the electric field in the rod with the temperature and L_2	118
8.4	Behavior of electric field and temperature for decreasing cavity length. The dashed curve is the experimentally obtained S-shaped curve of the mullite rod, while the solid curves represent the electric field solutions at fixed cavity length.	119
8.5	Behavior of electric field and temperature for increasing cavity length. The dashed curve is the experimentally obtained S-shaped curve of the mullite rod, while the solid curves represent the electric field solutions at fixed cavity length.	120
8.6	A stable heating process achieved by increasing the output power of the generator.	121
8.7	An unstable heating process by increasing the output power of the generator.	122
8.8	The variation of the electric field in the rod with the temperature and L_2	123

8.9	Transmission line model for cavity.	123
8.10	Behavior of electric field and temperature for decreasing cavity length; high power level, short position around critical point a	124
8.11	Numerical results for heating of a mullite rod by decreasing the cavity length : Electric field versus temperature.	125
8.12	Numerical results for heating of a mullite rod by decreasing the cavity length : (a) Cavity length versus temperature. (b) Cavity length versus electric field.	126
8.13	Numerical results for heating of a mullite rod by increasing the cavity length : Electric field versus temperature.	127
8.14	Numerical results for heating of a mullite rod by increasing the cavity length : (a) Cavity length versus temperature. (b) Cavity length versus electric field.	128
8.15	Numerical results for heating of an alumina rod by decreasing the cav- ity length : Electric field versus temperature.	128
8.16	Numerical prediction of the temperature distribution in an alumina rod : (a) ρ direction (b) y direction.	129
8.17	Numerical prediction of the electric field distribution in an alumina rod along the y direction.	129
8.18	Numerical prediction of the temperature distribution in an alumina rod : (a) ρ direction (b) y direction.	130
8.19	Numerical prediction of the electric field distribution in an alumina rod along the y direction.	130
8.20	Numerical prediction of the temperature distribution in an alumina rod along the y direction.	131
9.1	Stability analysis using both S-shaped curve and cavity effects	133
9.2	Different heating process	134
9.3	Temperature history for heating of a mullite rod with 4.5 mm diameter from 790°C to 990°C	136

NOMENCLATURE

a	thermal diffusivity (m^2/s); waveguide width (m)
b	waveguide height (m)
CL	cavity length (m)
C_p	specific heat ($\text{J}/\text{kg} \cdot \text{K}$)
d	slab thickness (m)
D_p	penetration depth (m)
E	electric field (V/m)
f	microwave frequency (Hz)
h	convective heat transfer coefficient ($\text{W}/\text{m}^2 \cdot \text{K}$)
I	equivalent current (A)
J_n	Bessel function of 1st kind of order n
k_{mn}	wavenumber of the TE_{mn} mode (m^{-1})
L_1	the length between the iris plane and the rod location (m)
L_2	the length between the rod location and the short plane (m)
q_{abs}	power density (W/m^3)
r	radius of the rod(m)
\vec{S}	Poynting vector (W/m^2)
t	time (s)
T	Temperature ($^{\circ}\text{C}$ or K)
V	equivalent voltage (V)
Y_n	Bessel function of 2nd kind of order n
Z_0	characteristic impedance of the TE_{10} mode (Ω)
Z_a	the impedance of the iris(Ω)
z_a	the nomalized impedance of the iris
Z_b	the series part of the impedance of the rod(Ω)
z_b	the nomalized series part of the impedance of the rod
Z_c	the parallel part of the impedance of the rod(Ω)
z_c	the nomalized parallel part of the impedance of the rod

Greek symbols

α	attenuation constant (m^{-1})
β	phase constant (m^{-1})
ϵ_0	permittivity of free space (f/m)
ϵ	permittivity of materials (f/m) or emissivity
ϵ'	dielectric constant (f/m)
ϵ''	loss factor (f/m)
ϵ'_r	relative dielectric constant
ϵ''_r	relative loss factor
ϵ''_{eff}	effective relative loss factor
γ	propagation constant (m^{-1})
Γ	reflection coefficient
κ	thermal conductivity ($\text{W}/\text{m} \cdot \text{K}$)
λ_0	wavelength in free space (m)
λ_g	wavelength in waveguide (m)
μ_0	permeability of free space (h/m)
μ	permeability (h/m)
ω	angular frequency (s^{-1})
σ	electrical conductivity (S/m)
ρ_d	density (kg/m^3)

Chapter 1

Introduction

Originally, microwaves were principally used for communication. In 1950, the use of microwave energy to heat materials was discovered^[11]. Now microwave ovens have become common for heating food products in the home. The potential advantages of microwave heating have led researchers to design and implement new processes for industrial use. Although some non-thermal microwave effects have been observed and claimed by researchers, the main application of microwave processing of materials is in heating. The most prominent characteristic of microwave heating is *volumetric* heating, which is quite different from conventional heating where the heat must diffuse in from the surface of the material. Volumetric heating means that materials can absorb microwave energy directly and internally and convert it to heat. It is this characteristic that leads to advantages using microwaves to process materials.

In the past, microwave heating had been successfully used in the following fields: tempering meat, preheating rubber slugs, vulcanizing rubber, precooking bacon, drying pasta, drying crushed oranges, etc^[65]. Such industrial applications are centered around relatively low temperatures. Beginning in the late 1980s, there was growing interest in high temperature microwave processing of materials. With some successful applications at laboratory scale, for example, sintering of ceramics, microwaves are justified as a potential heating mechanism to replace some conventional heating methods. The potential applications have attracted more researchers to this field.

At present, the research objectives can be generally divided into three categories:

- How microwaves can be used to heat materials successfully and efficiently?
- What is the origin of microwave (non-thermal) effects?
- How the use of microwaves can be broadened to include novel microwave processing applications?

These three objectives are interwoven. Often, success in any one of them leads to progress in others. To get a comprehensive view of microwave processing, three review papers are recommended. The first paper was written by Sutton in 1989^[70]. Although it mainly focused on microwave processing of ceramics, some general problems, including the characteristics of microwaves, the features and benefits of microwave processing, and the problems and challenges encountered in microwave processing, were also reviewed.

The second paper was presented in 1997 by Clark *et al.*^[15] Besides giving examples, benefits, challenges and needs of microwave processing, two other problems were discussed in this paper. One is the question of specific microwave effects. Beginning with the experimental reports by Janney and Kimrey^[38] that the apparent activation energy for sintering of high-purity ceramics was lower for microwave firing than for conventional firing, microwave effects became a hot topic, and is still a controversial issue under current study. Another issue discussed in this review paper is the commercialization of microwave processing. Generally, as a heating source, microwaves could be used in almost all areas. However, in practice, the use of microwaves is limited by the high cost of electricity used in microwave power generation^[65]. To compete with the existing, established conventional heating methods, the properties resulting from the use of microwaves must be unique or enhanced relative to conventional processing or that significant cost, energy or space saving can be realized^[68]. At present, compared with the successful results obtained in the laboratory, few applications have been used in industrial processes. Gellings^[27] gave some illustrative discussions on this problem.

The third review paper, given by Bykov in 2001, discussed microwave processing of materials from the physical aspects^[9]. His discussion included more material on the fundamental concepts regarding the absorption of electromagnetic waves, heat transfer, and the electrodynamics of single and multimode microwave cavities. Some formulas, estimates, and illustrations, which are rarely seen in papers by material scientists, were given throughout the paper. Also, as a pioneer user of millimeter-wave processing, he listed the advantages of using millimeter-waves over microwaves.

In this dissertation, the thermal phenomena occurring with microwave heating are of interest. For conventional heating by convection and radiation, all heat must diffuse in from the surface of the material, and the inside of the material can be heated by conduction only. Since conduction is a diffusion process, heat cannot be intensified, or the maximum temperature is always on the surface. To avoid overheating the surface, normally the temperature of the heating source cannot exceed the desired final temperature T_f , thus the overall heating rate is restricted by the heating sources. Another factor limiting the heating rate is the diffusion process. Although the response of the surface temperature to the outside heating source could be very quick, the temperature response of the material other than on the surface is limited by the coefficient of thermal diffusivity a defined as

$$a = \frac{\kappa}{\rho_d C_p}, \quad (1.1)$$

where ρ_d , C_p , and κ are the density, specific heat, and thermal conductivity¹ of the material, respectively. Typical values of a are $117 \times 10^{-6} \text{ m}^2/\text{s}$ for copper, $11.9 \times 10^{-6} \text{ m}^2/\text{s}$ for alumina, and $0.18 \times 10^{-6} \text{ m}^2/\text{s}$ for woods at room temperature^[53]. For a material with characteristic length L , the diffusion time can be roughly approximated as L^2/a . If L is large or a is small, the heating rate will be slow. Simply increasing heat flux from the boundary cannot always solve this problem, and with increasing heat flux, the temperature distribution tends to be more nonuniform. This nonuniformity is not acceptable for many processes. However, when time approaches infinity, the materials can attain the final temperature T_f uniformly. This is one advantage of

¹The symbol k rather than κ is used to represent thermal conductivity in heat transfer. In this dissertation we use k to represent wavenumber.

conventional heating.

For microwave heating, due to the appearance of internal heating, the heating rate can be made large by adjusting the microwave source power, so rapid heating is one of advantages of microwave heating. Another characteristic of microwave heating is the inverse temperature distribution. Maximum temperature is always inside the material rather than on the surface if microwave power is the only heating source. In most cases, this is a disadvantage since uniform heating is desired during processing. However, such a temperature profile can play a positive role for some processes. For example, it has been used in chemical vapor infiltration to fabricate ceramic composite materials^[92].

Uniform heating is important, sometimes critical, when processing materials. In ceramics sintering, nonuniform temperature distributions can lead to undesired or failed results^[39]. Nonuniform heating in microwave processing results from several sources. First, nonuniformity stems from the uneven distribution of the electric field. This occurs in both single mode and multimode cavities. This type of nonuniformity can be alleviated by the use of a variable frequency microwave furnace^[6] or an untuned cavity (with the use of millimeter-wave energy)^[40]. Secondly, nonuniformity is a result of the interactions between electromagnetic waves and materials. A uniform field in an empty applicator might be nonuniform after the introduction of the materials. For example, attenuation can lead to nonuniform field distribution inside the material. With increasing loss factor, this effect is more serious and cannot be solved except by changing the heating source. As an extreme case, when microwaves are used to heat metal, the heating result is similar to radiation heating. Indeed, from the point of view of the physicist, both heating methods are interactions between electromagnetic waves and materials. The third origin of nonuniformity is due to the heat loss on the boundary. When processing bulk materials at high temperature, this type of nonuniformity becomes significant. Two methods have been used to solve this type of nonuniformity: surrounding the heated material with an insulator^[69] or by hybrid heating.

Two hybrid heating methods have been proposed. The first is called microwave

hybrid heating (MMH)^[23]. In this method, some susceptors, which are good absorbers of microwave energy at a specific temperature range, are used to provide extra heat flux to the heated sample by heat conduction and radiation. One example is heating alumina in a multimode cavity^[23]. Alumina is a poor absorber of microwaves at room temperature. With increasing temperature, alumina can absorb microwave energy more readily. By surrounding the alumina with SiC susceptors, which absorb microwave energy even at room temperature, the initial temperature increase of alumina is due to heat conduction and radiation from susceptors. As the temperature of the alumina increases up to 800°C, it can absorb microwaves directly. Another example is sintering powdered-metal^[62]. Unlike alumina, during the densification process powdered metal reflects more and more microwave power. The SiC susceptors play a more and more important role. Although the authors of that paper asserted that microwave field contributed most significantly to the successful sintering, it is believed by the present author that the susceptors are more important. The MMH method is a clever idea to heat some transparent and opaque materials. With the inclusion of an insulator, a fairly uniform temperature distribution can be generated. Two problems with the MMH method must be emphasized. First, due to the use of heat conduction, the characteristic of rapid heating is compromised. Secondly, during some stages of processing, microwave energy does not transmit directly into heated materials.

Another hybrid heating method is the use of a combination of conventional heating and microwave heating sources. This heating method might be a more practical solution to many problems. One example is the heating of a flowing fluid in a microwave resonant cavity^[78]. The calculated results showed that if the conventional heating method of a uniform surface heat flux was applied, the temperature distribution was nonuniform. To heat the fluid uniformly, a very long tube and a very small surface heat flux are required. By adding microwaves as an additional heating source, the fluid can be heated to a uniform temperature distribution; the tube length is not a determinant factor any more. Another example is the heating of materials in a furnace by the combination of a radiant (gas or electric elements) and microwave heating

sources^[8]. The experimental results showed that the materials can be processed much faster with less energy. An independent energy audit demonstrated a 39% reduction in the energy use, with the efficiency of the microwave-assisted furnace being 66% higher than the gas mode.

There is another type of thermal phenomenon occurring with microwave heating that is of interest. The properties of materials often change during the process. Of these properties, the change of dielectric loss factor is most important for some materials. The varying loss factor can lead to some unexpected results. For example, a sharp temperature wave was observed during microwave heating of porous zinc oxide in nitrogen and argon atmospheres^[21]; and a traveling hot spot was observed in microwave heating of oxide ceramic fibers^[79, 82]. The change of material properties can also induce thermal runaway, which is the topic of this dissertation. A survey of the literature of thermal runaway is given in the next chapter.

In Chapter 2, a general survey of the literature of thermal runaway is given, which includes experimental results, theoretical models, strategies to control thermal runaway, and prior work conducted at Virginia Tech.

In Chapter 3, the factors which affect microwave power absorption are discussed. The focus is on the variation of the dielectric properties of the material, which is the main interest of this dissertation.

In Chapter 4, the experimental setup, originated by Curtis^[19], is described. The focus will be placed on the parts that have been changed since Curtis' work. Also the electric field in an empty single mode cavity is discussed in detail.

In Chapter 5, the experimental results are provided. An S-curve, which is believed to be the reason of thermal runaway, is experimentally observed. This result also gives a possible method to control thermal runaway.

In Chapter 6, the equivalent circuit model of a microwave heating system is discussed. By the use of equivalent circuits, the electric field inside a waveguide can be simulated by a transmission line model. The discontinuities along the waveguide are represented by lumped parameters. This can alleviate the difficulty of analyzing the fields inside the cavity and also make the analysis of parameters affecting the

heating behavior feasible.

In Chapter 7, methods for determining the parameters in the equivalent circuits are discussed. The methods used to calculate the iris problem are mode matching and moment methods, which were developed by Terril^[75]. The results are compared with those obtained from the finite element method. The orthogonal expansion method is used to calculate the electric field in the heated rod. To deal with the varying dielectric properties, a line source model is developed.

In Chapter 8, the electric field obtained from the line source model is coupled with a heat transfer model developed by Goodson^[29]. The comparison of calculated results and experimental results are given.

This dissertation ends with Chapter 9, which includes the summary, conclusions and recommendations.

Chapter 2

Literature Review

Thermal runaway is a type of thermal instability resulting from the interaction between the electromagnetic waves and materials. The governing equation to describe this thermal phenomenon in solid materials is¹

$$\rho_d C_p \frac{\partial T}{\partial t} = \nabla \cdot (\kappa \nabla T) + q_{abs}, \quad (2.1)$$

where q_{abs} is the power density absorbed by a material, which is related to the electric field by the following equation [52]:

$$q_{abs} = \omega \varepsilon''_{eff} |E|^2, \quad (2.2)$$

where ω is the angular frequency, $|E|$ is the RMS magnitude of the electric field in the material, and ε''_{eff} is the imaginary part of the complex permittivity of the material (also called the effective loss factor²).

In Eq. (2.1), we have assumed that conventional heating sources or sinks are included in the boundary conditions. In some cases, if a problem is simplified to be in a two-dimensional, one-dimensional or lumped capacity form, the heating sources or sinks due to convection and radiation will explicitly appear in the equation.

¹This equation is not universally valid. If a fluid is heated by microwaves, the contribution due to convection must be added.

² $\varepsilon''_{eff} = \varepsilon'' + \sigma/\omega$, where ε'' is loss factor, and σ is the electrical conductivity of the materials. Both contribute to the heat loss. It is not possible to identify the contributions of ε'' and σ without a physical model. Since we always use effective loss factor in microwave heating, the variable ε'' will be used to represent effective loss factor. Also loss factor refers to effective loss factor throughout this dissertation.

In Chapter 1, we have discussed that heat conduction is a diffusion process, whose rate is limited by the coefficient of thermal diffusivity a . If for any reason the local diffusion rate is much less than the microwave power dissipation rate, the local temperature will increase rapidly. With increasing temperature, the properties of the material change. If such changes lead to the acceleration of microwave power dissipation at this local point, the temperature will increase more rapidly. The result of such a positive feedback is the formation of a hot spot^[42], which is a local thermal runaway.

All properties of the material have impacts on thermal runaway. Among these variables, ε'' is most important because its range of variation can be very large and q_{abs} is proportional to it. Other variables, such as ρ_d , C_p , κ , can also play roles because they affect the coefficient of thermal diffusivity a . The combinatorial effect of these properties can be viewed in the process of ceramic sintering. During the densification process, both ρ_d and ε'' increase. In a theoretical model given by Varadan *et al.*^[81], ε'' could increase by several orders. Also, with increasing temperature, C_p increases and κ decreases³^[53]. It appears that all variable changes make thermal runaway more likely, thus it is not surprising that thermal runaway is an important challenge in ceramic sintering^[71, 72].

In some cases, a global thermal instability can occur. This could be due to the evolving of local temperature rise by heat conduction or some other reasons. The governing equation based on an energy balance is

$$\rho_d C_p \frac{dT}{dt} = Q_{abs} - Q_{loss}, \quad (2.3)$$

where Q_{loss} is the heat loss, which normally includes losses due to convection and radiation, and Q_{abs} is the total dissipated microwave power in the material.

If thermal runaway occurs during the process, the temperature of the material could keep increasing until the material is damaged. This has happened in the process of microwave heating of ceramics^[80], minerals^[51], food^[63], rubber^[60], etc. Therefore thermal runaway, as a catastrophic phenomenon, hinders the use of microwaves to

³It is not clear the variation trends of C_p and κ during the densification process.

process materials.

In this chapter, a general survey of the literature of thermal runaway is given, which includes experimental results, theoretical models, strategies to control thermal runaway, and prior work conducted at Virginia Tech.

2.1 Experimental Observations of Thermal Runaway

Although experimental reports about thermal runaway are mentioned in many papers, a systematic experimental study is rarely seen. One experimental result was given by Roussy *et al.* in 1985^[60]. In this experiment, the microwave heating of EPDM rubber was studied. When the incident power was 25 W, a steady temperature could be attained; but when the power level was increased to 35 W, the temperature increased rapidly starting from some point and finally the rubber was burned. If viewed from a time-temperature graph, there is a point dividing the temperature response curve into two segments with clearly different heating rates. As the material is in the thermal runaway state, the temperature increases very rapidly.

Another experiment was provided by Zhang *et al.* in 2001^[93]. In their experiment, they observed the effect of power level on the heating of an 8% Pt/Al₂O₃ catalyst. Supported catalysts were heated by microwaves at constant power level. With the power level equal to or less than 90 W, the temperature of Pt/Al₂O₃ catalysts reached a constant value and increased gradually with increasing input power. When the input power level reached a critical value, which was between 90 W and 100 W, the temperature almost reached a constant value, and then suddenly rose again.

Two common points exist in these experimental reports. First, below a critical microwave power level, a stable temperature can be attained by the material at the end of the process and this temperature increases with increasing power. The second point is that the temperature of the material increases rapidly with a slight increase

of input microwave power from that critical power level. The experimental results show that the temperature response to the input power is not continuous; at some critical power value, a temperature discontinuity exists.

2.2 Theoretical Models to Explain Thermal Runaway

Much effort has been made to explain the thermal runaway phenomenon theoretically. It is not easy to find who is the first one trying to explain thermal runaway. Nonetheless, the work of Roussy *et al.*^[60] is certainly important.

Roussy *et al.*^[60] first brought forward the concept of critical temperature. A lumped capacity model was used to describe the energy balance. They assumed the thermal loss was by heat convection only; that is,

$$q_{loss} = h(T - T_0), \quad (2.4)$$

where T_0 is the ambient temperature and h is the convective heat transfer coefficient. Also, Roussy *et al.* assumed ε'' could be approximated by a quadratic function,

$$\varepsilon'' = a_0 + a_1(T - T_0) + a_2(T - T_0)^2. \quad (2.5)$$

Under these assumptions, Roussy *et al.* determined a critical temperature that represented an upper limit beyond which the heating was unstable. The critical temperature was determined only by the loss factor ε'' and the ambient temperature, $T_{critical} = T_0 + \sqrt{a_0/a_2}$.

In their later work^[59], Roussy *et al.* considered a cylindrical sample. In this case, the temperature variation along the radius was included in the model. They concluded that thermal stability was determined by one numerical criterion, which is a combination of thermal conductivity κ , convective heat transfer coefficient h , dielectric loss factor ε'' , ambient temperature T_0 , radius, and incident electric field.

From their assumptions, it is clear that their results may be valid only for electrically thin materials since a uniform electric field is assumed. Also, it is only valid for low temperatures since thermal radiation loss was not included in the model.

In 1992, Kriegsmann^[41] published an important attempt to explain thermal runaway. In this paper, he developed a one-dimensional model for the heating of a ceramic slab by microwaves. He found the important result that steady-state temperature as a function of the input microwave power gave an S-shaped response curve. A predicted S-shaped curve is illustrated in Fig. 2.1, where different electric fields represent different input power levels.

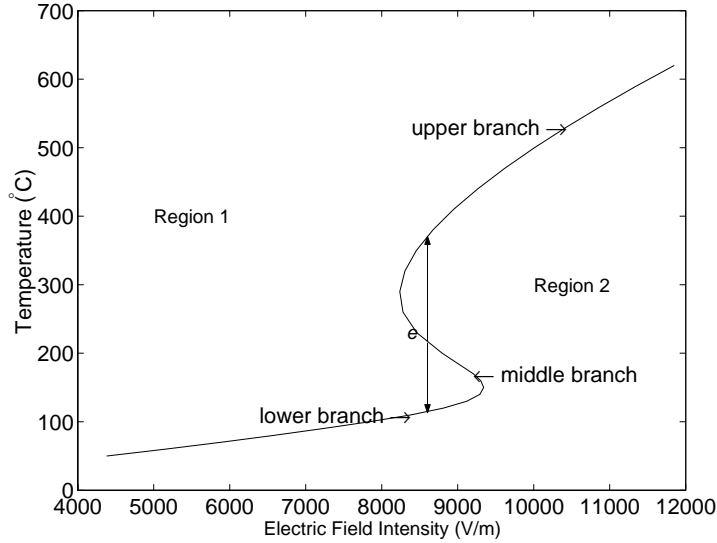


Figure 2.1: Stability analysis using S-shaped curve

Every point on the curve represents a thermally balanced state. The S-shaped curve divides the whole electric field and temperature plane into two regions. In Region 1, heat loss is larger than heat absorbed by the materials. In Region 2, heat loss is less than heat absorbed by the materials. Suppose there is a point e on the middle branch of the S-shaped curve. If the temperature fluctuates slightly, the temperature will keep increasing or decreasing until it reaches the equilibrium point on the upper or lower branch. Then from this S-shaped curve, the dynamic response for different power levels could be derived. Based on the energy balance, Kriegsmann concluded that the middle branch of the S-shaped curve was unstable. For that reason, a temperature jump is possible, suggesting a plausible mechanism for thermal runaway control problems.

After Kriegsmann's initial work, other researchers found the S-shaped curve

under different conditions. Jackson *et al.*^[37] developed a one-dimensional model for microwave heating of a sphere in a rectangular resonant cavity. The temperature variation along the radius as well as the temperature dependencies of thermal properties was taken into account. Their results were similar to Kriegsmann's^[41]. An interesting result was that the temperature difference between the sphere center and surface could be very large. As they reported, for an 0.875 cm radius alumina sphere heated at an electric field of 200 kV/m, a 100 °C temperature difference was generated after 83.5 seconds. For long processing times, the surface temperature was nearly unchanged while the center temperature experienced thermal runaway. Since only surface temperature could be measured during experiments, this result might be important for processing materials.

Spotz *et al.*^[67] examined the thermal stability of cylindrical alumina rods heated by microwaves. Their thermal model was a one-dimensional heat transfer equation, while the electric field was assumed to be constant. Based on an exponential form of ε'' , a half S-shaped curve, which included the lower and middle branches of the complete S-shaped curve, was obtained. Given that, their results were more similar to Roussy's^[59], which meant above some critical temperature, thermal stability was impossible, at least for some forms of alumina.

Gupta *et al.*^[30] analyzed the one-dimensional slab heated by microwaves. Following the lead of previous authors, the S-shaped curve was used to analyze the thermal stability. One interesting result was that thermal runaway could be avoided by selecting a particular thickness of slab.

Although the above models are different from each other, the common point is that dielectric loss factor ε'' plays the most important role in thermal runaway.

Vriezinger presented a series of papers to explain the thermal runaway phenomenon from a different perspective. His motivation stemmed from the thermal runaway phenomenon of materials other than ceramics. For demineralized water, ε'' hardly depends on temperature. Although ε'' even decreases slightly with increasing temperature, thermal runaway still occurs. In his paper published in 1996^[83], a one-dimensional isothermal slab irradiated by microwaves was used to analyze ther-

mal runaway. This model is same as Kriegsmann's, however, the heated material is different. Vriezinger found the total power dissipated in the material as a function of length of slab, attenuation constant α , wavenumber β , transmission coefficient, and reflection coefficient. He argued that α and β were more appropriate than ϵ'' to explain thermal runaway. Since β appeared in the argument of a cosine function, a slight variation of β with temperature strongly affected power dissipation. Then the power dissipation in the materials oscillates as a function of temperature. Similarly, he obtained an S-shaped curve again. One conclusion in this paper was the existence of a critical length. If the length of the slab is small enough, thermal runaway does not occur.

In 1998, Vriezinger^[84] studied isothermal cylinders and spheres heated by microwaves. The results were similar to his previous work. He obtained the more general conclusion that any isothermal object with characteristic dimension L would never be overheated by microwaves due to thermal runaway if L was smaller than $\pi/4\Delta\beta$, where $\Delta\beta$ is the difference between the maximum and the minimum value of β . More importantly, Vriezinger realized thermal runaway originates from resonance. Vriezinger also investigated the influence of the Biot number on thermal runaway^[85]. Since he always used water as sample, he concluded that the Biot number did not affect the results.

Vriezinger further extended his research to include ceramic materials^[86]. He explicitly expressed the view that the phenomenon of thermal runaway cannot be explained by looking at ϵ'' . He believed thermal runaway could be understood only through the wavenumber β and the attenuation constant α . He concluded the resonance due to small decrease of β with increasing temperature was the origin of thermal runaway for water, while the increase of α with increasing temperature caused thermal runaway for ceramic materials.

By the use of resonance to explain thermal runaway, Vriezinger provided a good supplementary explanation. However, his conclusion that thermal runaway cannot be explained by looking at ϵ'' is too sweeping.

Parris *et al.*^[56] gave an alternative model to explain thermal runaway. They

showed thermal runaway might occur if the thermal conductivity of the material decreases with increasing temperature.

All the theoretical models mentioned so far give reasonable results. The best way to understand the origin of thermal runaway might be from the heat diffusion equation and an energy balance. Any property change that can decrease the diffusion rate or increase the heat absorption rate could be a contribution factor to thermal runaway.

2.3 Control of Thermal Runaway

If the operating temperature required by the processing exceeds the maximum stable temperature, a control system must be included. Based on the controlled parameters, control methods can be divided into two groups.

The first is to control input power directly. This idea naturally appeared in early experiments. During the experiment, temperatures of the material were monitored. When the desired temperature was reached, the power source was adjusted manually^[80]. These attempts sometimes led to success. However, when materials are in a thermal runaway state, the temperature rise rate is rapid and temperature is highly sensitive to the incident power. For that reason, the difficulty in this method is apparent. Then an automatic control system must be introduced.

Beale *et al.*^[3, 4] developed an automatic feedback control system. They regulated the temperature of the ceramic sample about a reference value with little overshoot or oscillation by adjusting the power level. They could regulate material temperature above the critical value. At the same time, they reported that the control of thermal runaway material was not as accurate as it was with non-thermal runaway materials.

Another idea about controlling microwave heating is derived from an energy balance. This idea was explicitly expressed by Thomas *et al.*^[77, 76] They monitored and controlled the power absorbed by the sample. From the energy balance, if the material is in steady state, heat loss must be equal to power absorbed. Since heat loss

is a monotonically increasing function of temperature, constant power absorbed by materials means a specific temperature. Then, if power absorbed by materials can be controlled to be constant, thermal runaway can be avoided. Numerical simulations also verified this idea. However, to maintain constant power absorbed by materials, an automatic control system must be introduced.

2.4 Prior Work at Virginia Tech

In 1997, Goodson^[29] developed a two-dimensional numerical model, which can compute the temperature distribution along radial and axial directions for a rod under microwave heating. The model can also handle moving rods. Temperature dependent properties, including convection heat transfer coefficient, emissivity, conductivity and dielectric loss factor were incorporated into the model, but the electric field in the material was assumed to be constant.

In 1998, Terril^[75] used the mode-matching method to develop a numerical model to calculate the electric field distribution along the length of the rod in a resonant cavity. The model also included the effect of the iris on the field.

In 1999, based on the previous work by Goodson and Terril, McConnell^[50] developed a coupled thermal and electromagnetic field model.

In 1999, Curtis^[19] performed experimental research on microwave heating of thermal runaway ceramics and polymers. The materials were heated with three different programs, including constant absorbed power in the sample, constant power to the applicator, and constant electric field strength. Microwave power losses in a resonant cavity were characterized by measuring the difference between forward and reflected power to and from the cavity while tuning the empty cavity with forward power held constant. With the cavity losses known as a function of field strength in the cavity, it was then possible to measure and control the power absorbed by materials undergoing microwave heating. The results demonstrated that careful control of absorbed power was an effective means of avoiding thermal runaway in microwave processing of materials.

In 2000, Huie^[34] measured S parameters of the microwave heating network using an HP-8510 Automated Network Analyzer. His measurements included the waveguide short, the couplers, the wedge and iris, and the four-stub tuner. The data were collected and then embodied in Hewlett Packard Advanced Design Software to simulate the heating system. His measurement also include the geometry of the iris and cavity, the relation between the dial setting on the short and the cavity length.

2.5 Research Objective

Thermal runaway has been studied by many researchers over the past twenty years, and several different approaches have been used. Although the origin of thermal runaway can be due to different reasons, a common thread is that it is the energy balance that determines thermal stability. The theory of the S-shaped curve, based on an energy balance, is the most plausible explanation for thermal runaway. The beauty of the S-shaped curve is its visual simplicity even though the derivation could include complex mathematics. However, there has been no exhaustive study that considers whether the S-shaped curve really exists or if it is only an artifact of the assumptions inherent in the mathematical model. No researcher has declared that an S-shaped curve had been observed experimentally. The difficulty of such observation is obvious because the middle branch of an S-shaped curve is intrinsically unstable.

The objective of the research presented in this dissertation is to experimentally obtain the S-shaped curve to verify the theory. Since the middle branch of the S-shaped curve is unstable, I attempt to find a suitable control strategy to avoid thermal runaway. At the same time, I intend to improve the current numerical model to make better prediction of the microwave heating process.

Chapter 3

Microwave Power Absorption

In this chapter, some basic concepts of microwave power absorption by materials are discussed, then calculated examples are used to show how dielectric properties and the size of the material affect the power absorption.

The relation between the power density absorbed by a material and the electric field has been given in Eq. (2.2):

$$p_{dis} = \omega \varepsilon''_{eff} |E|^2 = q_{abs}. \quad (3.1)$$

From an electromagnetic (EM) point of view, p_{dis} is the power density dissipated in the materials. In the heat transfer equation, q_{abs} represents the heat generation term. It is this equation that connects the electromagnetic waves with heat transfer phenomenon. The variable ε'' plays an important role in microwave heating. For Maxwell's equations, ε'' , combined with ε' (which is the real part of the complex permittivity of the material), represents the material. In the heat transfer equation, this variable determines the heat generation rate, as expressed in Eq. (3.1).

It appears that ε' is not as important as ε'' viewed from Eq. (3.1) since it doesn't explicitly appear in the equation. However, as one important property of the material, ε' can affect the absorbed power through its impact on the electric field inside the material. In the following sections, we will use two simple examples to discuss the power issues in microwave heating.

3.1 A uniform plane wave traveling in half infinite space

As the first example, we discuss a uniform plane wave¹ propagating in an unbounded lossy medium. Suppose the wave is traveling in the $+z$ direction and the electric field has only x component. In addition, the amplitude of E_x is independent of x and y . From Maxwell's equations^[2], these conditions guarantee that the magnetic field has only y component. The fields can be expressed as

$$\vec{E} = E_0 e^{-\gamma z} \hat{x}, \quad (3.2)$$

$$\vec{H} = \frac{E_0}{\sqrt{\mu/\varepsilon}} e^{-\gamma z} \hat{y}, \quad (3.3)$$

where $\varepsilon = \varepsilon' - j\varepsilon''$ and μ is the permeability of the material. Throughout this dissertation, $\mu = \mu_0$, the free space permeability. In the above equations, γ , the propagation constant, is the most important parameter to describe a EM wave. The definition of γ is^[2]

$$\begin{aligned} \gamma &= \sqrt{j\omega\mu j\omega\varepsilon} = \omega\sqrt{\varepsilon_0\mu_0}\sqrt{-\varepsilon'_r + j\varepsilon''_r} \\ &= \frac{\pi(2\varepsilon'_r)^{1/2}}{\lambda_0} \left(\sqrt{\left(1 + \left(\frac{\varepsilon''_r}{\varepsilon'_r}\right)^2\right)^{1/2} - 1} + j\sqrt{\left(1 + \left(\frac{\varepsilon''_r}{\varepsilon'_r}\right)^2\right)^{1/2} + 1} \right). \end{aligned} \quad (3.4)$$

where ε'_r and ε''_r are relative dielectric constant and relative loss factor, which are defined as

$$\varepsilon'_r = \varepsilon'/\varepsilon_0, \quad (3.5)$$

$$\varepsilon''_r = \varepsilon''/\varepsilon_0, \quad (3.6)$$

where ε_0 is the permittivity of the free space and λ_0 is the wavelength in free space defined as

$$\lambda_0 = \frac{2\pi}{\omega\sqrt{\mu_0\varepsilon_0}}. \quad (3.7)$$

¹A uniform plane wave is the simplest electromagnetic wave. \mathbf{E} and \mathbf{H} , which are orthogonal to each other, construct the transverse plane. The propagation direction is orthogonal to the transverse plane. In the transverse plane, the phase and the amplitude of \mathbf{E} and \mathbf{H} are constants, so the wave is called a *uniform* wave. Along the propagation direction, different transverse planes are parallel, so the wave is called a *plane* wave.

If the frequency of the microwave source is 2450 MHz, λ_0 is equal to 12.24 cm.

Normally, γ is written in the form

$$\gamma = \alpha + j\beta, \quad (3.8)$$

where α is the attenuation constant and β is phase constant. Comparing this equation with Eq. (3.4), we obtain

$$\alpha = \frac{\pi(2\varepsilon_r')^{1/2}}{\lambda_0} \sqrt{\left(1 + \left(\frac{\varepsilon_r''}{\varepsilon_r'}\right)^2\right)^{1/2} - 1}, \quad (3.9)$$

and

$$\beta = \frac{\pi(2\varepsilon_r')^{1/2}}{\lambda_0} \sqrt{\left(1 + \left(\frac{\varepsilon_r''}{\varepsilon_r'}\right)^2\right)^{1/2} + 1}. \quad (3.10)$$

Now the fields are written as

$$\vec{E} = E_0 e^{-\alpha z} e^{-j\beta z} \hat{x}, \quad (3.11)$$

$$\vec{H} = \frac{E_0}{\sqrt{\mu/\varepsilon}} e^{-\alpha z} e^{-j\beta z} \hat{y}. \quad (3.12)$$

The Poynting vector \vec{S} , which defines the power flux associated with a propagating EM wave, is given by^[31]

$$\vec{S} = \vec{E} \times \vec{H}^* = \frac{(\sqrt{\varepsilon})^*}{\sqrt{\mu}} |E_0|^2 e^{-2\alpha z}. \quad (3.13)$$

From an energy balance, the power density dissipated in the material is

$$p_{dis} = -\text{Re}(\nabla \cdot \vec{S}) = \frac{2\alpha \text{Re}((\sqrt{\varepsilon})^*)}{\sqrt{\mu}} |E_0|^2 e^{-2\alpha z} = \frac{2\alpha \text{Re}((\sqrt{\varepsilon})^*)}{\sqrt{\mu}} |\vec{E}|^2. \quad (3.14)$$

It can be shown by some algebraic calculations that

$$\frac{2\alpha \text{Re}((\sqrt{\varepsilon})^*)}{\sqrt{\mu}} = \omega \varepsilon'', \quad (3.15)$$

thus, the power density dissipated in the lossy materials can be expressed as

$$p_{dis} = \omega \varepsilon'' |E_0|^2 e^{-2\alpha z}. \quad (3.16)$$

The variable E_0 is the amplitude of the electric wave at $z = 0$, from where the wave originates. E_0 is related to the microwave power source through the reflection

coefficient Γ and transmission coefficient T . In microwave heating, at least two media exist in the system. Microwaves travel from medium 1 into medium 2 and heat medium 2. Since the materials have different properties, only part of the energy from the power source can be transmitted into the heated material, while the remainder will be reflected. The reflection and transmission are described by Γ and T . Normally, Γ and T of a specified mode² are functions of the media. For a uniform plane wave traveling in half infinite space, the formulas to calculate Γ and T can be found in any EM waves book.

From Eq. (3.14), part of the energy carried by waves changes into heat as EM waves travel in the lossy material. As a result, the amplitude of the wave and the carrying power attenuate exponentially. A useful parameter describing the attenuation effect is the penetration depth, which is defined as^[15]

$$D_p = \frac{1}{2\alpha}. \quad (3.17)$$

The physical meaning of penetration depth is the distance that the EM wave must travel in a lossy medium to reduce its power to $e^{-1} = 0.368$ of the original value, as seen from Eq. (3.13). This value is one half of the skin depth used in electromagnetics^[2].

The above discussion can be applied only in an infinite half space. In reality, all materials have finite dimensions. Multiple reflections will occur on the interfaces; thus, the form of the waves existing in materials is the superposition of traveling waves and standing waves. It is the interferences among the waves that make the problem more interesting. We will use a simple example to illustrate such phenomena.

3.2 A TE₁₀ wave traveling in waveguide to heat a finite size material

Fig. 3.1 describes a microwave heating system. A slab is placed inside a waveguide and divides the waveguide into three regions. We use subscripts 1 and 3 to represent

²A mode is a particular field configuration, which is an eigenfunction of Maxwell's equation and satisfies the prescribed boundary condition^[2].

the air regions and 2 to represent the slab region. The microwaves illuminate the slab from two directions with amplitude A_1 and B_3 . The transverse dimensions of the waveguide is $a \times b$, which are selected so that only the TE_{10} mode is allowed to propagate at the microwave operating frequency. The thickness of the slab is d and the transverse area of the slab is the same as that of the waveguide. The complex permittivity of the slab is $\epsilon_0 (\epsilon'_r - j\epsilon''_r)$, which is assumed to be a constant. Similar problems have been discussed by Ayappa *et al.*^[1] and Pelesko *et al.*^[57] In their discussions, a slab with finite thickness is placed in free space rather than inside the waveguide.

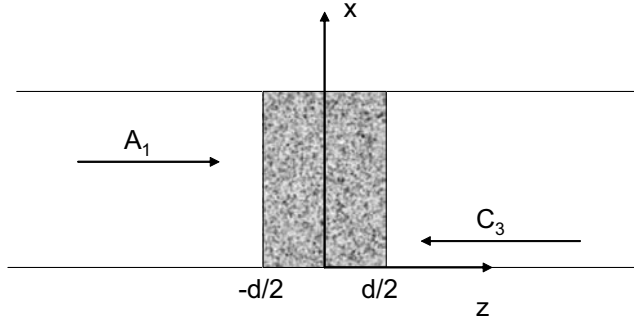


Figure 3.1: A slab heated by the TE_{10} mode in a waveguide.

The first step to determine the fields is to calculate the propagation constants in different media. Even though the media in region 1 and region 3 are air, the propagation constant is different from that in free space because the waveguide confines the wave. The propagation constants are expressed as

$$\gamma_i = \sqrt{\epsilon_{r,i}\gamma_0^2 + \left(\frac{\pi}{a}\right)^2} \quad i = 1,2,3, \quad (3.18)$$

where

$$\gamma_0 = \sqrt{-\omega^2\epsilon_0\mu}, \quad (3.19)$$

$$\epsilon_{r,1} = \epsilon_{r,3} = 1, \quad (3.20)$$

$$\epsilon_{r,2} = \epsilon_r = \epsilon'_r - j\epsilon''_r. \quad (3.21)$$

Although we have assumed that only the TE_{10} mode exists in the waveguide, higher order modes may appear in the slab if the value of ϵ_r is large enough. However, higher

order modes will be inhibited by the boundary conditions on the interfaces, thus the fields in any region can be expressed as

$$\begin{aligned} E_{y,i} &= \sin\left(\frac{\pi x}{a}\right)(A_i e^{-\gamma_i z} + B_i e^{\gamma_i z}), \\ H_{x,i} &= -\frac{\gamma_i}{j\omega\mu} \sin\left(\frac{\pi x}{a}\right)(A_i e^{-\gamma_i z} - B_i e^{\gamma_i z}) \quad i = 1,2,3. \end{aligned} \quad (3.22)$$

By the use of the boundary conditions that E_y and H_x are continuous at $z = \pm d/2$, the coefficients can be determined as

$$\begin{aligned} B_1 &= \frac{e^{d\gamma_1} [A_1 (-1 + e^{2d\gamma_2}) (\gamma_{1,2}^2 - 1) + 4B_3 e^{d\gamma_2} \gamma_{1,2}]}{e^{2d\gamma_2} (\gamma_{1,2} + 1)^2 - (\gamma_{1,2} - 1)^2}, \\ A_2 &= \frac{2e^{\frac{1}{2}d(\gamma_1 + \gamma_2)} \gamma_{1,2} [A_1 e^{d\gamma_2} (1 + \gamma_{1,2}) + B_3 (1 - \gamma_{1,2})]}{e^{2d\gamma_2} (\gamma_{1,2} + 1)^2 - (\gamma_{1,2} - 1)^2}, \\ B_2 &= \frac{2e^{\frac{1}{2}d(\gamma_1 + \gamma_2)} \gamma_{1,2} [A_1 (1 - \gamma_{1,2}) + B_3 e^{d\gamma_2} (1 + \gamma_{1,2})]}{e^{2d\gamma_2} (\gamma_{1,2} + 1)^2 - (\gamma_{1,2} - 1)^2}, \\ A_3 &= \frac{e^{d\gamma_1} [4A_1 e^{d\gamma_2} \gamma_{1,2} + B_3 (-1 + e^{2d\gamma_2}) (\gamma_{1,2}^2 - 1)]}{e^{2d\gamma_2} (\gamma_{1,2} + 1)^2 - (\gamma_{1,2} - 1)^2}. \end{aligned} \quad (3.23)$$

where

$$\gamma_{1,2} = \frac{\gamma_1}{\gamma_2}. \quad (3.24)$$

The dissipated power density in the slab can be computed from Eq. (3.1). The total power dissipated in the slab can be obtained by either integrating the power density over the slab region or by computing from the difference of the Poynting vector at $z = \pm d/2$. For the TE₁₀ mode,

$$\vec{S} = \vec{E} \times \vec{H}^* = E_y \hat{y} \times (H_x \hat{x} + H_z \hat{z})^* = -E_y H_x^* \hat{z} + E_y H_z^* \hat{x}. \quad (3.25)$$

It can be shown the power carried by the waves in the x direction is purely reactive, so the power is dissipated along only the z direction. Hence, the total dissipated power P_{total} is given by

$$P_{total} = Re [(E_y H_x^*)|_{z=d/2} - (E_y H_x^*)|_{z=-d/2}]. \quad (3.26)$$

Apparently, P_{total} is a function of ε_r , d , A_1 and B_3 . To understand microwave heating, it is necessary to discuss how these parameters affect the power dissipation. For

simplicity, we drop the factor $\sin(\pi x/a)$, hence the only independent variable is z . Also we set $A_1 = 1$, $B_3 = 0$ and $d = 1 \text{ cm}$ when discussing the effects of ε' , ε'' .

Dielectric constant ε'_r

When ε' increases and ε'' is fixed, the phase constant β increases and the attenuation constant α decreases, as illustrated by Fig. 3.2. It can be seen from Fig. 3.3 that the total power dissipated in the slab (normalized by the incident power) tends to decrease with the increase of ε' . This can be understood by considering that the *mismatch* between the air and slab becomes more serious so that more power is reflected by the slab. However, there is a clear peak if ε'' is not too large. At this point, the slab is in its first resonant state, as illustrated by Fig. 3.4. This is obvious if we notice that $\beta d \approx \pi$. If ε' is increased to a larger number, say 1000, more resonant states can be observed. From Fig. 3.3, it appears that the resonant state depends on only ε' , but this is true only if the value of ε'' is small. If ε'' is large enough, the resonant point will shift and $\beta d \approx \pi$ is not a useful criterion to judge whether the slab is in a resonant state. Actually, in that case, the peak will be smeared out since the attenuation effect is so prominent. An example is given by the curve with parameter $\varepsilon'' = 100$ in Fig. 3.3.

Loss factor ε''_r

When ε''_r increases and ε' is fixed, both the phase constant β and the attenuation constant α increase. Their behaviors are illustrated by Fig. 3.5. The total power dissipated in the slab (normalized by the incident power) is given in Fig. 3.6. With increasing ε'' , the total dissipated power increases first and then decreases. This behavior can be explained by Eq. (3.1). When ε'' is small, the attenuation effect is negligible, then dissipated power increases with increasing ε'' . As ε'' increases to some critical value, the attenuation effect becomes dominant. The term $|E|^2$ in Eq. (3.1) decreases much faster, which induces the total dissipated power to decrease.

Slab thickness d

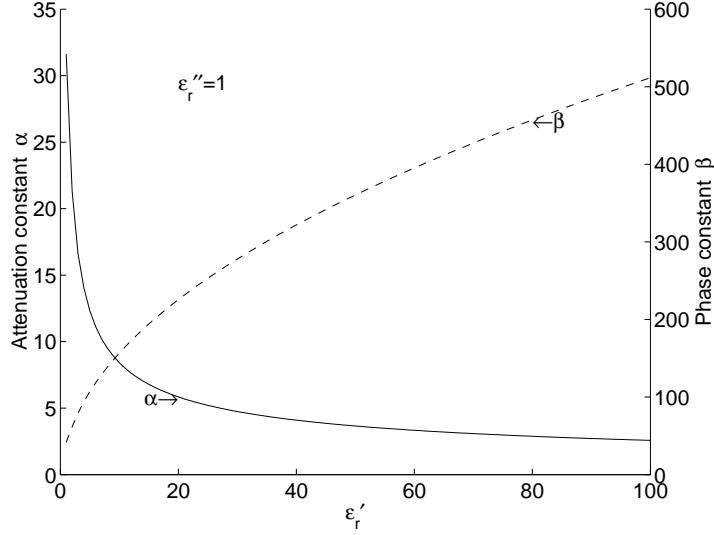


Figure 3.2: Variation of phase constant and attenuation constant with dielectric constant.

We select two materials to discuss the variation of dissipated power with slab thickness. One is alumina (Al_2O_3) of 99% purity^[26] with $\epsilon_r = 9.5 - 0.0009j$; the other is cooked beef^[1] with $\epsilon_r = 30.5 - 9.60j$. Since it is the power density that will determine the final temperature of the materials, we calculated averaged power density rather than the total dissipated power. The averaged power density, \bar{p} , is defined as

$$\bar{p} = P_{total}/d. \quad (3.27)$$

The calculated results are shown in Fig. 3.7. In the plot range, the attenuation effect for Al_2O_3 is negligible because its $D_p = 64m$. With increasing thickness, \bar{p} behaves like a periodic function, whose peaks correspond to the resonant states. In contrast, \bar{p} of the beef is heavily affected by the attenuation effect. With increasing thickness, \bar{p} decreases rapidly. There are only two identifiable peaks.

We have discussed how ϵ_r and the thickness affect the dissipated power; two important points from this discussion are:

1. At the resonant states, the materials can absorb more power. If ϵ_r'' is not too large, the phase constant state can be determined by the relation $\beta d = n\pi, n =$

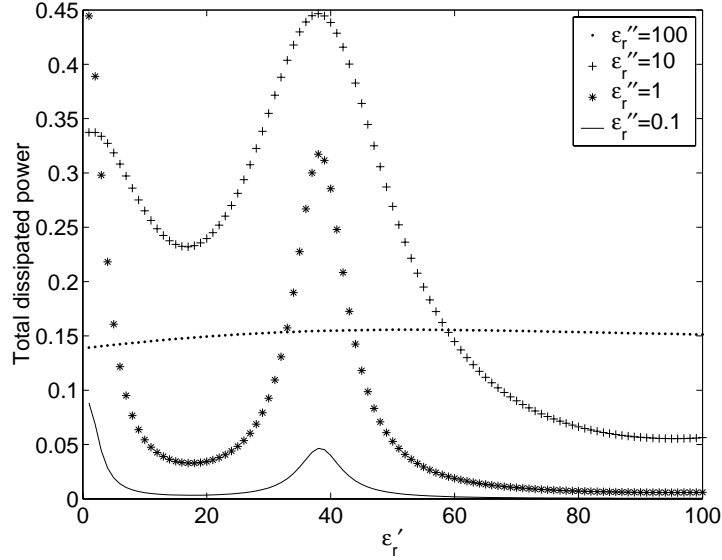


Figure 3.3: Variation of absorbed power with dielectric constant, where $A_1 = 1$, $B_3 = 0$, and $d = 1$ cm.

1, 2, 3.... In practical heating, the shape of the material could be very complex. The resonant state will be determined by solving the eigenvalue problem. Since the system with finite dimension has discrete eigenvalues, the heated material can absorb microwave much more easily at some dimensions (dielectric constants) if the dielectric constant (dimension) of the material is fixed.

2. With increasing ε_r'' , the power density dissipated in the material first increases and then decreases.

Next, we will discuss how A_1 and B_3 affect the power dissipation.

Incident field coefficients A_1 and B_3

By choosing different combinations of A_1 and B_3 , we can simulate various field patterns. For example, by setting $A_1 = 1$ and $B_3 = 0$, the material is illuminated by microwaves from one side; by setting $A_1 = 1$ and $B_3 = 1$, the material is put at the maximum electric field point; by setting $A_1 = 1$ and $B_3 = -1$, the material is put at the maximum magnetic field point. Generally, we can let $A_1 = 1$ and $B_3 = e^{j\theta}$, where $\theta \in (0, \pi)$.

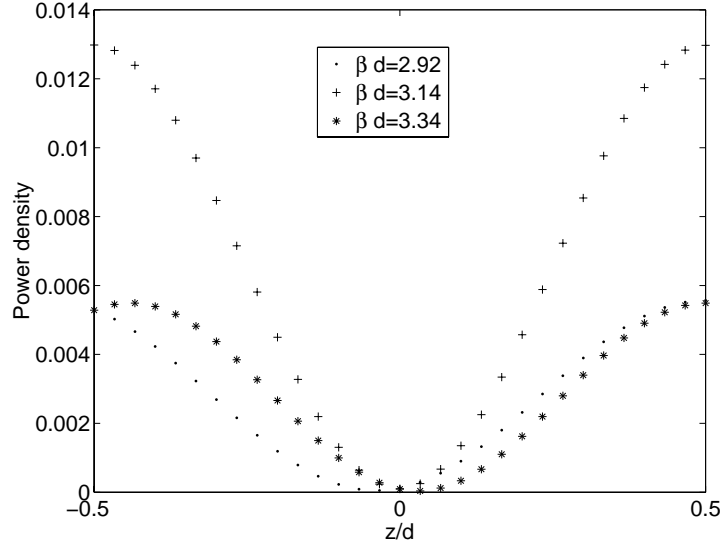


Figure 3.4: Effect of phase constant on power density distribution in the slab, where $A_1 = 1$, $B_3 = 0$, and $d = 1$ cm.

This study is inspired by the work of Cheng *et al.*^[12] They reported that for some materials, the microwave heating should be attributed to the magnetic field rather than the electric field. Before their work, a similar idea had been proposed by some researchers in France. Cherradi *et al.*^[13] used a resonant cavity to heat different materials including insulators, semiconductors and metals. They observed that semiconductor materials were heated more efficiently if the material is put at a maximum of the magnetic field. Also, they asserted that Eq. (3.1) cannot be used to explain such phenomena. They attributed the heating to so-called eddy currents, the consequence of dissipated power by the Joule effect, and they concluded that for some materials the maximum heating corresponded to the maximum magnetic field.

Here we encounter a dilemma. Eq. (3.1) is directly derived from Maxwell's equation and ε''_{eff} has been used to include all heat sources except magnetic loss (ferromagnetic materials with large μ). Therefore, both dielectric heating and Joule effect should have been included in Eq. (3.1). The power density must be proportional to the square of the RMS magnitude of the electric field, or the maximum heating must correspond to the maximum electric field.

To explain this contradiction, we consider two special cases: E case and H

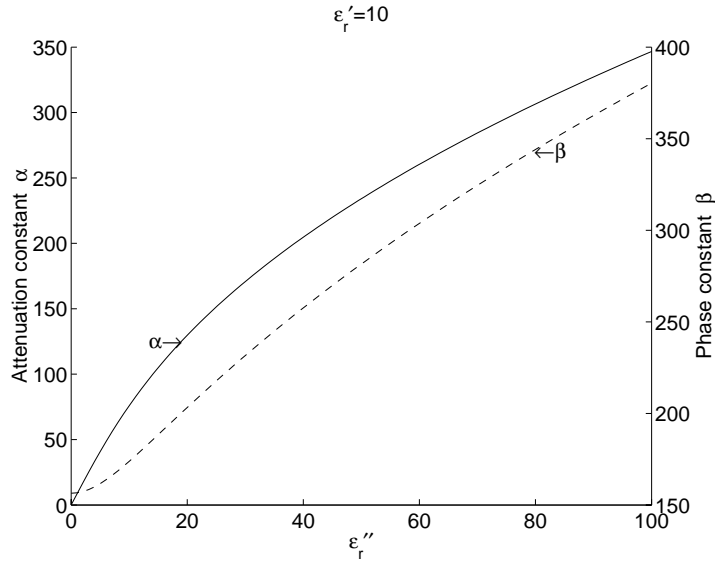


Figure 3.5: Variation of phase constant and attenuation constant with loss factor.

case. In the E case, we let $A_1 = 1$ and $B_3 = 1$ so that the electric field is maximum and magnetic field is zero at $z = 0$; in the H case, we let $A_1 = 1$ and $B_3 = -1$ so that the electric field is zero and magnetic field is maximum at $z = 0$. After obtaining A_2 and B_2 from Eq. (3.23), the electric and magnetic fields from Eq. (3.22) can be expressed as

E case

$$\begin{aligned} E_{y,2} &= f_1(e^{-\gamma_2 z} + e^{\gamma_2 z}), \\ H_{x,2} &= -j \frac{\gamma_2}{j\omega\mu} f_1(e^{-\gamma_2 z} - e^{\gamma_2 z}), \end{aligned} \quad (3.28)$$

H case

$$\begin{aligned} E_{y,2} &= f_2(e^{-\gamma_2 z} - e^{\gamma_2 z}), \\ H_{x,2} &= j \frac{\gamma_2}{j\omega\mu} f_2(e^{-\gamma_2 z} + e^{\gamma_2 z}). \end{aligned} \quad (3.29)$$

The power density and total power dissipated in the slab are expressed as

E case

$$p_{dis} = |f_1|^2 \frac{2\alpha\beta}{\omega\mu} [(e^{2\alpha z} + e^{-2\alpha z}) + 2 \cos(2\beta z)], \quad (3.30)$$

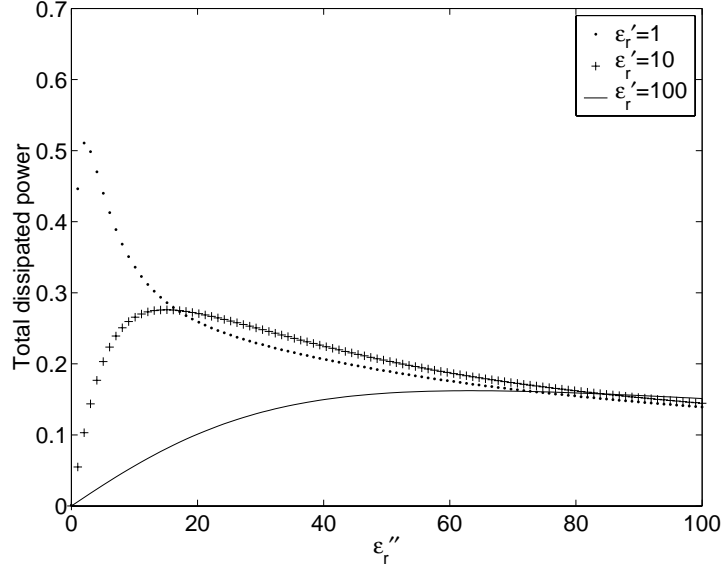


Figure 3.6: Variation of absorbed power with loss factor, where $A_1 = 1$, $B_3 = 0$, and $d = 1$ cm.

$$P = \frac{|f_1|^2}{\omega\mu} [2\beta (e^{\alpha d} - e^{-\alpha d}) + 4\alpha \sin(\beta d)], \quad (3.31)$$

H case

$$p_{dis} = |f_2|^2 \frac{2\alpha\beta}{\omega\mu} [(e^{2\alpha z} + e^{-2\alpha z}) - 2\cos(2\beta z)], \quad (3.32)$$

$$P = \frac{|f_2|^2}{\omega\mu} [2\beta (e^{\alpha d} - e^{-\alpha d}) - 4\alpha \sin(\beta d)], \quad (3.33)$$

where

$$\alpha = \text{Re}(\gamma_2), \quad (3.34)$$

$$\beta = \text{Im}(\gamma_2), \quad (3.35)$$

$$f_1 = \frac{2e^{\frac{1}{2}(\gamma_1 + \gamma_2)d}\gamma_1}{e^{\gamma_2 d}(\gamma_1 + \gamma_2) - (\gamma_2 - \gamma_1)}, \quad (3.36)$$

$$f_2 = \frac{2e^{\frac{1}{2}(\gamma_1 + \gamma_2)d}\gamma_1}{e^{\gamma_2 d}(\gamma_1 + \gamma_2) + (\gamma_2 - \gamma_1)}. \quad (3.37)$$

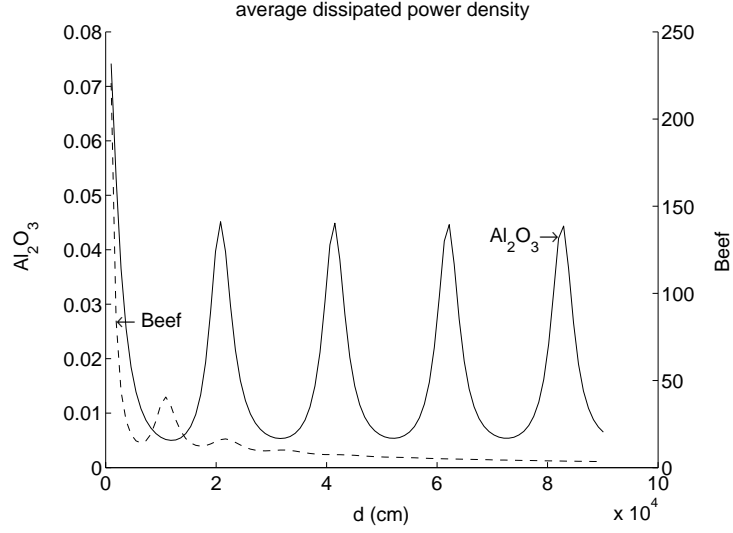


Figure 3.7: Variation of average dissipated power density with slab thickness. The relative complex permittivities of beef and Al_2O_3 are $30.5-9.60j$ and $9.5-0.0009j$, respectively.

From the above equations, it is clear that the electric field and power density at $z = 0$ in the H case is zero. However, the total power dissipated in the materials, P , is the integral of p_{dis} over the whole slab, so we need to consider the behavior of p_{dis} in the range of $(-d/2, d/2)$. The \cos term in the expression of p_{dis} is a periodic function. If the thickness of the slab d is selected so that βd is greater than π and less than 2π , the behavior of p_{dis} in these two cases is as illustrated in Fig. 3.8. Viewed as a wave, this means that the wave inside the material has experienced a full power period. Although p_{dis} is zero at $z = 0$ in the H case, p_{dis} does reach its maximum inside the slab. Compared with only one maximum point of p_{dis} inside the slab in the E case, two maximum points exist in the H case, so P in the H case could be greater than that in the E case. This can be also observed from the expressions for P . At the condition that $\pi < \beta d < 2\pi$, the \sin term in H case is greater than zero while it is less than zero in the E case.

The impact factors f_1 and f_2 also affect the power dissipation. For different materials, they exhibit different variations with the thickness of the slab. We use three typical materials to explain this problem more clearly.

The first two materials are the Al_2O_3 and beef we have used before. The third

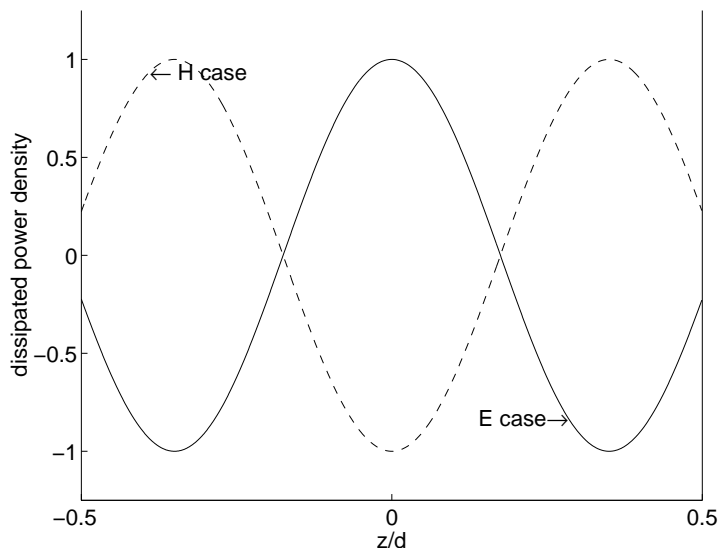


Figure 3.8: Comparison of dissipated power density along slab. In the E case, $A_1 = 1$ and $B_3 = 1$; In the H case, $A_1 = 1$ and $B_3 = -1$.

material is an imaginary one with $\epsilon_r = 1 - j1000$. This might be a semiconductor or a powdered form metal. Relevant parameters are list in Table 3.1, where d^* is the thickness which satisfies $\beta d^* = \pi$. The calculated results for impact factors f_1 , f_2 and \bar{p} are shown in Figs. 3.9, 3.10 and 3.11.

Table 3.1: Properties and parameters of materials

Material	ϵ_r	α	β	$d^*(cm)$
Al_2O_3	9.5-j0.0009	0.0078	152.15	2.06
beef	30.5-j9.6	44.6	283.7	1.11
imaginary material	1-j1000	1148.01	1148.83	0.27

From the results, we can see that P in the H case is larger than that in the E case if the thickness of the material is around d^* . For dielectric materials, d^* is of cm order while for semiconductors, d^* is of mm order.

The above discussion cannot be regarded as a full explanation of the experimental results since the heating in the cavity has different circumstances other than assumed here. The fields in a cavity are confined by metal plates at $\pm z$ direction. This example assumes that no boundary conditions are applied at $\pm z$. However, the field and power pattern inside the heated material should be similar.

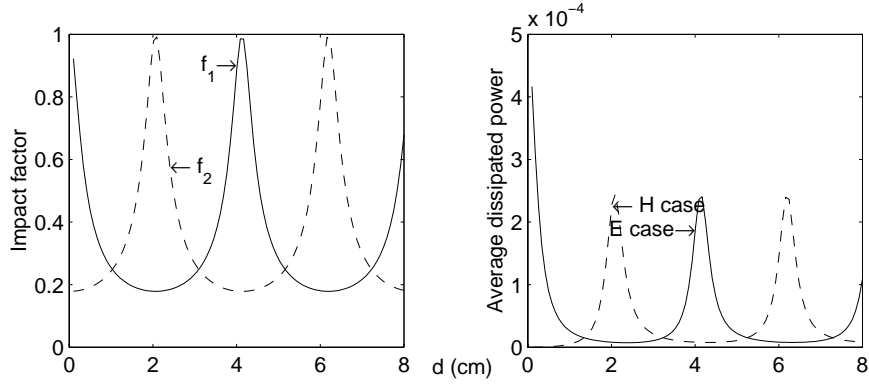


Figure 3.9: f_1 , f_2 and \bar{p} for Al_2O_3 in the E case and H case. The relative complex permittivity of Al_2O_3 is $9.5-0.0009j$. f_1 and f_2 are measures of the electric and magnetic fields at the center of the slab, respectively.

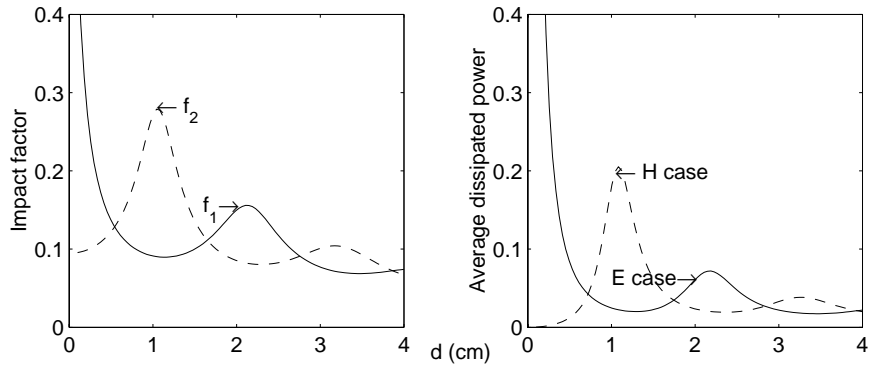


Figure 3.10: f_1 , f_2 and \bar{p} for beef in the E case and H case. The relative complex permittivity of beef is $30.5-9.60j$. f_1 and f_2 are measures of the electric and magnetic fields at the center of the slab, respectively.

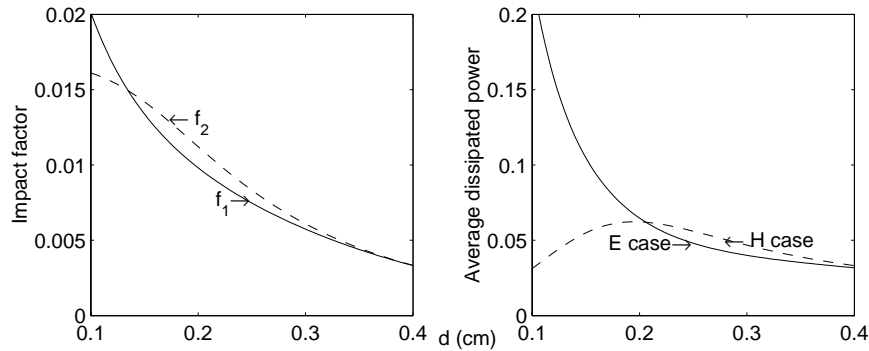


Figure 3.11: f_1 , f_2 and \bar{p} for an imaginary material in the E case and H case. The relative complex permittivity of this imaginary material is $1-j1000$. f_1 and f_2 are measures of the electric and magnetic fields at the center of the slab, respectively.

Chapter 4

Experiment Setup

The experimental setup was originated by Curtis^[19]. In his thesis, he gave a detailed description of the experimental setup and measurement techniques. In this chapter, we will describe briefly the overall system first. The focus will be placed on the parts that have been changed since Curtis' work. Also, the working principle of a resonant cavity will be discussed.

4.1 Overall System

The apparatus used for the experiments includes a power supply, remote microwave launcher (magnetron), circulator, water load, WR-284 copper waveguide cavity with coupling iris, waveguide, adjustable end-wall short, and power and temperature measurement equipment. The layout of the experimental components is shown in Fig. 4.1.

The microwave generator includes both the power supply and the remote launcher. The microwave system is powered by a Cober SM 1545D power supply and CWM-4-S magnetron, which can supply up to 3 kW to the applicator. The magnetron is water cooled and launches the 2.45 GHz microwaves into a tapered WR-340 to WR-284 waveguide section. To protect the power generator from reflected power, the system is equipped with a circulator and water load.

To measure power, a Homer impedance analyzer (by Cober) is introduced

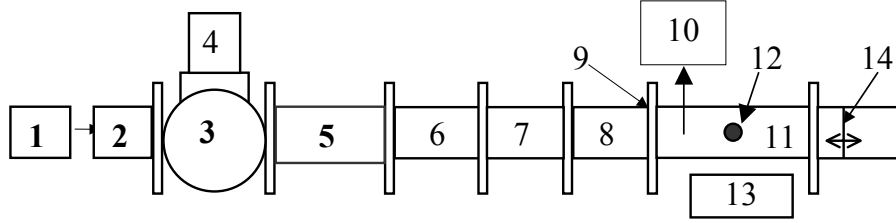


Figure 4.1: Schematic of experimental setup (top view). (1) Power Source; (2) Magnetron; (3) Circulator; (4) Water Load; (5) Waveguide Extension; (6) Four Stub Tuner; (7) Impedance Analyzer; (8) Waveguide with Wedge; (9) Iris; (10) Power Meter for Electric Field Measurement (11) Cavity; (12) Sample; (13) Pyrometer; (14) Adjustable End-wall Short.

into the system. The impedance analyzer can measure incident power, reflection coefficient, and frequency.

The electric field strength in the cavity is measured using a power sensor and associated power meter. The power sensor is coupled to the electric field through a small probe inserted slightly into the cavity. The magnitude of the electric field strength is proportional to the square root of the measured power; the constant of proportionality is determined by measuring the probe power in an empty cavity with no iris and a termination load replacing the sliding short.

To precisely monitor the microwave heating process, two infrared radiation pyrometers (Heitronics KT 15.82D and KT 15.01D) were chosen. While the KT 15.82D is used to measure temperatures within a range of 0-500°C, the KT 15.01D can measure temperatures within the range 350-2200°C. A radiation pyrometer measures the infrared radiation emitted by a surface; given the emissivity ϵ of the surface being measured, the temperature of the surface can be determined. The materials to be tested in this experimental program have emissivities that change significantly as a function of temperature. Varying the emissivity used by the pyrometer during an experiment is not practical since it must be done manually. Instead, the emissivity is set at 1.0 for the duration of the experiment, and the actual temperature is then determined from the measured temperature knowing the emissivity as a func-

tion of temperature for the material being heated^[19], a process which is performed automatically by the data acquisition software.

The resonant cavity is designed to operate in the TE_{10n} mode. Using the adjustable short, the cavity was adjusted to operate near the cavity resonance of the TE_{103} mode for all of the experiments. The cavity includes three parts: the waveguide, input coupling iris, and adjustable short. The position of the short plane ranges from 1.1 cm to 10.7 cm if measured from the waveguide flange. The sample to be heated was placed in a port located 17.5 cm from the cavity aperture, which means it is always very close to an electric field peak for the TE_{103} mode as illustrated in Fig. 4.2.

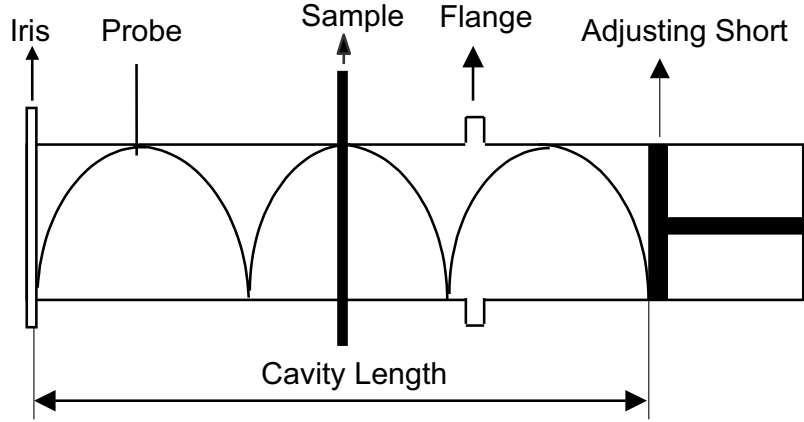


Figure 4.2: Schematic of TE_{103} mode cavity.

4.2 Electric Field Measurement

A small probe inserted slightly into the cavity was used to measure the electric field. The value of the field cannot be read directly; instead, through a power sensor, the value of the electric field was converted to a value of power, which can be read on a power meter. Since electric field is proportional to the square root of power, the electric field can be obtained through the equation

$$E_{meas} = C\sqrt{P_{read}}, \quad (4.1)$$

4.3 The Short with a Spin Dial

One improvement in our current setup is that we use a short with a spin dial to replace the sliding short used by Curtis^[19]. By reading the number on the dial, the position of the short plane can be determined, thus the cavity length can be calculated. Knowing the cavity length is very important for the experiments conducted in a single mode cavity.

The relation between the dial reading and the cavity length is given in Table 4.1. By a least squares fit, a linear relation is found as

Table 4.1: The relation between dial reading and cavity length

Dial reading	0	0.5	1	1.5	2	2.5
Depth from flange (cm)	10.7	9.8	8.9	8.1	7.2	6.3
Cavity length (cm)	36.1	35.2	34.3	33.5	32.6	31.7
Dial reading	3	3.5	4	4.5	5	5.375
Depth from flange (cm)	5.4	4.6	3.7	2.8	1.9	1.1
Cavity length (cm)	30.8	30.0	29.1	28.2	27.3	26.5

$$CL = 36.11 - 1.77DR, \quad (4.4)$$

where CL is cavity length with units of cm and DR is the dial reading. The geometry relation is illustrated in Fig. 4.4, which also includes the locations of the point to measure the electric field and port to insert the rod.

4.4 Cavity

The cavity is the key part of this heating system because the power carried by the electromagnetic waves is converted to heat here. The most common type of cavity is the multimode cavity^[69]. At a given frequency, such a cavity can support numerous modes and the fields in the cavity are the summation of all excited modes. This makes the analysis of the field distribution difficult, especially after the introduction of the material. The multimode cavity has advantages such as low cost, simplicity of

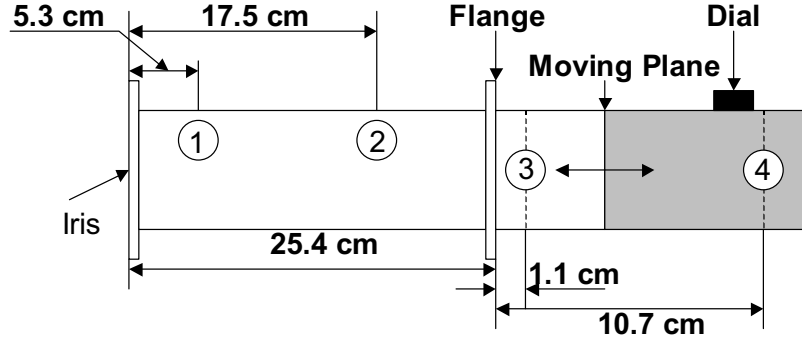


Figure 4.4: Cavity. (1) Location to measure electric field; (2) Location to insert heated rods; (3) Location of the short plane such that the cavity length is minimum; (4) Location of the short plane such that the cavity length is maximum.

construction and versatility^[20]. Detailed descriptions of multimode cavities can be found in several references^[61, 52]. In our experiments, single mode cavity is used.

Compared with a multimode cavity, only one mode is excited in a single mode cavity, so the electric field distribution is known accurately. One advantage of the single mode cavity is that the electric field can be much larger than that in a multimode cavity. Therefore, to heat small size low-loss materials, the single mode cavity is a natural choice.

An ideal single mode cavity is constructed of a piece of waveguide enclosed by two short planes. The electric field inside a lossless cavity could be infinite. In reality, fields can not be infinite even if the loss is not considered because one short plane must be replaced by an iris to couple the cavity to the waveguide. An iris is the same as a short plane except that there is a small aperture in it to allow microwaves to enter the cavity. A typical single mode cavity is illustrated in Fig. 4.5. The cavity used in our experiment is the same as the illustrated one except the iris shape. By choosing a suitable iris and adjusting the short plane, the cavity can be tuned to a resonant condition. Under the resonant condition, the electric field inside the cavity is much higher than the exciting field, which make it possible to heat the material efficiently.

In the following, we will discuss how such a cavity works through a multiple reflection viewpoint. The following procedure imitates an example in the book by Pozar^[58], who used multiple reflections to interpret the matching principle of a quarter-wave transformer.

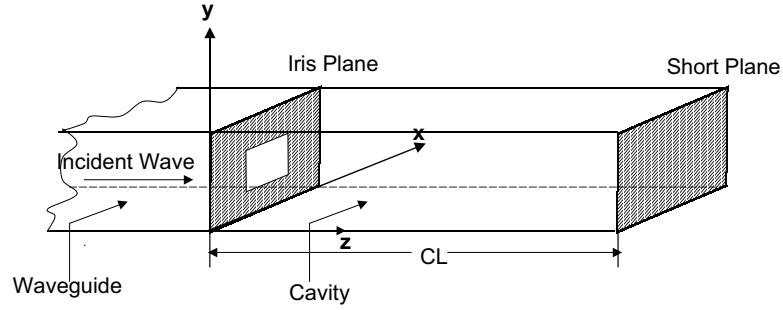


Figure 4.5: A single mode cavity

Suppose the reflection coefficient of the iris is Γ_{iris} . As an incident electric field with unity amplitude strikes the iris, part of the wave will be reflected, while the remainder will enter the cavity. Since only the TE_{10} mode wave can propagate through the cavity, we will neglect all higher order modes in the following discussion, so the wave can be expressed as:

$$\text{incident wave} \quad E_{inc} = \sin\left(\frac{m\pi x}{a}\right)e^{-jk_{10}z}, \quad (4.5)$$

$$\text{reflected wave} \quad E_{refl} = \Gamma_{iris} \sin\left(\frac{m\pi x}{a}\right)e^{jk_{10}z}, \quad (4.6)$$

$$\text{transmitted wave} \quad E_{trans} = (1 + \Gamma_{iris}) \sin\left(\frac{m\pi x}{a}\right)e^{-jk_{10}z}. \quad (4.7)$$

where k_{10} is the wavenumber of TE_{10} mode and a is the waveguide width.

Now we will focus on the fields inside the cavity. The transmitted wave will propagate until it strikes the short plane to induce the first reflected wave propagating in the $-z$ direction.

$$E_1 = A_1 \sin\left(\frac{m\pi x}{a}\right)e^{jk_{10}z}, \quad (4.8)$$

where A_1 is the complex amplitude. Since the short plane is considered a perfect electrical conductor, the electric field at the short plane should be zero. This condition gives

$$A_1 = -(1 + \Gamma_{iris})e^{-2jk_{10}CL}, \quad (4.9)$$

where CL is the cavity length. The transmitted and the first reflected waves create a standing wave as

$$\begin{aligned} S_1 &= (1 + \Gamma_{iris}) \sin\left(\frac{m\pi x}{a}\right) e^{-jk_{10}z} + A_1 \sin\left(\frac{m\pi x}{a}\right) e^{jk_{10}z} \\ &= -2j(1 + \Gamma_{iris})e^{-jk_{10}CL} \sin\left(\frac{m\pi x}{a}\right) \sin[k_{10}(z - CL)]. \end{aligned} \quad (4.10)$$

When the first reflected wave encounters the iris plane, it will produce the second reflected wave which will propagate along $+z$ direction, that is

$$\begin{aligned} E_2 &= \Gamma_{iris}A_1 \sin\left(\frac{m\pi x}{a}\right) e^{-jk_{10}z} \\ &= -\Gamma_{iris}(1 + \Gamma_{iris})e^{-2jk_{10}CL} \sin\left(\frac{m\pi x}{a}\right) e^{-jk_{10}z}. \end{aligned} \quad (4.11)$$

Comparing this wave with the transmitted wave in Eq. (4.7), we see that the standing wave produced by it is

$$S_2 = -2j(1 + \Gamma_{iris})e^{-jk_{10}CL}(-\Gamma_{iris}e^{-2jk_{10}CL}) \sin\left(\frac{m\pi x}{a}\right) \sin[k_{10}(z - CL)]. \quad (4.12)$$

The total field inside the cavity is the summation of all these standing waves produced by multiple reflection, as illustrated in Fig. 4.6.

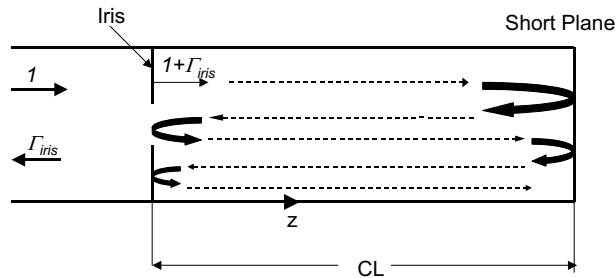


Figure 4.6: Cavity: multiple reflection viewpoint

By summing all the standing waves, the total field inside the cavity is found to be

$$\begin{aligned}
S &= -2j(1 + \Gamma_{iris})e^{-jk_{10}CL} \sin\left(\frac{m\pi x}{a}\right) \sin[k_{10}(z - CL)] \sum_{i=1}^{\infty} (-\Gamma_{iris}e^{-2jk_{10}CL})^{i-1} \\
&= -2j \frac{(1 + \Gamma_{iris})e^{-jk_{10}CL}}{1 + \Gamma_{iris}e^{-2jk_{10}CL}} \sin\left(\frac{m\pi x}{a}\right) \sin[k_{10}(z - CL)].
\end{aligned} \tag{4.13}$$

For the coupling through a small aperture, Γ_{iris} can be approximated by $|\Gamma_{iris}|e^{j\theta}$, where $|\Gamma_{iris}| \simeq 1$ and $\theta \simeq \pi$. For example, the calculated value of Γ_{iris} of the iris used in our experiment by moment methods is $-0.985 + j0.121$. Using this number, we can calculate the peak value of the electric field inside the cavity as a function of the cavity length CL as

$$S_{peak} = 2 \frac{|1 + \Gamma_{iris}|}{|1 + \Gamma_{iris}e^{-2jk_{10}CL}|}. \tag{4.14}$$

The calculated result is illustrated in Fig. 4.7. There are some points that need

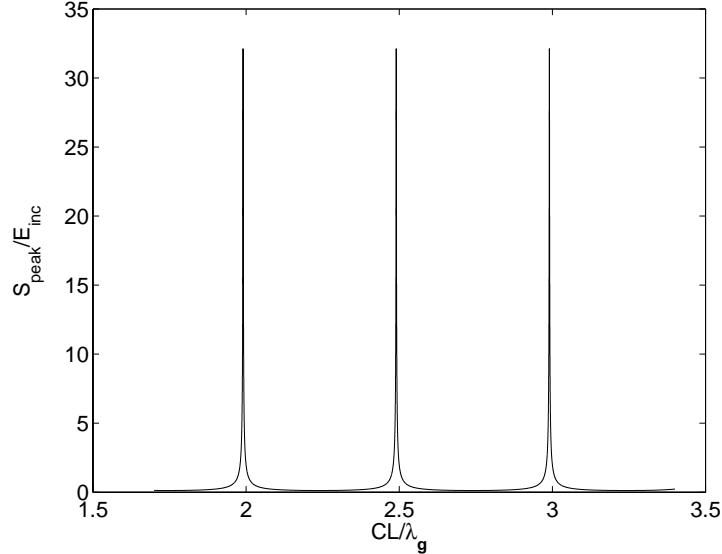


Figure 4.7: Peak electric field inside the cavity varied with the cavity length

to be mentioned here:

- The electric field has finite value even when loss is not included in the system.
- The peak value of the electric field is much larger than the incident value. In this example, it is more than 33 times the magnitude of the incident wave.

- The cavity is said to be tuned when the electric field inside the cavity is very large. From Fig. 4.7, the cavity is tuned when the cavity length is near an integer multiple of a half wavelength.
- From Eq. (4.13), it appears that at a resonant condition, the electric field is near zero at $z = 0$, where the iris is located, because the cavity length is near an integer multiple of a half wavelength. However, around a discontinuity, many higher order modes exist besides the TE_{10} mode, so the field at that location cannot be expressed by Eq. (4.13).

In our experiments, the microwave power source operates at 2450 MHz; correspondingly, the wavenumber k_{10} and wavelength λ_g of the TE_{10} mode are 27.2 m^{-1} and 23.1 cm. From Table 4.1, the cavity length ranges from 26.5 cm to 36.1 cm, which are equal to $1.15\lambda_g$ and $1.56\lambda_g$, respectively. Therefore, the empty cavity can be tuned to a TE_{103} resonant state, as illustrated by Fig. 4.2. According to Fig. 4.4, the distances between the iris plane and the positions of the probe and the rod are equal to $0.23\lambda_g$ and $0.76\lambda_g$. Since a *sin* function varies slowly around its maximum value, these two locations can be thought to be at electric field peaks.

4.5 Data Acquisition

The data acquired from pyrometers and power meters were transferred to a computer through a AT-MIO-16F-5 or a Lab-PC+ data acquisition board (by National Instruments). The data acquired from the Homer impedance analyzer were transferred to a computer through an RS-232 port. All collected data are processed by Labview software. Data were acquired at 1 second intervals.

Chapter 5

Experimental Results

This chapter shows the experimental results for microwave heating of mullite and alumina rods. Both are important ceramic materials in industry and are known to be thermal runaway materials. In Section 5.1, heating of a mullite rod with a diameter of 4.5 mm is described. The detailed heating process and method to avoid thermal runaway are provided. Also in this section, three critical points in the heating process are identified. In Section 5.2, we present the experimental results for heating of an alumina rod with a diameter of 4.5 mm. Then in the following two sections, we briefly show the effects of the output power of the generator and the size of the rod to the heating process.

In all experiments, the rod is inserted into the cavity through two holes on the broad sides of the waveguide, so that the rod is aligned parallel to the electric field, as illustrate in Fig. 4.2.

5.1 Experimental Results for 4.5 mm Mullite Rod

The experimental results for a mullite rod with a diameter of 4.5 mm and a length of 30.5 cm are shown in Figs. 5.1 and 5.2. Since the height of the cavity is only 3.4 cm, only a small portion of the rod is in the cavity. The output of the power generator is set to 600 W, and is not changed during the experiment. The only adjustable component in the system is the position of the short plane, which changes the cavity

length.

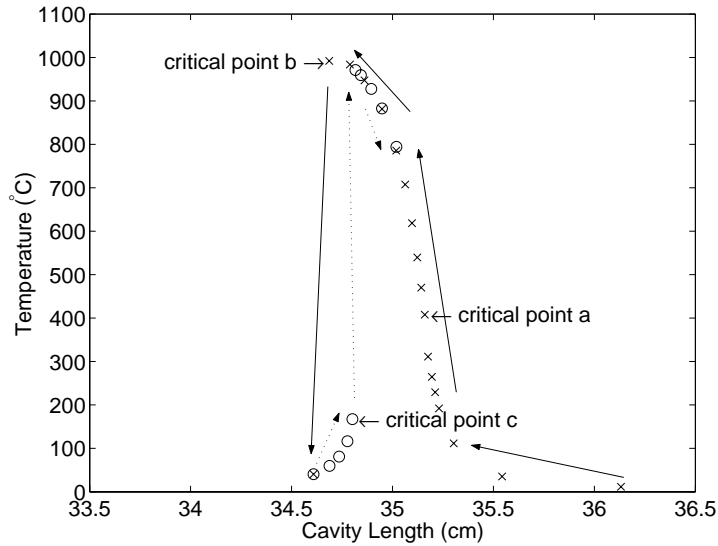


Figure 5.1: Behavior of the rod temperature when the position of the shorting plane was adjusted. In the figure, the stable states obtained by decreasing and increasing the cavity length are denoted by the “ × ” and “ o ” symbols, respectively.

The experiment starts from a cavity length of 36.1 cm where the cavity is highly detuned. As Figs. 5.1 and 5.2 show, at the beginning of the experiment the rod is at ambient temperature. When the short is adjusted to decrease the length of the cavity, the temperature of the rod increases, as well as the electric field strength at the plane of the rod. Continuing to decrease the cavity length leads to critical point *a*, which is the point at which the maximum electric field strength is reached. From this point, the electric field strength always decreases independent of the direction of changes to the short plane position.

If we change the short plane position to increase the length of the cavity, then temperature and electric field strength decrease simultaneously to a new equilibrium point on the same curve. If we very gently adjust the short to decrease the length of the cavity further, the temperature of the rod will increase but the electric field strength will decrease due to the increased power absorption, leading to a new equilibrium point at higher temperature. If we continue decreasing the length of the cavity, the field in the cavity will collapse at critical point *b*. Both the temperature of the rod

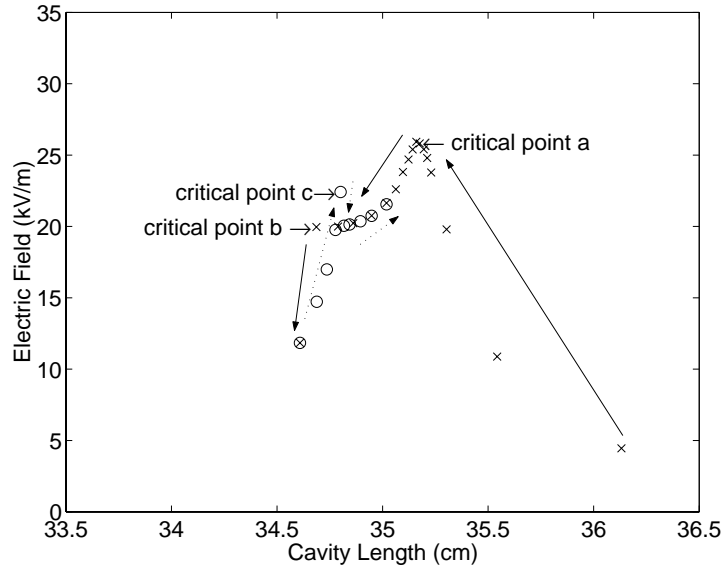


Figure 5.2: Behavior of the electric field for the same experiment shown in Figure 5.1.

and the field intensity will drop dramatically, leading to equilibrium at a much lower temperature; this process is like reverse thermal runaway. All the points plotted in Figs. 5.1 and 5.2 represent stable states, and are denoted by the “ \times ” symbol. The whole process path is denoted by the solid arrow.

To heat the rod from the lower temperature point, where the cavity length is 34.6 cm, we must increase the cavity length. The temperature and the field will both increase along another curve that does not coincide with the original one. At critical point c , another electric field maximum is encountered. If the length of the cavity is increased from point c , a temperature excursion occurs. The temperature continues increasing and the field continues decreasing until an equilibrium point is reached that has much higher temperature and lower electric field strength. Notice that at the end of this process the field decreases rather than increases. If we continue to increase the length of the cavity, the temperature will decrease but the field will increase, and the equilibrium point curve will coincide with the original curve. All the stable points are denoted by the “ \circ ” symbol, while the process path is denoted by a dashed arrow.

In Fig. 5.3, we collect the equilibrium points from Figs. 5.1 and 5.2 to plot

temperature *vs.* electric field strength. This shows clearly the lower and middle branches of the S-curve.

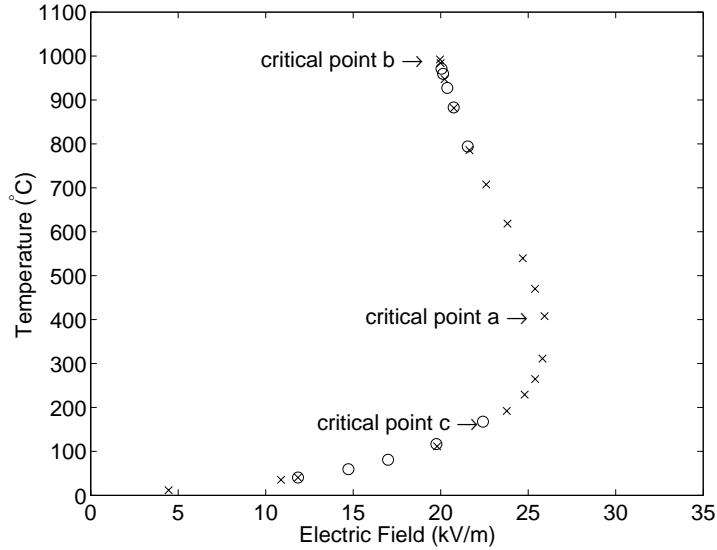


Figure 5.3: Plot of the temperature versus electric field for a mullite rod with a 4.5 mm diameter heated at 600 W.

5.1.1 Typical Heating Processes

There are 4 typical heating processes at constant power level. To illustrate the processes clearly, each is discussed and plotted on the S-curve in the following paragraphs.

Decreasing the Cavity Length

The process starts from an equilibrium point, and is illustrated in Fig. 5.4. When the cavity length is decreased, the electric field strength increases immediately while the temperature of the rod is nearly unchanged. When the rod heating begins, the cavity is detuned by the increasing dielectric loss of the rod resulting from the heating process. If the starting point is below the critical point *a*, this process will end at an absolutely stable point.

If the starting point is above the critical point *a*, the process will end at a relatively stable point. It is well known that all equilibrium points above the critical

point a are unstable as viewed from the energy balance since it cannot tolerate any small perturbation. But the process is governed by Maxwell's equations as well as the energy balance. When the system attempts to escape from the equilibrium point, changes in the cavity field will force it back and the state will fluctuate around the equilibrium point.

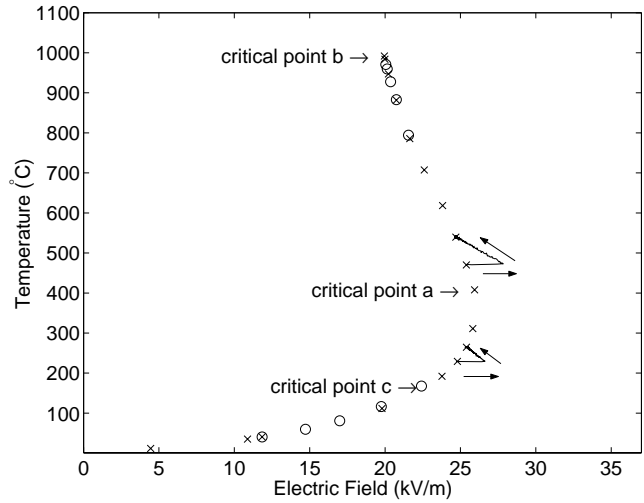


Figure 5.4: The transient behavior of electric field and temperature for decreasing cavity length. This behavior is illustrated for two different starting points. The arrows illustrate the dynamic heating process observed in the experiments.

Increasing the Cavity Length

As illustrated in Fig. 5.5, when increasing the cavity length, the rod can be heated or cooled depending upon the starting point. If the starting point is below the critical point c , the cavity will continue being tuned and the temperature will increase. If the starting point is above the critical point, the cavity is detuned first, but as the temperature increases, the cavity is moved toward the tuned state.

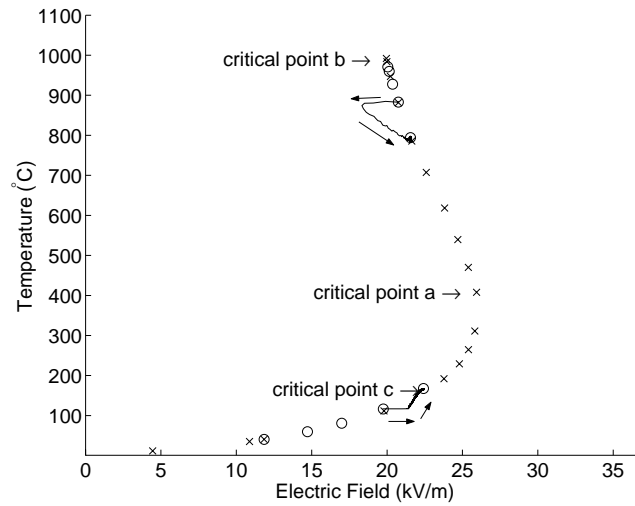


Figure 5.5: The transient behavior of electric field and temperature for increasing cavity length. This behavior is illustrated for two different starting points. The arrows illustrate the dynamic heating process observed in the experiments.

Thermal Excursion

If the cavity length is increased from critical point c, a rapid temperature excursion occurs in a rather complicated process. Although the temperature increases almost continuously, the field intensity does not vary monotonically. As illustrated by Fig. 5.6, the cavity is first highly tuned and the temperature increases rapidly. When the field intensity reaches its maximum value, the temperature increases dramatically during a very short time. In our experiments, the temperature increases more than 500 degrees in less than half a minute, causing the cavity to become detuned. At the end of the process, the temperature drops slightly to the equilibrium curve.

Reverse Thermal Runaway

If we decrease the length of cavity from the critical point b, a “reverse thermal runaway” occurs. The field strength decreases slightly, but the temperature drops precipitously, as illustrated in Fig. 5.7.

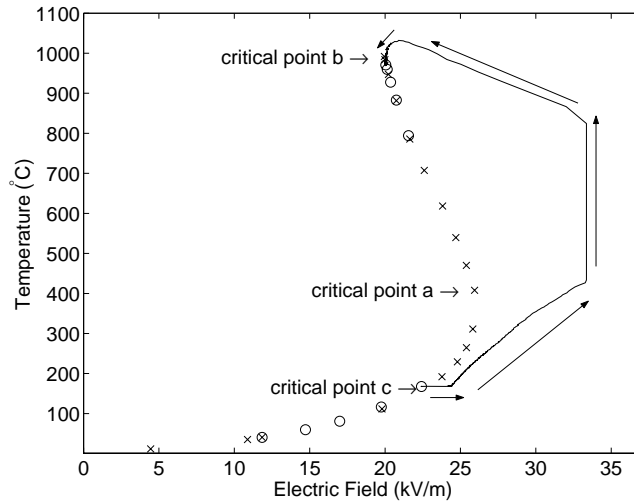


Figure 5.6: Behavior of the electric field and temperature when the cavity length is increased from critical point *c*. The temperature excursion mimics thermal runaway, but a stable equilibrium point is achieved at high temperature.

5.2 Experimental Results for 4.5 mm Alumina Rod

The experimental results for an alumina rod of 99.9% purity with a diameter of 4.5 mm and a length of 20.3 cm are shown in Fig. 5.8. The output of the power generator is set to 300 W, and is not changed during the experiment. The same procedures as we followed for the mullite rod were repeated. As shown in Figure 5.8, similar behavior of the temperature and the electric field was observed. By decreasing the cavity length through adjustments to the short plane position, the rod can be stabilized at any temperature. However, if the cavity length is increased, thermal excursion occurs. Compared with the experiment results for the mullite rod, we observed a full S-curve. This curve is illustrated in Figure 5.9.

5.3 Power Level Effects

If the output of the power generator is set too high, part of the middle branch of the S-curve becomes unstable. An example for a mullite rod with a diameter of 4.5 mm is shown in Fig. 5.10. In the experiment, the output of the power generator is set to 2000 W. It is observed the temperature cannot be stabilized in the range of 413°C to

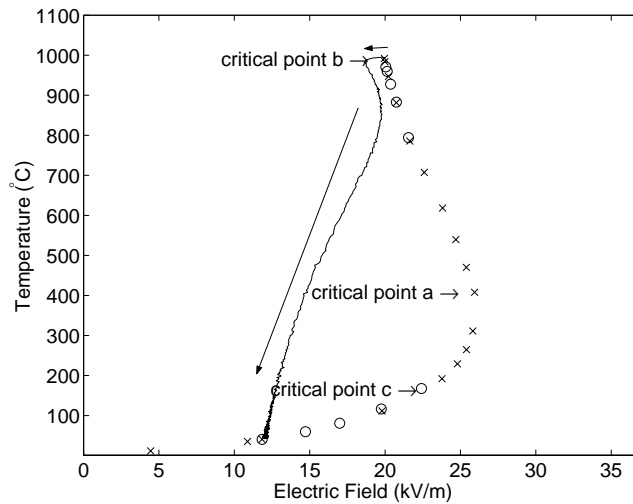


Figure 5.7: Rapid temperature decrease following a decrease in cavity length from critical point *b*.

992°C. For comparison, we include the stable curve obtained at low power level.

A similar unstable behavior is also observed when heating the alumina rod. As the output of the power generator is set to 700 W, the whole middle branch of the S-curve becomes unstable. The experimental results are shown in Fig. 5.11.

5.4 Rod Size Effects

When the diameter of the rod increases, it is found to be difficult to heat the rod using our current apparatus. Fig. 5.12 shows the experimental results of heating an alumina rod with diameter of 9 mm. From the figure, it appears that to heat the rod to a specified temperature, the required electric field is lower than that for heating of a thinner rod. However, much higher input power is required to attain this lower electric field. For example, when heating the alumina rod with a diameter of 4.5 mm, 700 W input power is sufficient to heat the rod to more than 1000°C. If the diameter of the rod increases to 9 mm, the input power has to be set to 1600 W. Another difficulty is that arcing occurs frequently.

In our experiment, no unstable behavior was observed for this alumina rod.

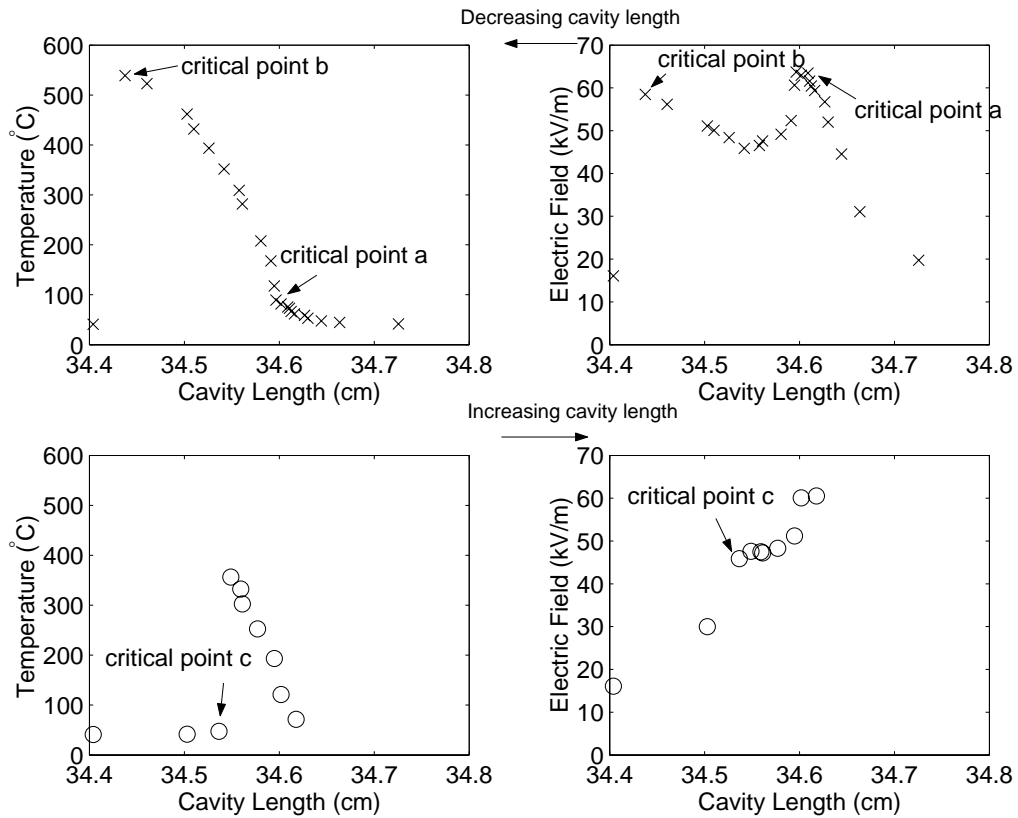


Figure 5.8: Behavior of the alumina rod temperature and the electric field when the position of the shorting plane was adjusted. In the figure, the stable states obtained by decreasing and increasing the cavity length are denoted by the “ × ” and “ o ” symbols, respectively.

5.5 Summary

In this chapter, we report the direct experimental evidence of the so-called S-curve of temperature versus electrical field when materials with positive temperature dependence of dielectric loss are heated in a microwave field. A complete discussion of how the experimental results were achieved is presented. From the experimental results, the S-curve does exist for some materials. However, by the use of the resonant cavity, the unstable behavior of the S-curve can be controlled without the use of any other control system.

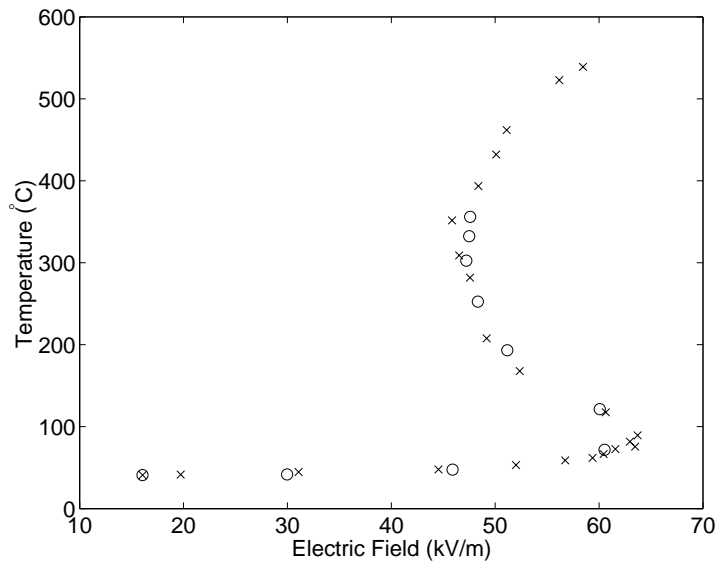


Figure 5.9: Plot of the temperature versus electric field for an alumina rod with a 4.5 mm diameter heated at 300 W. In the figure, the stable states obtained by decreasing and increasing the cavity length are denoted by the “ × ” and “ o ” symbols, respectively.

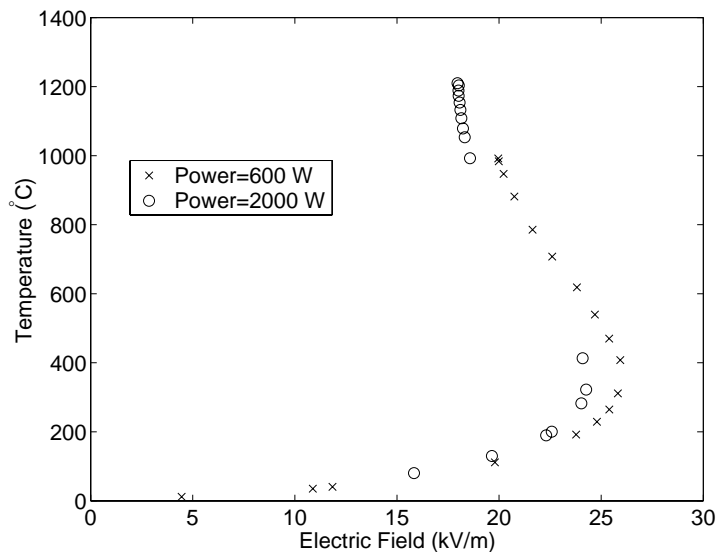


Figure 5.10: Part of the middle branch of the S-curve becomes unstable when heating the mullite rod with 2000 W input power. In the figure, the stable states obtained by decreasing and increasing the cavity length are denoted by the “ × ” and “ o ” symbols, respectively.

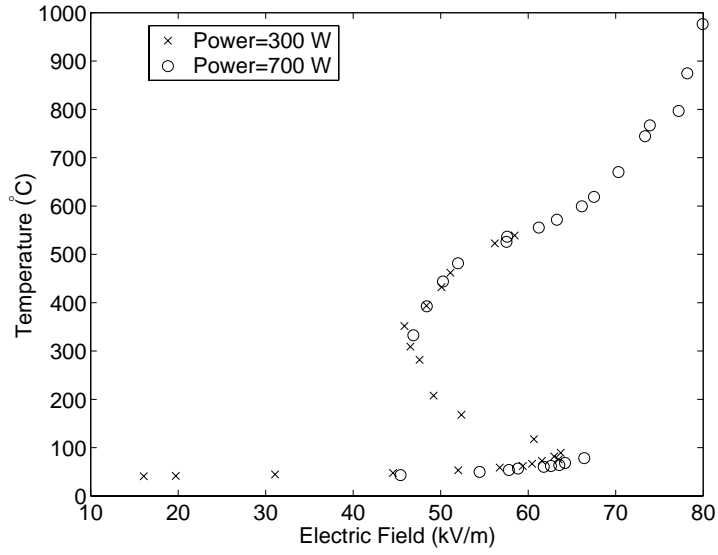


Figure 5.11: The middle branch of the S-curve becomes unstable when heating the alumina rod with 700 W input power. In the figure, the stable states obtained by decreasing and increasing the cavity length are denoted by the “ × ” and “ o ” symbols, respectively.

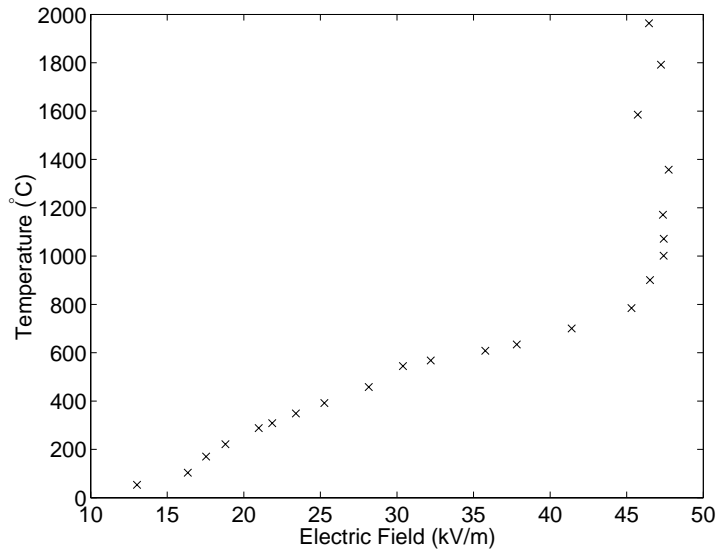


Figure 5.12: Plot of the temperature versus electric field for an alumina rod with a 9.0 mm diameter.

Chapter 6

Equivalent Circuit Model for the Microwave Heating System

To model microwave heating of ceramic rods in a single mode cavity, the electric field in the rod must be calculated. To simplify our modeling work, we consider the electric field inside the cavity only, ignoring all the components before the iris. The cavity is illustrated in Fig. 6.1. The incident wave is the TE_{10} mode with unity amplitude coming from the left. As it strikes the iris, some higher order modes are excited, some of which are reflected and others transmitted through the aperture. The transmitted wave will strike the heated rod and short plane, inducing other reflected waves. These waves will propagate to the left and be scattered by the iris again. The field in the cavity and waveguide will be the superposition of all these scattered modes.

The above analysis, considering a problem consisting of the iris, the heated rod and short plane all together, makes the problem unnecessarily complex since only the TE_{10} mode can propagate along the waveguide. If we treat the iris and rod as obstacles, the electric field far away from these obstacles will consist of only TE_{10} modes. The effects of higher order modes are important around the obstacles only, which provides a possible simple method to analyze the problem.

In this chapter, the S-matrix simplifications^[43] are introduced in Section 6.1. Using this method, we show that the calculation of the electric field in the cavity can be divided into two separate problems. One problem concerns the scattering property

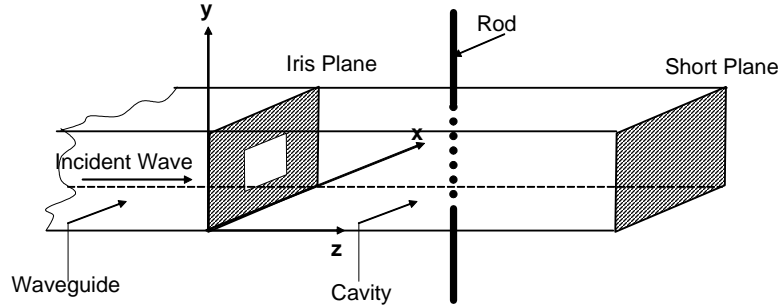


Figure 6.1: Cavity

of an iris in a homogeneous waveguide without any other obstacles, while the other problem concerns a waveguide terminated by the rod and short plane without the iris. Based on these results, some more general concepts on microwave networks are introduced in Section 6.2. By the use of these concepts, the obstacles along the waveguide can be modeled by lumped parameters and the overall heating system represented by an equivalent circuit. In Section 6.3, the equivalent circuit model is applied to the calculation of electric field pattern in an empty cavity, which has been discussed in Chapter 4 from a multireflection viewpoint. Finally, in Section 6.4 an equivalent circuit is used to model the overall heating system.

6.1 S-matrix Simplifications

To determine the electromagnetic field inside the cavity, we must find a solution to satisfy Maxwell's equations as well as all boundary conditions. The solution of Maxwell's equations in the empty waveguide are well documented^[2]. They are constructed by the superposition of eigenfunctions (also called modes), which satisfy the differential equations as well as the boundary conditions on all PECs (Perfect Electric Conductor). What we need to do is to determine the complex amplitude of these modes so that they satisfy the boundary conditions introduced by the iris, rod, and short.

Far away from these obstacles, only the TE_{10} mode exists in the waveguide. To

make a quantitative estimation, suppose there is an imaginary plane placed between and equal distance from the iris and the rod, as illustrated by Fig. 6.2. In our experimental setup, the distance between the iris plane and the heated rod, L_1 , is 17.5cm. The mode decaying most slowly is TE_{20} , whose wavenumber is $70.4m^{-1}$. After propagating the length $L_1/2$, the wave with unity amplitude originating at the rod or iris plane diminishes to $e^{-\gamma_{20}L_1/2}$, which is around 0.0021. If we recall that the electric field in a cavity is constructed of the multiply reflected waves, we can conclude that all higher order modes make little contribution to the overall structure of the electric field in the cavity. Therefore, to get the field pattern, we only need to study the behavior of the TE_{10} mode.

The electric field due to the TE_{10} mode in the section between the iris and the rod can be expressed as

$$E_{im} = (Fe^{-jk_{10}z} + Be^{jk_{10}z}) \sin\left(\frac{\pi x}{a}\right), \quad (6.1)$$

where F and B are the complex amplitudes for the TE_{10} mode propagating in $+z$ and $-z$ directions.

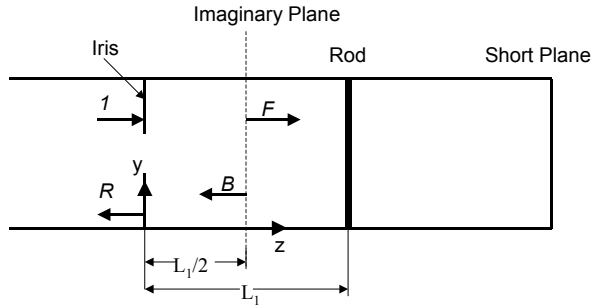


Figure 6.2: Imaginary Plane

The electric field to the left and far away from the iris plane can be written as

$$E_{left} = (e^{-jk_{10}z} + Re^{jk_{10}z}) \sin\left(\frac{\pi x}{a}\right), \quad (6.2)$$

where R is the complex amplitude for the TE_{10} mode propagating in $-z$ direction, which includes the effects of the iris, rod and short plane.

To use S-matrix simplifications, we first focus on the region to the left of the imaginary plane. This is an overdetermined scattering problem since we have specified too many conditions. Some relations must exist among F , B and R . If we assume the reflection coefficient of the iris in a homogeneous waveguide without any other obstacle is Γ_{iris} , the relations can be constructed as follows:

- The second term in Eq. (6.2), which is a TE_{10} wave traveling in $-z$ direction, can be regard as the summation of the reflection of the first term in Eq. (6.2) and the transmission of the second term in Eq. (6.1), that is

$$R = \Gamma_{iris} + (1 + \Gamma_{iris})B. \quad (6.3)$$

- The first term in Eq. (6.1), which is a TE_{10} wave traveling in the $+z$ direction, can be regarded as the summation of the reflection of the second term in Eq. (6.1) and the transmission of the first term in Eq. (6.2), that is

$$F = \Gamma_{iris}B + (1 + \Gamma_{iris}). \quad (6.4)$$

In the above expressions, we have used the relation that $T_{iris} = 1 + \Gamma_{iris}$, where T_{iris} is the transmission coefficient of the iris. This relation holds since we assume the thickness of the iris is zero.

Next if we consider the region between the imaginary plane and short plane, the relation between F and B can be expressed as

$$B = \Gamma_{rs}F. \quad (6.5)$$

where Γ_{rs}^1 is the complex amplitude of the reflected TE_{10} mode wave if a TE_{10} mode wave with unity amplitude strikes the rod and short.

Combining Eqs. (6.4) and (6.5), we obtain

$$F = \frac{1 + \Gamma_{iris}}{1 - \Gamma_{iris}\Gamma_{rs}}, \quad (6.6)$$

and

$$R = \Gamma_{iris} + (1 + \Gamma_{iris})\Gamma_{rs} \frac{1 + \Gamma_{iris}}{1 - \Gamma_{iris}\Gamma_{rs}}. \quad (6.7)$$

¹ Γ_{rs} is defined at the $z = 0$ plane.

From Eqs. (6.6) and (6.7), it is clear that the field structure can be determined by two parameters, Γ_{iris} and Γ_{rs} . The system has been separated into two subsystems. First, we need to calculate the reflection coefficient of an iris in a homogeneous waveguide. Secondly, we need to calculate the electric field inside a cylindrical rod which is irradiated by an electric wave with amplitude F . The iris has been excluded from this subsystem. The effects of the iris are included in Eq. (6.6) through Γ_{iris} .

Indeed, the second subsystem, which includes the rod and the short, can be further divided if the multireflections arising from higher order modes between them can be neglected. A general conclusion is that in a microwave heating system, all obstacles can be handled individually. This conclusion is based on the assumptions that the higher order modes generated from one obstacle have negligible effects on other obstacles.

The effect of an obstacle is twofold. It generates a far field consisting of only the TE_{10} mode and it also produces a local field consisting of exponentially attenuated higher order modes. For different obstacles, we have different interests. For example, in microwave heating problems, we do not care about the local field around the iris; but the local field produced by the rod is important. If we solve Maxwell's equation in the whole region, we will obtain too much information. Instead, we can use circuit analysis combined with necessary local analysis to obtain what we really want.

6.2 Equivalent Circuit for a Two-port Microwave Network

Fig. 6.3 shows an obstacle located at $z = 0$ in a waveguide. If there are no other obstacles, then only the TE_{10} mode exists as $z \rightarrow -\infty$, and the fields can be represented as

$$E_{1y} = \sqrt{\frac{2}{a}} \sin \frac{\pi x}{a} V_1(z), \quad (6.8)$$

and

$$H_{1x} = -\sqrt{\frac{2}{a}} \sin \frac{\pi x}{a} I_1(z), \quad (6.9)$$

where $V_1(z)$ and $I_1(z)$ are equivalent voltage and current.

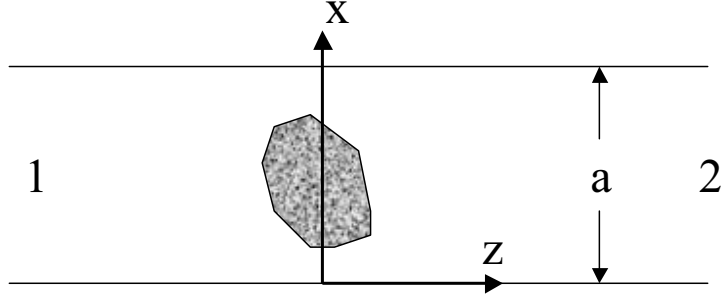


Figure 6.3: An arbitrary obstacle in the waveguide

By substituting these expressions into Maxwell's equations, the equations for $V_1(z)$ and $I_1(z)$ can be obtained as

$$\frac{d^2 V_1(z)}{d^2 z} + k_{10}^2 V_1(z) = 0, \quad (6.10)$$

$$\frac{d^2 I_1(z)}{d^2 z} + k_{10}^2 I_1(z) = 0, \quad (6.11)$$

where k_{10} is the wavenumber for the TE_{10} mode. These equations are the well-known transmission line equations^[58]. The traveling wave solutions are

$$V_1(z) = V_1^+ e^{-k_{10}z} + V_1^- e^{k_{10}z}, \quad (6.12)$$

$$I_1(z) = I_1^+ e^{-k_{10}z} - I_1^- e^{k_{10}z}, \quad (6.13)$$

where $V_1(z)$ and $I_1(z)$ are equivalent voltage and current. The constants V_1^+ and V_1^- are related to I_1^+ and I_1^- through

$$\frac{V_1^+}{I_1^+} = \frac{V_1^-}{I_1^-} = \frac{\omega\mu}{k_{10}} = Z_0, \quad (6.14)$$

where Z_0 is the characteristic impedance of the transmission line.

The same procedure can be applied to the far fields to the right of the obstacle and similar results can be obtained as

$$V_2(z) = V_2^+ e^{k_{10}z} + V_2^- e^{-k_{10}z}, \quad (6.15)$$

$$I_2(z) = I_2^+ e^{k_{10}z} - I_2^- e^{-k_{10}z}. \quad (6.16)$$

Notice that the sign is changed in the exponential terms because V_i^+ is always used to represent the amplitude of a wave traveling toward the obstacle.

Mathematically, such transformations just drop the x variation of the fields. The reason to do this is that there are many useful results in the circuit theory which can make the analysis simple and intuitive.

Next we consider the voltage and current at the $z = 0$ plane where the obstacle is located. We use V_1 and I_1 to represent the voltage and current extrapolated back to the $z = 0^-$ plane from $-\infty$, V_2 and I_2 to represent the voltage and current extrapolated back to the $z = 0^+$ plane from $+\infty$. Due to the presence of the obstacle, normally $V_1 \neq V_2$ and $I_1 \neq -I_2$. The voltages are related to the currents through

$$\begin{bmatrix} V_1 \\ V_2 \end{bmatrix} = \begin{bmatrix} Z_{11} & Z_{12} \\ Z_{21} & Z_{22} \end{bmatrix} \begin{bmatrix} I_1 \\ I_2 \end{bmatrix}, \quad (6.17)$$

or

$$[V] = [Z] [I], \quad (6.18)$$

where the impedance matrix $[Z]$ is determined by the properties of the obstacle. If the network is reciprocal, $[Z]$ is symmetric^[58]. One equivalent circuit to represent this two-port network is illustrated in Fig. 6.4.

The impedance matrix $[Z]$ is convenient when analyzing the network problem. However, when an obstacle is analyzed by a mode matching method, a scattering matrix is used rather than an impedance matrix. A scattering matrix $[S]$ relates the amplitudes of the incident wave to the amplitudes of reflected waves as

$$\begin{bmatrix} V_1^- \\ V_2^- \end{bmatrix} = \begin{bmatrix} S_{11} & S_{12} \\ S_{21} & S_{22} \end{bmatrix} \begin{bmatrix} V_1^+ \\ V_2^+ \end{bmatrix}, \quad (6.19)$$

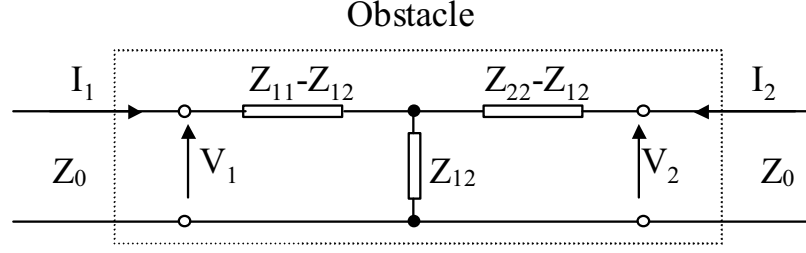


Figure 6.4: An equivalent circuit for a two-port microwave network

or

$$[V^-] = [S] [V^+]. \quad (6.20)$$

Since both $[Z]$ and $[S]$ describe the properties of the obstacle, they are not independent. Their relations are^[58]

$$\frac{Z_{11}}{Z_0} = \frac{(1 + S_{11})(1 - S_{22}) + S_{12}^2}{\Delta S}, \quad (6.21)$$

$$\frac{Z_{12}}{Z_0} = \frac{2S_{12}}{\Delta S}, \quad (6.22)$$

$$\frac{Z_{22}}{Z_0} = \frac{(1 - S_{11})(1 + S_{22}) + S_{12}^2}{\Delta S}, \quad (6.23)$$

where

$$\Delta S = (1 - S_{11})(1 - S_{22}) - S_{12}^2. \quad (6.24)$$

In the above expressions, we have used the property that if $[Z]$ is symmetric, then $[S]$ is symmetric.

In our microwave heating system, both the iris and the rod are two-port networks. Since they are both symmetrical about the $z = 0$ plane, then $Z_{11} = Z_{22}$ and $S_{11} = S_{22}$. In the iris case, since the electric field is continuous across the iris (we suppose that the thickness of the iris is zero), then $V_1 = V_2$. From Eq. (6.17), we obtain that $Z_{11} = Z_{12}$. Therefore, the series arms in the equivalent circuit are absent.

In conclusion, when we use equivalent circuits to represent the rod, two complex numbers, Z_{11} and Z_{12} , need to be determined; in the iris case, only one complex number, Z_{12} , needs to be determined.

6.3 Analysis of the Cavity from an Equivalent Circuit Viewpoint

The analysis of a cavity from a multiple reflection viewpoint has been discussed in Chapter 4. That method gives a physically clear picture of the electric field inside the cavity. However, the problem can be also handled with an equivalent circuit model as illustrated in Fig. 6.5. In this model, the iris is treated as a lumped parallel

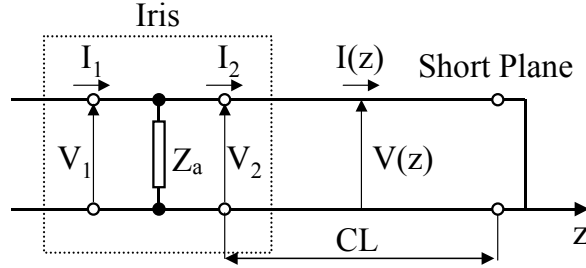


Figure 6.5: Cavity: transmission line model

impedance and the waveguide as a section of transmission line.

Suppose that Γ_{iris} is given; then $S_{11} = \Gamma_{iris}$ and $S_{12} = 1 + \Gamma_{iris}$. By putting these into Eq. (6.22), the normalized impedance z_a can be calculated as

$$z_a = \frac{Z_a}{Z_0} = \frac{2S_{12}}{\Delta S} = -\frac{1 + \Gamma_{iris}}{2\Gamma_{iris}}. \quad (6.25)$$

The normalized input impedance of a transmission line terminated in a short circuit is

$$z_{in} = \frac{Z_{in}}{Z_0} = j \tan(k_{10}CL), \quad (6.26)$$

where CL is the length of the cavity or the length of the transmission line.

The equivalent total normalized impedance including the iris and the short circuit is

$$z_t = \frac{Z_t}{Z_0} = \frac{1}{\frac{1}{z_a} + \frac{1}{z_{in}}} = \frac{j \tan(k_{10}CL)z_a}{j \tan(k_{10}CL) + z_a}. \quad (6.27)$$

From the transmission line theory^[58], the total reflection coefficient seen from the iris is

$$\Gamma_t = \frac{z_t - 1}{z_t + 1}. \quad (6.28)$$

The amplitude of the incident electric field or the equivalent incident voltage, V_1^+ , is supposed to be unity, so the amplitude of the total electric field or the total voltage just before the iris is

$$V_1 = V_1^+ + V_1^- = V_1^+ + V_1^+\Gamma_t = V_1^+(1 + \Gamma_t) = 1 + \Gamma_t, \quad (6.29)$$

and the corresponding current is

$$I_1 = I_1^+ - I_1^- = \frac{V_1^+ - V_1^-}{Z_0} = \frac{V_1^+}{Z_0}(1 - \Gamma_t) = \frac{1 - \Gamma_t}{Z_0}, \quad (6.30)$$

Across the iris, the total voltage will not change while the total current will be

$$I_2 = I_1 - \frac{V_1}{Z_a} = \frac{1 - \Gamma_t}{Z_0} - \frac{1 + \Gamma_t}{Z_a}. \quad (6.31)$$

Since V_2 and I_2 are the total voltage and current at one point in a transmission line with fixed impedance Z_0 and wave number k_{10} , the total voltage at all other points along the transmission line can be determined. Suppose the iris is at the point of $z = 0$; then the total voltage at z is

$$\begin{aligned} V(z) &= V_2 \cos(k_{10}z) - jI_2Z_0 \sin(k_{10}z) \\ &= (1 + \Gamma_t) \cos(k_{10}z) - j \left[(1 - \Gamma_t) - \frac{1}{z_a}(1 + \Gamma_t) \right] \sin(k_{10}z). \end{aligned} \quad (6.32)$$

By putting the expressions for Γ_t and z_a in the above equation, we obtain

$$V(z) = -2j \frac{(1 + \Gamma_{iris})e^{-jk_{10}L}}{1 + \Gamma_{iris}e^{-2jk_{10}CL}} \sin[k_{10}(z - CL)]. \quad (6.33)$$

This expression is the same as we obtained from the multiple reflections method (Eq. (4.13)) except for the factor $\sin(m\pi x/a)$.

6.4 The Equivalent Circuit for the Microwave Heating System

By inserting the equivalent circuit of the rod into Fig. 6.5, the equivalent circuit for the microwave heating system is obtained and illustrated in Fig. 6.6.

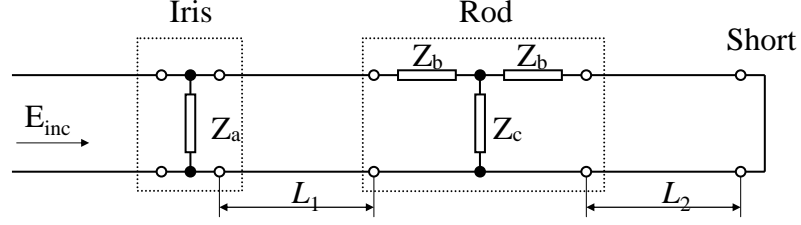


Figure 6.6: The equivalent circuit for the microwave heating system. In the model, the incident electric field is assumed to be a constant during the heating process.

In Fig. 6.6, Z_a is used to represent the iris, and the combination of Z_b and Z_c represent the rod. In the following discussions, normalized impedances are used for convenience.

In Fig. 6.7, four planes along the z direction are defined. From circuit theory, the input impedances viewed from these planes are

$$z_4 = j \tan(k_{10}L_2), \quad (6.34)$$

$$z_3 = z_b + \frac{z_c(z_b + z_4)}{z_c + z_b + z_4}, \quad (6.35)$$

$$z_2 = \frac{z_3 + j \tan(k_{10}L_1)}{1 + j z_3 \tan(k_{10}L_1)}, \quad (6.36)$$

and

$$z_1 = \frac{z_a z_2}{z_a + z_2}. \quad (6.37)$$

For a wave with unity amplitude striking the heating system from the left, the

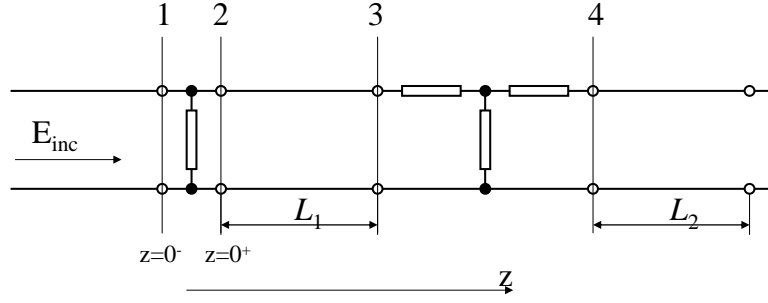


Figure 6.7: Four planes are defined in the equivalent circuit model. In the model, the incident electric field is assumed to be a constant during the heating process.

amplitude of the reflected wave is calculated through the total reflection coefficient Γ_1 as

$$V_1^- = \Gamma_1 V_1^+ = \Gamma_1 = \frac{z_1 - 1}{z_1 + 1}, \quad (6.38)$$

thus the total voltage and the total current at plane 1 are

$$V_1 = 1 + V_1^- = 1 + \Gamma_1, \quad (6.39)$$

and

$$I_1 = 1 - I_1^- = 1 - \Gamma_1. \quad (6.40)$$

At plane 2, the voltage and current are

$$V_2 = V_1 = 1 + \Gamma_1, \quad (6.41)$$

and

$$I_2 = I_1 - \frac{V_1}{z_a} = (1 - \Gamma_1) - \frac{1 + \Gamma_1}{z_a}. \quad (6.42)$$

The voltage and current along the transmission line between plane 2 and plane 3 are calculated from Eq. (6.12) and Eq. (6.13):

$$V(z) = \cos(k_{10}z)V_2 - j \sin(k_{10}z)I_2, \quad (6.43)$$

$$I(z) = -j \sin(k_{10}z)V_2 + \cos(k_{10}z)I_2. \quad (6.44)$$

By putting $z = L_1$ into the above equations, the voltage and current at plane 3 are

$$V_3 = \cos(k_{10}L_1)V_2 - j \sin(k_{10}L_1)I_2, \quad (6.45)$$

and

$$I_3 = -j \sin(k_{10}L_1)V_2 + \cos(k_{10}L_1)I_2. \quad (6.46)$$

At plane 4, the voltage and current computed from circuit theory are

$$V_4 = \left(1 + \frac{z_b}{z_c}\right)V_3 - \left(2z_b + \frac{z_b^2}{z_c}\right)I_3, \quad (6.47)$$

and

$$I_4 = -\frac{1}{z_c}V_3 + \left(1 + \frac{z_b}{z_c}\right)I_3. \quad (6.48)$$

The voltage and current between plane 4 and short plane are calculated from Eq. (6.12) and Eq. (6.13):

$$V(z) = \cos(k_{10}z)V_4 - j \sin(k_{10}z)I_4, \quad (6.49)$$

$$I(z) = -j \sin(k_{10}z)V_4 + \cos(k_{10}z)I_4. \quad (6.50)$$

In our heating system, L_1 , the distance between the iris plane and the heated rod, is fixed, thus the voltage and current in the waveguide are functions of z_a, z_b, z_c , and L_2 . These parameters can be obtained from the field analysis, which will be discussed in the next chapter.

Chapter 7

Computation of the Electric Field in the Cavity

In this chapter, methods for determining the two parameters in the equivalent circuits are discussed. In Section 7.1, the reflection coefficient of the iris is computed by mode matching and moment methods, which were developed by Terril^[75]. The results are compared with those obtained from the finite element method. In Section 7.2, we use orthogonal expansion method to calculate the electric field inside the rod. This method can provide accurate results. To deal with some difficulties encountered in the calculation when the properties of the rod vary along the rod, we develop an approximate method based on the current sources. This is an improvement of the method developed by Terril^[75].

7.1 Iris Problem

An iris, as illustrated in Fig. 7.1, is used to couple the fields in the waveguide and the cavity. This introduces an iris-type discontinuity in the microwave heating network. As discussed in the previous chapter, the most important quantity we are concerned about is Γ_{iris} , the reflection coefficient of the TE_{10} mode. To determine Γ_{iris} , we must find the solution of Maxwell's equations to satisfy the required boundary conditions. These boundary conditions include:

- Perfect electric conductor (PEC) conditions on the waveguide walls
- PEC condition on the iris

Additional boundary conditions must be added when specific solution methods are selected. For example, if the finite element method (FEM) is used, the matching boundary conditions must be applied at the inlet and outlet boundaries.

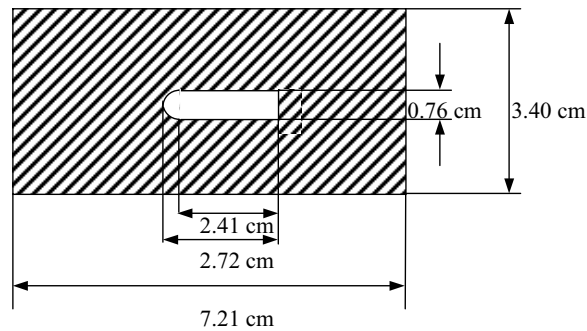


Figure 7.1: The iris used in the experiment

The method to solve this type of problem can be dated back to the 1940s. At that time, computers were not available so that some ingenious methods were developed by some scientists, among whom J. Schwinger played a dominant role^[64]. They used a transformation to overcome the most difficult part of the problem. Unfortunately, their methods can be used only in some specific cases, as illustrated in Figs. 7.2 and 7.3. In these cases, Maxwell's equations can be simplified to be scalar equations.



Figure 7.2: Capacitive Iris

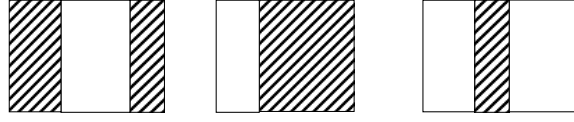


Figure 7.3: Inductive Iris

If the shape of the iris becomes complex, Schwinger's transformation cannot be found. In the 1960s, as a result of the availability of the computer, mode-matching techniques were used in the computation of waveguide discontinuities^[88]. These techniques are ideal to deal with the junction between two different waveguides. By expanding the transverse fields in terms of the waveguide modes, the scattering matrix can be obtained. However, these techniques cannot be directly applied to the iris-type discontinuities due to the zero thickness of the iris^[49]. Instead of expressing the fields in the aperture in terms of the waveguide modes, other series of orthogonal functions are used for the transverse electric and magnetic field. This idea is the same as that behind Schwinger's transformation and the procedure of this method is the same as that of the moment methods. Moment methods, as a general procedure to convert the analytical formulation into a numerical formulation in the form of a matrix equation, have been used in almost all computation fields. The applications of the moment methods in electromagnetic field problems can be found in several books^[33, 87] and overview papers^[32, 55]. Moment methods can handle more problems than the transformation method can. For example, a double iris, whose dimension is an exact rectangle as illustrated in Fig. 7.4, can be solved by moment methods.

However, since the methods are of global analysis, they still require the boundary of the iris to be regular.

As the iris shape becomes more complex, such as the iris used in our heating system, the FEM has to be used. Indeed, the FEM is also a kind of moment methods in which the solution region is divided into small elements.

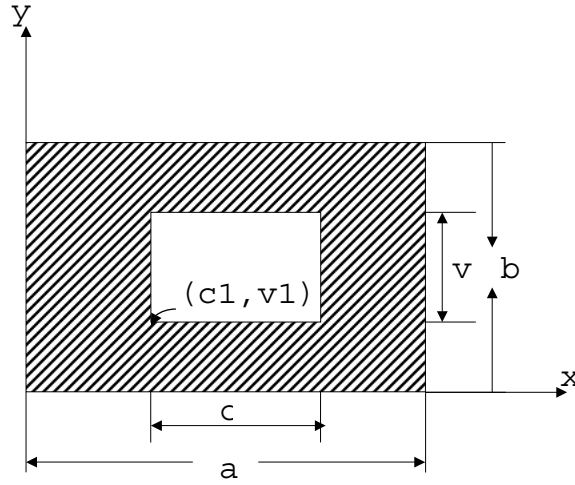


Figure 7.4: Double Step Iris

In the following, we will derive the integral equation first,¹ then briefly discuss the moment methods through an example. By the use of the moment methods, the solution of the double step iris is obtained. This solution serves as a criterion to determine the appropriate size of elements when using FEM. Finally, FEM is used to compute the reflection coefficient of the iris used in our experiments.

7.1.1 Integral equation

The electromagnetic fields inside a waveguide are constructed of the TE and TM modes. Every mode is an eigenfunction of Maxwell's equations under specific boundary conditions. For a rectangular waveguide, these modes can be obtained by separation of variables. The solution procedure can be found in any book on electromagnetic waves^[18, 31, 2]. In this dissertation, we use the results directly.

¹The derivation of the integral equation, the selection of the basis and weighting functions follow Terril's work^[75]. However, since we did not use the concepts of magnetic currents, the integral equations and the weighting functions are different from Terril's.

Modes

TE modes

First, we define the following orthonormal mode functions for a TE_{mn} mode:

$$\begin{aligned} \vec{e}_{m,n}^h &= e_{m,n}^{h,x} \hat{x} + e_{m,n}^{h,y} \hat{y} = \alpha_{m,n}^h \left[-\frac{n\pi}{b} \cos\left(\frac{m\pi x}{a}\right) \sin\left(\frac{n\pi y}{b}\right) \hat{x} \right. \\ &\quad \left. + \frac{m\pi}{a} \sin\left(\frac{m\pi x}{a}\right) \cos\left(\frac{n\pi y}{b}\right) \hat{y} \right], \end{aligned} \quad (7.1)$$

and

$$\begin{aligned} \vec{h}_{m,n}^h &= h_{m,n}^{h,x} \hat{x} + h_{m,n}^{h,y} \hat{y} = \frac{\alpha_{m,n}^h}{Z_{m,n}^h} \left[\frac{m\pi}{a} \sin\left(\frac{m\pi x}{a}\right) \cos\left(\frac{n\pi y}{b}\right) \hat{x} \right. \\ &\quad \left. + \frac{n\pi}{b} \cos\left(\frac{m\pi x}{a}\right) \sin\left(\frac{n\pi y}{b}\right) \hat{y} \right], \end{aligned} \quad (7.2)$$

where

$$Z_{m,n}^h = \frac{\omega\mu}{j\gamma_{m,n}}, \quad (7.3)$$

$$\alpha_{m,n}^h = \frac{2}{\sqrt{ab\epsilon_m^0 \epsilon_n^0 k_{c,mn}}}, \quad (7.4)$$

$$\epsilon_m^0 = \begin{cases} 2 & , \quad m = 0; \\ 1 & , \quad m \neq 0, \end{cases}$$

$$k_{c,mn}^2 = \left(\frac{m\pi}{a}\right)^2 + \left(\frac{n\pi}{b}\right)^2, \quad (7.5)$$

and

$$\gamma_{m,n} = \sqrt{\left(\frac{m\pi}{a}\right)^2 + \left(\frac{n\pi}{b}\right)^2 - \omega^2\mu\epsilon}. \quad (7.6)$$

The transverse electric and magnetic fields of a $\text{TE}_{m,n}$ wave traveling in the $+z$ direction are

$$\vec{E}_{m,n}^{h,Pos} = e^{-\gamma_{m,n}z} \vec{e}_{m,n}^h, \quad (7.7)$$

and

$$\vec{H}_{m,n}^{h,Pos} = e^{-\gamma_{m,n}z} \vec{h}_{m,n}^h, \quad (7.8)$$

while the transverse fields of a TE_{m,n} wave traveling in the $-z$ direction are

$$\vec{E}_{m,n}^{h,Neg} = e^{+\gamma_{m,n}z} \vec{e}_{m,n}^h, \quad (7.9)$$

and

$$\vec{H}_{m,n}^{h,Neg} = -e^{+\gamma_{m,n}z} \vec{h}_{m,n}^h. \quad (7.10)$$

TM modes

The orthonormal mode functions for a TM_{mn} mode are

$$\begin{aligned} \vec{e}_{m,n}^e &= e_{m,n}^{e,x} \hat{x} + e_{m,n}^{e,y} \hat{y} = \alpha_{m,n}^e \left[-\frac{m\pi}{a} \cos\left(\frac{m\pi x}{a}\right) \sin\left(\frac{n\pi y}{b}\right) \hat{x} \right. \\ &\quad \left. - \frac{n\pi}{b} \sin\left(\frac{m\pi x}{a}\right) \cos\left(\frac{n\pi y}{b}\right) \hat{y} \right], \end{aligned} \quad (7.11)$$

and

$$\begin{aligned} \vec{h}_{m,n}^e &= h_{m,n}^{e,x} \hat{x} + h_{m,n}^{e,y} \hat{y} = \frac{\alpha_{m,n}^e}{Z_{m,n}^e} \left[-\frac{n\pi}{b} \sin\left(\frac{m\pi x}{a}\right) \cos\left(\frac{n\pi y}{b}\right) \hat{x} \right. \\ &\quad \left. + \frac{m\pi}{a} \cos\left(\frac{m\pi x}{a}\right) \sin\left(\frac{n\pi y}{b}\right) \hat{y} \right], \end{aligned} \quad (7.12)$$

where

$$Z_{m,n}^e = \frac{j\gamma_{m,n}}{\omega\epsilon}, \quad (7.13)$$

and

$$\alpha_{m,n}^e = \frac{2}{\sqrt{ab}k_{c,mn}}. \quad (7.14)$$

The transverse electric and magnetic fields of a TM_{mn} wave traveling in the $+z$ directions are

$$\vec{E}_{m,n}^{e,Pos} = e^{-\gamma_{m,n}z} \vec{e}_{m,n}^e, \quad (7.15)$$

and

$$\vec{H}_{m,n}^{e,Pos} = e^{-\gamma_{m,n}z} \vec{h}_{m,n}^e, \quad (7.16)$$

while the fields of a TM_{mn} wave traveling in the $-z$ direction are

$$\vec{E}_{m,n}^{e,Neg} = e^{+\gamma_{m,n}z} \vec{e}_{m,n}^e, \quad (7.17)$$

and

$$\vec{H}_{m,n}^{e,Neg} = -e^{+\gamma_{m,n}z} \vec{h}_{m,n}^e. \quad (7.18)$$

Fields

Suppose there is a TE_{10} mode propagating in the $+z$ direction and an iris is located at the $z = 0$ plane. Due to the presence of the iris, higher order modes are excited. To the left of the iris, the fields are composed of a TE_{10} mode traveling in the $+z$ direction and other reflected TE and TM modes traveling in the $-z$ direction, thus the fields are expressed as

$$\vec{E}^A = \sum_{m,n} (A_{m,n}^h \vec{E}_{m,n}^{h,Neg} + A_{m,n}^e \vec{E}_{m,n}^{e,Neg}) + \vec{E}_{1,0}^{h,Pos}, \quad (7.19)$$

and

$$\vec{H}^A = \sum_{m,n} (A_{m,n}^h \vec{H}_{m,n}^{h,Neg} + A_{m,n}^e \vec{H}_{m,n}^{e,Neg}) + \vec{H}_{1,0}^{h,Pos}. \quad (7.20)$$

To the right of the iris, the fields are composed of transmitted waves traveling in the $+z$ direction if no other obstacles exist downstream, thus the fields are expressed as

$$\vec{E}^B = \sum_{m,n} (B_{m,n}^h \vec{E}_{m,n}^{h,Pos} + B_{m,n}^e \vec{E}_{m,n}^{e,Pos}) + \vec{E}_{1,0}^{h,Pos}, \quad (7.21)$$

and

$$\vec{H}^B = \sum_{m,n} (B_{m,n}^h \vec{H}_{m,n}^{h,Pos} + B_{m,n}^e \vec{H}_{m,n}^{e,Pos}) + \vec{H}_{1,0}^{h,Pos}. \quad (7.22)$$

Boundary conditions and the integral equation

The only physical boundary condition on the iris plane is the PEC condition, which requires the tangential electric field to be zero on the iris. On the aperture, no

boundary exists, thus the electric and magnetic fields must be the same. Overall, at the $z = 0$ plane, the electric fields should be the same everywhere, thus $A_{m,n}^h = B_{m,n}^h$ and $A_{m,n}^e = B_{m,n}^e$.

The electric field at the $z = 0$ plane is assumed to be

$$\vec{E}^0 = \begin{cases} \vec{E} & , \text{ on the aperture;} \\ 0 & , \text{ on the iris,} \end{cases}$$

where \vec{E} is a unknown vector function. Inserting Eq. (7.19) into the above expression, we obtain

$$\sum_{m,n} (A_{m,n}^h \vec{e}_{m,n}^h + A_{m,n}^e \vec{e}_{m,n}^e) + \vec{e}_{1,0}^h = \vec{E} \quad \text{on the aperture.} \quad (7.23)$$

Due to the orthogonality between different modes, the coefficients of the mode can be computed as

$$A_{m,n}^h = \iint_{aper} \vec{E} \cdot \vec{e}_{m,n}^h ds - \delta_m^1 \delta_n^0, \quad (7.24)$$

$$A_{m,n}^e = \iint_{aper} \vec{E} \cdot \vec{e}_{m,n}^e ds. \quad (7.25)$$

From the condition that the tangential magnetic field must be the same on the aperture, we obtain

$$\vec{H}^A = \vec{H}^B \quad \text{on the aperture.} \quad (7.26)$$

By the use of Eqs. (7.20) and (7.22), we obtain

$$\sum_{m,n} (A_{m,n}^h \vec{h}_{m,n}^h + A_{m,n}^e \vec{h}_{m,n}^e) = 0. \quad (7.27)$$

This equation gives us some useful information about the tangential magnetic field on the aperture. If we put this result into Eq. (7.20), it is obvious that the tangential magnetic field on the aperture is just the magnetic field of the TE₁₀ mode.

By substituting the expressions of $A_{m,n}^h$ and $A_{m,n}^e$ into the above equation and after some simplifications, we obtain

$$\sum_{m,n} \left[\iint_{aper} \vec{E}(r') \cdot \vec{e}_{m,n}^h(r') \vec{h}_{m,n}^h(r) ds + \iint_{aper} \vec{E}(r') \cdot \vec{e}_{m,n}^e(r') \vec{h}_{m,n}^e(r) ds \right] = \vec{h}_{1,0}^h(r). \quad (7.28)$$

If we let

$$\vec{G}(r', r) = \sum_{m,n} \left[\vec{e}_{m,n}^h(r') \vec{h}_{m,n}^h(r) + \vec{e}_{m,n}^e(r') \vec{h}_{m,n}^e(r) \right], \quad (7.29)$$

we obtain the integral equation

$$\iint_{aper} \vec{E}(r') \cdot \vec{G}(r', r) ds' = \vec{h}_{1,0}^h(r) \quad \text{on the aperture.} \quad (7.30)$$

This is the integral equation we need to solve. Before we use moment methods to solve this problem, we use a simpler problem to reveal the difficulty inside this integral equation and briefly discuss the moment methods.

7.1.2 Moment methods

We consider an inductive iris with zero thickness located at a homogeneous waveguide. The dimension of the iris is illustrated in Fig. 7.5. The incident field, a TE_{10} mode with unity amplitude, will set up the reflected and transmitted higher order modes. Since the fields of the TE_{10} mode are independent of y and the inductive iris does not introduce any y -related boundary condition, then all field components are independent of y . Moreover, if we note that x and z components of the electric field are zero at $y = 0$ and $y = b$, we conclude that only the y component of the electric field exists. From the mode function, this means that only the TE_{m0} mode can be excited by the iris. Therefore, the expression of $\vec{G}(r', r)$ and $\vec{E}(r')$ are simplified to be

$$\vec{G}(r', r) = \sum_m \vec{e}_{m,0}^h(r') \vec{h}_{m,0}^h(r) = \sum_m \frac{2j\gamma_{m,0}}{ab\omega\mu} \sin\left(\frac{m\pi x'}{a}\right) \sin\left(\frac{m\pi x}{a}\right) \hat{y}' \hat{x}, \quad (7.31)$$

and

$$\vec{E}(r') = E_y(x')\hat{y}'. \quad (7.32)$$

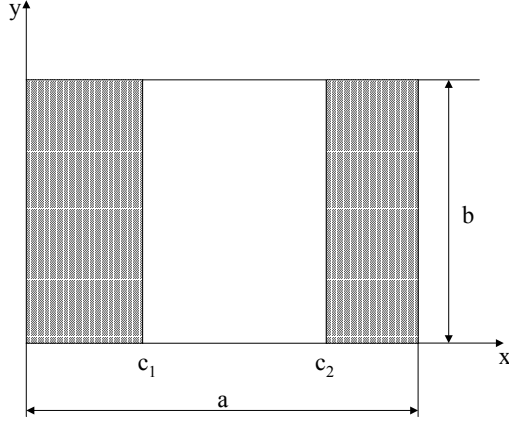


Figure 7.5: Inductive Iris - An Example

By putting the above expressions into Eq. (7.30), we obtain

$$\sum_{m=1}^{\infty} \frac{\gamma_{m,0}}{\gamma_{1,0}} \sin\left(\frac{m\pi x}{a}\right) \int_{c_1}^{c_2} E_y(x') \sin\left(\frac{m\pi x'}{a}\right) dx' = \sqrt{\frac{a}{2b}} \sin\left(\frac{\pi x}{a}\right) \quad \text{on the aperture.} \quad (7.33)$$

The difficulty of this integral equation is that both the range of the integration and the range that the integral equation must hold are not the full guide width, over which the modes are orthogonal to each other. If such difficulty does not exist, the integral equation is only a trivial problem.

To illustrate the difficulty more clearly, we propose a method to solve it. First, we truncate the infinite summation in Eq. (7.33) to the first M terms, that is

$$\sum_{m=1}^M \frac{\gamma_{m,0}}{\gamma_{1,0}} \sin\left(\frac{m\pi x}{a}\right) \int_{c_1}^{c_2} E_y(x') \sin\left(\frac{m\pi x'}{a}\right) dx' = \sqrt{\frac{a}{2b}} \sin\left(\frac{\pi x}{a}\right) \quad \text{on aperture.} \quad (7.34)$$

Since the set of $\sin(m\pi x'/a)$, $m = 1, 2, \dots, M$ are linearly independent over the region of (c_1, c_2) , we can construct $E_y(x')$ as a linear combination of $\sin(m\pi x'/a)$,

$$E_y(x') = \sum_{m=1}^M c_m \sin\left(\frac{m\pi x'}{a}\right). \quad (7.35)$$

By properly selecting c_m we can let $E_y(x')$ be orthogonal to $\sin(m\pi x'/a)$, $m = 2, \dots, M$ and

$$\int_{c_1}^{c_2} E_y(x') \sin \frac{\pi x'}{a} dx' = \sqrt{\frac{a}{2b}}. \quad (7.36)$$

Apparently, this $E_y(x')$ is a solution to Eq. (7.34), but is not a solution to our original problem. This can be seen if we notice that $A_{m,0}^h = 0$, $m = 2, 3 \dots, M$ from Eq. (7.24), so only the TE_{10} mode is excited by the iris. In other words, the iris has been removed from the waveguide by this solution. We can also view this solution from an error estimation point of view. If we add one more term in the summation, the error will be

$$\begin{aligned} error &= \frac{\gamma_{M+1,0}}{\gamma_{1,0}} \sin \frac{(M+1)\pi x}{a} \int_{c_1}^{c_2} E_y(x') \sin \frac{(M+1)\pi x'}{a} dx' \\ &= \frac{\gamma_{M+1,0}}{\gamma_{1,0}} \sin \frac{(M+1)\pi x}{a} \sum_{m=1}^M c_m \langle \sin \frac{m\pi x'}{a}, \sin \frac{(M+1)\pi x'}{a} \rangle. \end{aligned} \quad (7.37)$$

Here we use $\langle \rangle$ to represent the integration. We cannot guarantee that the error is small. Indeed, in a numerical experiment, c_m increases rapidly with increasing m . This is analogous to the use of $1, x, x^2 \dots$ to approximate a known function.

To obtain correct results, we must choose an orthogonal set to approximate $E_y(x')$. For example, let

$$E_y(x') = \sum_{p=1}^{\infty} c_p \phi_p(x'), \quad (7.38)$$

where $\phi_p(x)$, $p = 1, 2, \dots, \infty$ is a set of functions which are orthonormal to each other over the region (c_1, c_2) and c_p is the corresponding Fourier coefficient. In moment methods, $\phi_p(x)$ is called a *basis function*. Since the integral equation is a linear system, we can examine the response of $\phi_p(x')$ individually. From Eq. (7.33), the response of $\phi_p(x')$ is

$$\sum_{m=1}^{\infty} \frac{\gamma_{m,0}}{\gamma_{1,0}} \sin \left(\frac{m\pi x}{a} \right) \int_{c_1}^{c_2} \phi_p(x') \sin \left(\frac{m\pi x'}{a} \right) dx'. \quad (7.39)$$

Because the response is composed of $\sin(m\pi x/a)$, $m = 1, 2, 3 \dots, \infty$, which are not orthogonal to each other, then it is necessary to expand $\sin(m\pi x/a)$ in terms of another set of orthonormal functions $\varphi_q(x)$, $q = 1, 2, \dots, \infty$, which are called *weighting functions*. Let

$$\sin\left(\frac{m\pi x}{a}\right) = \sum_{q=1}^{\infty} a_{qm} \varphi_q(x), \quad (7.40)$$

thus the response of $\phi_p(x')$ is

$$\sum_{q=1}^{\infty} \left(\sum_{m=1}^{\infty} \frac{\gamma_{m,0}}{\gamma_{1,0}} a_{qm} b_{mp} \right) \varphi_q(x), \quad (7.41)$$

where

$$b_{mp} = \int_{c_1}^{c_2} \phi_p(x') \sin\left(\frac{m\pi x'}{a}\right) dx'. \quad (7.42)$$

By substituting Eqs. (7.38) and (7.41) into Eq. (7.33) and comparing the coefficients of $\varphi_q(x)$, we obtain

$$\sum_{p=1}^{\infty} \left(\sum_{m=1}^{\infty} \frac{\gamma_{m,0}}{\gamma_{1,0}} a_{qm} b_{mp} \right) c_p = \sqrt{\frac{a}{2b}} a_{1q} \quad q = 1, 2, 3, \dots, \infty. \quad (7.43)$$

This is the matrix equation to determine c_p , then E_y , and finally $A_{m,n}$. To obtain a numerical solution, the three infinite series summations must be truncated. We use M , P , and Q to denote the terms to be selected in the summations. Our objective is to determine the reflection coefficient of the TE₁₀ mode. From Eq. (7.24),

$$A_{1,0}^h = \iint_{aper} \vec{E} \cdot \vec{e}_{1,0}^h ds - 1 = \alpha_{1,0}^h \frac{\pi}{a} \sum_{p=1}^P c_p b_{1p} - 1. \quad (7.44)$$

Before the solution is obtained, c_p is unknown. However, we expect that c_p decreases with increasing p . Otherwise, this method fails. As a rough approximation², let $c_p \sim 1/p$. b_{1p} is the projection of $\sin(\pi x/a)$ on $\phi_p(x)$. A natural choice of $\phi_p(x)$ is $\sin[p\pi(x - c_1)/(c_2 - c_1)]$, which is the mode of a waveguide with width $c_2 - c_1$. It can be shown that $b_{1p} \sim 1/p$. Therefore, $A_{1,0}^h$ converges rapidly. This means that

²Normally the coefficients of the orthogonal expansion decay very fast. Some discussions can be found in reference [10].

if we are only concerned about the reflection coefficient of the TE_{10} mode, P can be set to be a relative small number. From Eq. (7.43), to obtain a unique solution, Q should be selected to be equal to P .

The selection of M is an interesting issue, which induces the relative convergence phenomenon. From Eq. (7.43), M must be large enough so that the truncations will not affect the accuracy of the matrix element calculation. In other words, the truncated terms must be small compared with the remaining terms. Every term in those summations consist of the interactions between $\phi_p(x)$, $\varphi_p(x)$ and $\sin(m\pi x/a)$. As a general rule, the interactions between two waves is strengthened when the wavenumber of one wave approaches the wavenumber of another. If $\phi_p(x)$ is selected to be $\sin[p\pi(x - c_1)/(c_2 - c_1)]$, the strongest interaction occurs when $m/a = p/(c_2 - c_1)$, thus M must be larger than $pa/(c_2 - c_1)$. A detailed discussion can be found in a paper by Lee *et al.*^[44]

The selection of an appropriate set of basis and weighting functions is important when using moment methods; sometimes it is also difficult. In this example, the selection of $\sin[p\pi(x - c_1)/(c_2 - c_1)]$ is obvious because this set of functions satisfies the boundary conditions and has simple form. However, for vector problems, the selection is not an easy task anymore. The behaviors of both E_x and E_y are irregular at the boundary of the aperture. For example, E_y is zero at the x direction boundaries but it approaches infinity at the y direction boundaries³. Some special functions satisfying such conditions have been used by researchers^[54, 90]. By the use of those special functions, the terms of the basis function can be selected to be small, but the calculation process could be very lengthy. More importantly, in some cases, the orthogonality cannot be retained.

Compared with FEM or finite difference method, moment methods can produce very accurate results. However, if the geometry of the object becomes complex, the use of moment methods is highly limited. In these cases, FEM or finite difference method is necessary. In the next section, we will apply moment methods to the double step iris problem. The results are compared with those obtained from FEM,

³Such behaviors are called edge conditions, see reference [7].

then FEM is applied to obtain equivalent circuit of the iris used in our microwave heating system.

7.1.3 Solutions

Mode matching method solutions

First, we apply moment methods to solve the double step iris problem. The unknown electric field on the aperture are expressed in terms of basis functions $\phi_{p,q}^x$ and $\phi_{p,q}^y$ as

$$\vec{E}(x, y) = \sum_{p,q} [a_{p,q}^x \phi_{p,q}^x(r) \hat{x} + a_{p,q}^y \phi_{p,q}^y(r) \hat{y}], \quad (7.45)$$

where $a_{p,q}^x$ and $a_{p,q}^y$ are unknown coefficients. By substituting the above expression into Eq. (7.30), we obtain

$$\sum_{p,q} a_{p,q}^x \iint_{ap} \phi_{p,q}^x(r) \hat{x} \cdot \bar{G}(r', r) ds + \sum_{p,q} a_{p,q}^y \iint_{ap} \phi_{p,q}^y(r) \hat{y} \cdot \bar{G}(r', r) ds = \vec{h}_{1,0}^h(r). \quad (7.46)$$

The weighting functions are selected to have the forms

$$\vec{\varphi}_{s,t}^x = \varphi_{s,t}^x(r) \hat{x}, \quad (7.47)$$

$$\vec{\varphi}_{s,t}^y = \varphi_{s,t}^y(r) \hat{y}. \quad (7.48)$$

By applying the weighting functions $\vec{\varphi}_{s,t}^x$ and $\vec{\varphi}_{s,t}^y$ to Eq. (7.46), we obtain

$$\begin{aligned} \iint_{ap} \vec{h}_{1,0}^h(r) \cdot \varphi_{s,t}^x(r) \hat{x} ds &= \sum_{p,q} a_{p,q}^x \iint_{ap} \iint_{ap} \phi_{p,q}^x(r') \hat{x} \cdot \bar{G}(r', r) \cdot \varphi_{s,t}^x(r) \hat{x} ds' ds \\ &+ \sum_{p,q} a_{p,q}^y \iint_{ap} \iint_{ap} \phi_{p,q}^y(r') \hat{y} \cdot \bar{G}(r', r) \cdot \varphi_{s,t}^x(r) \hat{x} ds' ds, \end{aligned} \quad (7.49)$$

and

$$\begin{aligned} \iint_{ap} \vec{h}_{1,0}^h(r) \cdot \varphi_{s,t}^y(r) \hat{y} ds &= \sum_{p,q} a_{p,q}^x \iint_{ap} \iint_{ap} \phi_{p,q}^x(r') \hat{x} \cdot \bar{G}(r', r) \cdot \varphi_{s,t}^y(r) \hat{y} ds' ds \\ &+ \sum_{p,q} a_{p,q}^y \iint_{ap} \iint_{ap} \phi_{p,q}^y(r') \hat{y} \cdot \bar{G}(r', r) \cdot \varphi_{s,t}^y(r) \hat{y} ds' ds. \end{aligned} \quad (7.50)$$

The above two equations construct the matrix equation.

The basis functions are selected to be

$$\phi_{p,q}^x(x, y) = \cos\left(\frac{p\pi(x - c1)}{c}\right) \sin\left(\frac{q\pi(y - v1)}{v}\right), \quad (7.51)$$

and

$$\phi_{p,q}^y(x, y) = \sin\left(\frac{p\pi(x - c1)}{c}\right) \cos\left(\frac{q\pi(y - v1)}{v}\right), \quad (7.52)$$

where $(p, q) = (1, 2, 3, \dots, P) \times (0, 1, 2, \dots, Q)$.

The weighting functions used in the calculations are

$$\varphi_{s,t}^x(x, y) = \sin\left(\frac{s\pi(x - c1)}{c}\right) \cos\left(\frac{t\pi(y - v1)}{v}\right), \quad (7.53)$$

and

$$\varphi_{s,t}^y(x, y) = \cos\left(\frac{s\pi(x - c1)}{c}\right) \sin\left(\frac{t\pi(y - v1)}{v}\right), \quad (7.54)$$

where $(s, t) = (0, 1, 2, \dots, S) \times (1, 2, 3, \dots, T)$.

The detailed description of the solution procedure can be found in Terril's thesis^[75].

Fig. 7.6 shows the computed results. During the calculations, we set $P = Q = S = T$ and $M = N$, where M and N are the highest mode numbers used to compute $\overline{\overline{G}}(r', r)$ in Eq. (7.29). The symbol x_a is the normalized reactance of the iris, which is related to the normalized impedance z_a through $jx_a = z_a$.

It can be seen from Fig. 7.6 that when $M = 100$ and $P = 10$, the normalized reactance has converged to $x_a = 0.061$. Thus the normalized impedance z_a is $j0.061$ and the corresponding Γ_{iris} is $-0.985 + j0.121$. We will use these numbers as the exact values to verify the FEM results.

FEM solutions

Table 7.1 shows the results from the FEM. All results are calculated by the software FEMLAB. In the table, L, N1, N2, and Max are the length of the waveguide in the computation region, the number of nodes, the number of elements, and the maximum

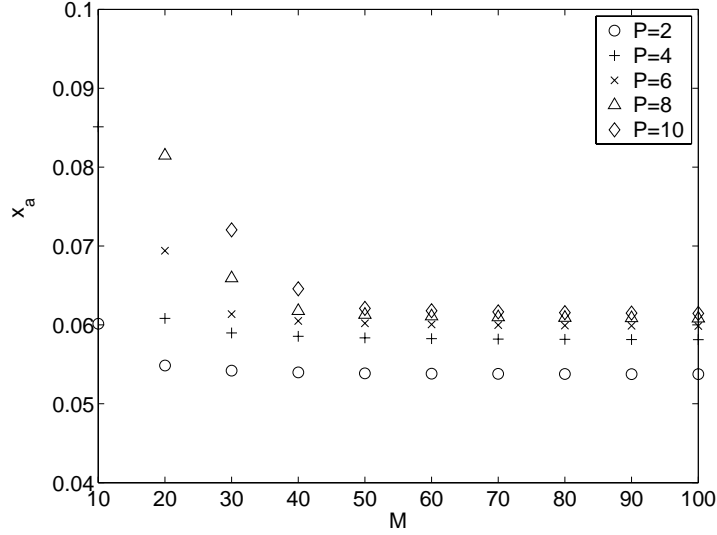


Figure 7.6: The reactance of the double step iris

size of the element on the aperture. All boundary conditions are set to be PECs except that the inlet and outlet boundary conditions are matching boundary conditions. A matching boundary is an imaginary boundary where no physical boundary exists. This concept is the same as the non-reflecting boundary used in computational fluid mechanics. On the inlet boundary, we specify the incident field to be the TE_{10} mode with unity amplitude.

The results obtained from the FEM are discrete field values. To obtain the reflection coefficient of the TE_{10} mode, an integration is necessary, that is

$$V_T = \frac{2}{ab} \int_S E_{y0} \sin\left(\frac{\pi x}{a}\right) ds, \quad (7.55)$$

where S represents the transverse area of the waveguide and E_{y0} is the y -component of the electric field at the $z = 0$ plane, which is the inlet boundary. V_T can be thought of as the total voltage or the amplitude of the TE_{10} mode. Since the incident field has been set to be the TE_{10} mode with unity amplitude, the amplitude of the reflected wave is $V_T - 1$, thus the reflection coefficient at the $z = 0$ plane is $V_T - 1$. Since the iris is located at the $z = L/2$ plane, the reflection coefficient of the TE_{10} mode is

$$\Gamma_{iris} = (V_T - 1)e^{jk_{10}L}, \quad (7.56)$$

and the normalized impedance is

$$z_a = -\frac{1 + \Gamma_{iris}}{2\Gamma_{iris}}. \quad (7.57)$$

When using the FEM, element shape and size are crucial to the success of computation. In our problem, there are two factors affecting element shape and size. First, since the aperture is small, especially its height, the element size must be set small to get reasonable results. However, the size of the elements that are not on the aperture are not necessarily small. Actually, the sizes of those elements should be as large as possible. Otherwise, the total number of elements will be too large. Therefore, we should use normal size elements in the whole region except limiting the maximum size of the element on the aperture. In Cases (2), (4), and (5), the size of the element on the aperture is limited by a fixed number. Secondly, to decrease the number of elements, the length of the waveguide in the computation region should be set as short as possible. However, this length cannot be set too small. To obtain better results, half of this length should be approximately equal to the height of the aperture.

Table 7.1: Computation results for a double step iris by FEM

Case	L (cm)	N1	N2	Max (cm)	Γ_{iris}	z_a
1	5	2363	11485	not controlled	-0.9929 + j 0.1011	-0.0016 + j0.0508
2	5	3450	17042	0.3	-0.9912 + j0.1104	-0.0017 + j 0.0555
3	1	1118	4666	not controlled	-0.9672 + 0.0940i	0.0121 + j0.0498
4	1	2311	10501	0.3	-0.9611 + 0.1143i	0.0130 + j 0.0610
5	1	4589	22468	0.2	-0.9596 + 0.1057i	0.0148 + j0.0567
6	0.5	3703	16263	not controlled	-0.9083 + j0.1238	0.0404 + j 0.0737

Based on the results provided in Table 7.1, we use the setting of Case (4) to compute the iris used in our experiment. The geometry and the grid are illustrated in Figs. 7.7 and 7.8.

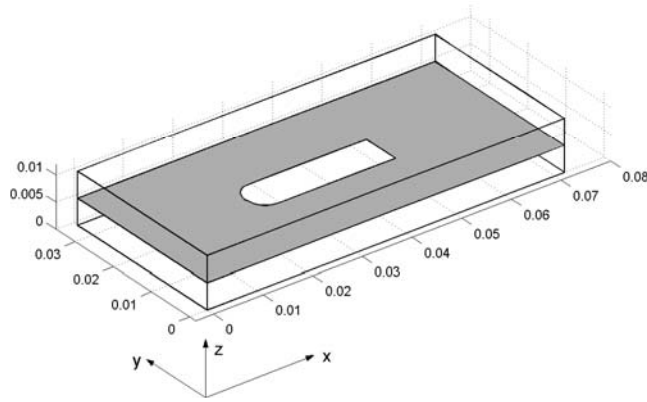


Figure 7.7: The geometry of the computation region

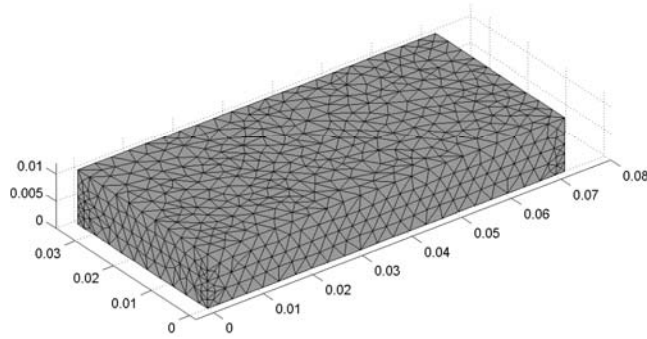


Figure 7.8: Meshing result

The calculated Γ_{iris} and z_a are $-0.969+j0.0892$ and $0.0118+j0.0472$. Notice that the impedance computed by the FEM is not a pure imaginary number. This contradicts the fact that the iris is lossless. Such error will not occur when using moment methods. In the following computation, we will use $z_a = j0.0472$.

7.2 Electric Field in the Rod

In this section, we will consider the fields scattered by the dielectric rod. The geometry of this problem consists of a box (waveguide section) and a cylinder (rod section). The eigenfunctions of Maxwell's equations in these two regions are known. The difficulty is how to match the solutions on the interface to satisfy the boundary conditions. The orthogonal expansion method^[28] (OEM) is believed to be reliable and accurate when

solving this type of discontinuity in the waveguide. It has been used to calculate the scattering properties of dielectric resonators^[47] and conducting posts^[91]. We will discuss this method in detail in Section 1. In the discussions, the dielectric properties of the rod are assumed to be a constant. This can reduce the problem to two dimensional. The box and cylinder become a rectangle and a circle. The equivalent circuit parameters obtained from this method are compared with those given in the *Waveguide Handbook*^[48]. Also, the electric field variation in the rod will be discussed.

When the rod is being heated, the temperature distribution along the rod is nonuniform, thus the temperature dependent dielectric properties are also nonuniform. Under these conditions, applying OEM becomes very lengthy, but such detailed information might be not necessary. Since the radius and the dielectric properties of the heated rod in our experiments are relatively small, we can assume the electric field along the r direction is a constant. This assumption has been used by Lewin^[45] and Terril^[75]. In section 2, we will discuss the solution procedure under this assumption. Also, we point out a pitfall when applying this assumption. In this section, all formulas will be derived by the use of the dyadic Green's function. After comparing the calculated results with those obtained from OEM, we propose an approximate method to handle the nonuniform properties along the rod. This is the main reason that we introduce the assumption that the electric field along the r direction is a constant.

7.2.1 Orthogonal expansion method

Algorithm^[28]

OEM is a kind of mode matching method. By expressing the fields in terms of the different eigenfunctions in the different regions and matching the fields on the interface, the scattering matrix can be obtained.

Suppose the incident wave is in the TE₁₀ mode, whose electric field has only a y component and is independent of y . If a rod is placed parallel to the electric field

and the dielectric property of the rod is constant, the rod does not introduce any new boundary condition along the y direction, thus y will not be an independent variable in this system. Also, the boundary conditions require E_x and E_z to vanish at $y = 0$ and $y = a$, so these two components of the electric field must be zero everywhere. This means that only E_y exists or only TE_{m0} modes can be excited by the rod.

The computation region is divided into four subregions, as illustrated in Fig. 7.9. Region I includes the dielectric rod. Region II is the interaction region, which is an imaginary circle with a radius $a/2$ and centered at $(a/2, 0)$, where a is the waveguide width. The other two regions are waveguide regions, called region WI and region WII, which are to the left and right of the interaction region.

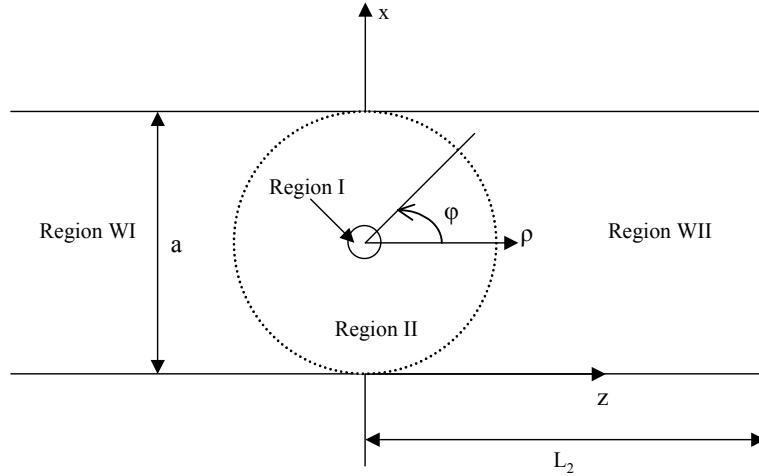


Figure 7.9: Geometry of the rod and waveguide

In region I and region II, the geometry is circular, thus the eigenfunctions are Bessel functions. In region I, the electric and magnetic fields are expressed as

$$E_{y,I} = a_0^i J_0(k_i \rho) \frac{1}{\sqrt{2\pi}} + \sum_{n=1}^{\infty} \left[a_n^{is} J_n(k_i \rho) \frac{\sin n\phi}{\sqrt{\pi}} + a_n^{ic} J_n(k_i \rho) \frac{\cos n\phi}{\sqrt{\pi}} \right], \quad (7.58)$$

and

$$H_{\phi,I} = -\frac{j}{\omega\mu} \frac{\partial E_y}{\partial \rho} = -\frac{jk_i}{\omega\mu} \left\{ a_0^i J_0'(k_i \rho) \frac{1}{\sqrt{2\pi}} + \sum_{n=1}^{\infty} \left[a_n^{is} J_n'(k_i \rho) \frac{\sin n\phi}{\sqrt{\pi}} + a_n^{ic} J_n'(k_i \rho) \frac{\cos n\phi}{\sqrt{\pi}} \right] \right\}, \quad (7.59)$$

where

$$k_i = \omega \sqrt{\varepsilon \mu}, \quad (7.60)$$

and ε is the dielectric constant of the rod. For convenience, the amplitudes of the eigenfunctions are written in vector form, that is

$$\vec{a}^i = \begin{bmatrix} a_0^i \\ a_1^{is} \\ a_2^{is} \\ \vdots \\ a_1^{ic} \\ a_2^{ic} \\ \vdots \end{bmatrix}. \quad (7.61)$$

In region II, the fields are expressed as

$$\begin{aligned} E_{y,\text{II}} = & a_0^J J_0(k\rho) \frac{1}{\sqrt{2\pi}} + a_0^Y Y_0(k\rho) \frac{1}{\sqrt{2\pi}} + \sum_{n=1}^{\infty} \left[a_n^{Js} J_n(k\rho) \frac{\sin n\phi}{\sqrt{\pi}} + a_n^{Jc} J_n(k\rho) \frac{\cos n\phi}{\sqrt{\pi}} \right. \\ & \left. + a_n^{Ys} Y_n(k\rho) \frac{\sin n\phi}{\sqrt{\pi}} + a_n^{Yc} Y_n(k\rho) \frac{\cos n\phi}{\sqrt{\pi}} \right], \end{aligned} \quad (7.62)$$

and

$$\begin{aligned} H_{\phi,\text{II}} = & -\frac{jk}{\omega\mu} \left\{ a_0^J J_0'(k\rho) \frac{1}{\sqrt{2\pi}} + a_0^Y Y_0'(k\rho) \frac{1}{\sqrt{2\pi}} + \sum_{n=1}^{\infty} \left[a_n^{Js} J_n'(k\rho) \frac{\sin n\phi}{\sqrt{\pi}} \right. \right. \\ & \left. \left. + a_n^{Jc} J_n'(k\rho) \frac{\cos n\phi}{\sqrt{\pi}} + a_n^{Ys} Y_n'(k\rho) \frac{\sin n\phi}{\sqrt{\pi}} + a_n^{Yc} Y_n'(k\rho) \frac{\cos n\phi}{\sqrt{\pi}} \right] \right\}, \end{aligned} \quad (7.63)$$

where

$$k = \omega \sqrt{\varepsilon_0 \mu}. \quad (7.64)$$

The amplitudes of the electric field eigenfunctions are written in vector form as

$$\vec{a}^J = \begin{bmatrix} a_0^J \\ a_1^{Js} \\ a_2^{Js} \\ \vdots \\ a_1^{Jc} \\ a_2^{Jc} \\ \vdots \end{bmatrix}, \text{ and } \vec{a}^Y = \begin{bmatrix} a_0^Y \\ a_1^{Ys} \\ a_2^{Ys} \\ \vdots \\ a_1^{Yc} \\ a_2^{Yc} \\ \vdots \end{bmatrix}. \quad (7.65)$$

In the waveguide regions, the electric fields are expressed as

$$E_{y,\text{WI}} = \sum_{m=1}^{\infty} \sin \frac{m\pi x}{a} [q_m e^{-jk_{z,m}z} + r_m e^{jk_{z,m}z}], \quad (7.66)$$

and

$$E_{y,\text{WII}} = \sum_{m=1}^{\infty} \sin \frac{m\pi x}{a} [t_m e^{-jk_{z,m}z} + s_m e^{jk_{z,m}z}], \quad (7.67)$$

where

$$k_{z,m} = \sqrt{\omega^2 \varepsilon_0 \mu - \left(\frac{m\pi}{a}\right)^2}. \quad (7.68)$$

For convenience, the waveguide modes are abbreviated as

$$\Phi_m^q(x, z) = \Phi_m^t(x, z) = \sin \frac{m\pi x}{a} e^{-jk_{z,m}z}, \quad (7.69)$$

and

$$\Phi_m^r(x, z) = \Phi_m^s(x, z) = \sin \frac{m\pi x}{a} e^{+jk_{z,m}z}. \quad (7.70)$$

Thus the fields in the waveguide regions are written as

$$E_{y,\text{WI}} = \sum_{m=1}^{\infty} [q_m \Phi_m^q(x, z) + r_m \Phi_m^r(x, z)], \quad (7.71)$$

$$E_{y,\text{WII}} = \sum_{m=1}^{\infty} [t_m \Phi_m^t(x, z) + s_m \Phi_m^s(x, z)]. \quad (7.72)$$

The continuity conditions require that the tangential electric and magnetic fields be equal at the interfaces. In this problem, two types of interfaces exist. The first is the interface between the dielectric rod and air, which is a physical interface. The other is an imaginary interface, which we call an interface because it divides the waveguide into regions with different eigenfunctions. The continuity conditions are used to determine the amplitudes of the modes.

The continuity conditions on the interface of the dielectric rod surface require

$$E_{y,I} = E_{y,II} \quad \text{at} \quad \rho = r, \quad (7.73)$$

and

$$H_{\phi,I} = H_{\phi,II} \quad \text{at} \quad \rho = r, \quad (7.74)$$

where r is the radius of the rod.

Substituting Eqs. (7.58) and (7.62) into Eq. (7.73), Eqs. (7.59) and (7.63) into Eq. (7.74), we obtain

$$\vec{a}^Y = \xi \cdot \vec{a}^J, \quad (7.75)$$

and

$$\vec{a}^i = \eta \cdot \vec{a}^J. \quad (7.76)$$

After some algebraic manipulations, we obtain

$$\xi = \begin{bmatrix} \xi_0 & 0 & 0 & \cdots & 0 \\ 0 & \xi_1 & 0 & \cdots & \vdots \\ 0 & 0 & \ddots & 0 & \vdots \\ \vdots & \vdots & 0 & \xi_n & 0 \\ 0 & \cdots & \cdots & 0 & \ddots \end{bmatrix}, \quad (7.77)$$

and

$$\eta = \begin{bmatrix} \eta_0 & 0 & 0 & \cdots & 0 \\ 0 & \eta_1 & 0 & \cdots & \vdots \\ 0 & 0 & \ddots & 0 & \vdots \\ \vdots & \vdots & 0 & \eta_m & 0 \\ 0 & \cdots & \cdots & 0 & \ddots \end{bmatrix}, \quad (7.78)$$

where

$$\xi_n = \frac{J'_n(kr)J_n(k_i r) - \sqrt{\frac{\epsilon}{\epsilon_0}}J_n(kr)J'_n(k_i r)}{\sqrt{\frac{\epsilon}{\epsilon_0}}Y_n(kr)J'_n(k_i r) - Y'_n(kr)J_n(k_i r)}, \quad n = 0, 1, 2, \dots, \quad (7.79)$$

and

$$\eta_n = \frac{J_n(kr) + \xi_n Y_n(kr)}{J_n(k_i r)}, \quad n = 0, 1, 2, \dots. \quad (7.80)$$

Notice that all properties of the rod are included in ξ and η . At this step, we rewrite the electric and magnetic fields in region II in a more concise form as

$$E_{y,\text{II}} = U_0(k\rho) \frac{1}{\sqrt{2\pi}} + \sum_{n=1}^{\infty} \left[U_n^s(k\rho) \frac{\sin n\phi}{\sqrt{\pi}} + U_n^c(k\rho) \frac{\cos n\phi}{\sqrt{\pi}} \right], \quad (7.81)$$

and

$$H_{\phi,\text{II}} = -\frac{jk}{\omega\mu} \left\{ I_0(k\rho) \frac{1}{\sqrt{2\pi}} + \sum_{n=1}^{\infty} \left[I_n^s(k\rho) \frac{\sin n\phi}{\sqrt{\pi}} + I_n^c(k\rho) \frac{\cos n\phi}{\sqrt{\pi}} \right] \right\}. \quad (7.82)$$

The functions $U_n^s(k\rho)$, $U_n^c(k\rho)$, $I_n^s(k\rho)$ and $I_n^c(k\rho)$ can be written in vector form as

$$\vec{U}(k\rho) = \begin{bmatrix} U_0(k\rho) \\ U_1^s(k\rho) \\ U_2^s(k\rho) \\ \vdots \\ U_1^c(k\rho) \\ U_2^c(k\rho) \\ \vdots \end{bmatrix}, \quad \vec{I}(k\rho) = \begin{bmatrix} I_0(k\rho) \\ I_1^s(k\rho) \\ I_2^s(k\rho) \\ \vdots \\ I_1^c(k\rho) \\ I_2^c(k\rho) \\ \vdots \end{bmatrix}. \quad (7.83)$$

By comparing Eqs. (7.81) and (7.82) with Eqs. (7.62) and (7.63), we obtain

$$\vec{U}(k\rho) = J(k\rho) \cdot \vec{a}^J + Y(k\rho) \cdot \vec{a}^Y, \quad (7.84)$$

and

$$\vec{I}(k\rho) = J'(k\rho) \cdot \vec{a}^J + Y'(k\rho) \cdot \vec{a}^Y, \quad (7.85)$$

where

$$J(k\rho) = \begin{bmatrix} J_0(k\rho) & 0 & \cdots & \cdots & \cdots & \cdots & 0 \\ 0 & J_1(k\rho) & 0 & \cdots & \cdots & \cdots & \vdots \\ \vdots & 0 & J_2(k\rho) & 0 & \cdots & \cdots & \vdots \\ \vdots & \vdots & 0 & \ddots & 0 & \vdots & \vdots \\ \vdots & \vdots & \vdots & 0 & J_1(k\rho) & 0 & \vdots \\ \vdots & \vdots & \vdots & \vdots & 0 & J_2(k\rho) & 0 \\ 0 & \cdots & \cdots & \cdots & \cdots & 0 & \ddots \end{bmatrix}, \quad (7.86)$$

and

$$Y(k\rho) = \begin{bmatrix} Y_0(k\rho) & 0 & \cdots & \cdots & \cdots & \cdots & 0 \\ 0 & Y_1(k\rho) & 0 & \cdots & \cdots & \cdots & \vdots \\ \vdots & 0 & Y_2(k\rho) & 0 & \cdots & \cdots & \vdots \\ \vdots & \vdots & 0 & \ddots & 0 & \vdots & \vdots \\ \vdots & \vdots & \vdots & 0 & Y_1(k\rho) & 0 & \vdots \\ \vdots & \vdots & \vdots & \vdots & 0 & Y_2(k\rho) & 0 \\ 0 & \cdots & \cdots & \cdots & \cdots & 0 & \ddots \end{bmatrix}. \quad (7.87)$$

By putting Eq. (7.75) into Eqs. (7.84) and (7.85), we obtain

$$\vec{U}(k\rho) = \{J(k\rho) + Y(k\rho) \cdot \xi\} \cdot \vec{a}^J, \quad (7.88)$$

and

$$\vec{I}(k\rho) = \{J'(k\rho) + Y'(k\rho) \cdot \xi\} \cdot \vec{a}^J. \quad (7.89)$$

From the above equations, we see that $\vec{U}(k\rho)$ relates to $\vec{I}(k\rho)$ through \vec{a}^J . After eliminating \vec{a}^J , we obtain

$$\vec{U}(k\rho) = Z(k\rho) \cdot \vec{I}(k\rho), \quad (7.90)$$

where

$$Z(k\rho) = \{J(k\rho) + Y(k\rho) \cdot \xi\} \cdot \{J'(k\rho) + Y'(k\rho) \cdot \xi\}^{-1}. \quad (7.91)$$

This equation gives the relation between electric and magnetic fields.

Now, we will match the fields on the imaginary interface. Before doing this, we transform the independent variables x and z used in the waveguide regions into cylindrical coordinates r and ρ , thus Eqs. (7.69) and (7.70) become

$$\Phi_m^q(\rho, \phi) = \Phi_m^t(\rho, \phi) = \sin\left(\frac{m\pi}{2} + \frac{m\pi\rho \sin\phi}{a}\right)e^{-jk_{zm}\rho \cos\phi}, \quad (7.92)$$

$$\Phi_m^r(\rho, \phi) = \Phi_m^s(\rho, \phi) = \sin\left(\frac{m\pi}{2} + \frac{m\pi\rho \sin\phi}{a}\right)e^{+jk_{zm}\rho \cos\phi}, \quad (7.93)$$

and the electric fields in region WI and WII become

$$E_{y,\text{WI}} = \sum_{m=1}^{\infty} [q_m \Phi_m^q(\rho, \phi) + r_m \Phi_m^r(\rho, \phi)], \quad (7.94)$$

and

$$E_{y,\text{WII}} = \sum_{m=1}^{\infty} [t_m \Phi_m^t(\rho, \phi) + s_m \Phi_m^s(\rho, \phi)]. \quad (7.95)$$

To write the magnetic fields in a concise form, we define

$$\Psi_m^i = \frac{\partial \Phi_m^i(\rho, \phi)}{\partial \rho}, \quad i = q, t, r, s, \quad (7.96)$$

thus the magnetic fields in the waveguide regions are

$$H_{\phi,\text{WI}} = -\frac{j}{\omega\mu} \frac{\partial E_y}{\partial \rho} = -\frac{j}{\omega\mu} \sum_{m=1}^{\infty} [q_m \Psi_m^q(\rho, \phi) + r_m \Psi_m^r(\rho, \phi)], \quad (7.97)$$

and

$$H_{\phi,\text{WII}} = -\frac{j}{\omega\mu} \frac{\partial E_y}{\partial \rho} = -\frac{j}{\omega\mu} \sum_{m=1}^{\infty} [t_m \Psi_m^t(\rho, \phi) + s_m \Psi_m^s(\rho, \phi)]. \quad (7.98)$$

The continuity condition of the electric field at the imaginary interface requires

$$E_{y,\text{II}}(\rho, \phi) = \begin{cases} E_{y,\text{WI}}(\rho, \phi) & , \quad \phi \in \left[\frac{\pi}{2}, \frac{3\pi}{2}\right]; \\ E_{y,\text{WII}}(\rho, \phi) & , \quad \phi \in \left[-\frac{\pi}{2}, \frac{\pi}{2}\right]. \end{cases} \quad (7.99)$$

By substituting Eqs. (7.81), (7.71) and (7.72) into the above equation and matching the fields at $\rho = a/2$, we obtain

$$\begin{aligned} & U_0(ka/2) \frac{1}{\sqrt{2\pi}} + \sum_{n=1}^{\infty} \left[U_n^s(ka/2) \frac{\sin n\phi}{\sqrt{\pi}} + U_n^c(ka/2) \frac{\cos n\phi}{\sqrt{\pi}} \right] \\ & = \begin{cases} \sum_{m=1}^{\infty} [q_m \Phi_m^q(a/2, \phi) + r_m \Phi_m^r(a/2, \phi)] & , \quad \phi \in \left[\frac{\pi}{2}, \frac{3\pi}{2}\right]; \\ \sum_{m=1}^{\infty} [t_m \Phi_m^t(a/2, \phi) + s_m \Phi_m^s(a/2, \phi)] & , \quad \phi \in \left[-\frac{\pi}{2}, \frac{\pi}{2}\right]. \end{cases} \end{aligned} \quad (7.100)$$

Now we can use the orthogonality property of $\sin n\phi$ and $\cos n\phi$ over the range of $[-\pi/2, 3\pi/2]$ to get an expression for $\vec{U}(ka/2)$. For brevity, we write $\sin n\phi$ and $\cos n\phi$ in vector form, that is

$$\vec{T}(\phi) = \frac{1}{\sqrt{\pi}} \begin{bmatrix} 1/\sqrt{2} \\ \sin \phi \\ \sin 2\phi \\ \vdots \\ \cos \phi \\ \cos 2\phi \\ \vdots \end{bmatrix}. \quad (7.101)$$

The integration of Eq. (7.100) with respect to ϕ over the range of $-\frac{\pi}{2}$ to $\frac{3\pi}{2}$ yields

$$\begin{aligned} \vec{U}(ka/2) &= \sum_{m=1}^{\infty} \left\{ q_m \int_{\pi/2}^{3\pi/2} \vec{T}(\phi) \Phi_m^q(a/2, \phi) d\phi + s_m \int_{-\pi/2}^{\pi/2} \vec{T}(\phi) \Phi_m^s(a/2, \phi) d\phi \right. \\ &\quad \left. + r_m \int_{\pi/2}^{3\pi/2} \vec{T}(\phi) \Phi_m^r(a/2, \phi) d\phi + t_m \int_{-\pi/2}^{\pi/2} \vec{T}(\phi) \Phi_m^t(a/2, \phi) d\phi \right\}. \end{aligned} \quad (7.102)$$

The same matching procedure can be applied to the continuity condition of H_ϕ . We obtain

$$\begin{aligned} \vec{I}(ka/2) &= \sum_{m=1}^{\infty} \left\{ q_m \int_{\pi/2}^{3\pi/2} \vec{T}(\phi) \Psi_m^q(a/2, \phi) d\phi + s_m \int_{-\pi/2}^{\pi/2} \vec{T}(\phi) \Psi_m^s(a/2, \phi) d\phi \right. \\ &\quad \left. + r_m \int_{\pi/2}^{3\pi/2} \vec{T}(\phi) \Psi_m^r(a/2, \phi) d\phi + t_m \int_{-\pi/2}^{\pi/2} \vec{T}(\phi) \Psi_m^t(a/2, \phi) d\phi \right\}. \end{aligned} \quad (7.103)$$

For a scattering problem, q_m and s_m are given, while r_m and t_m need to be

determined. We arrange Eqs. (7.102) and (7.103) in matrix form as

$$\vec{U}(ka/2) = K^{UE} \cdot \begin{bmatrix} q_1 \\ q_2 \\ \vdots \\ s_1 \\ s_2 \\ \vdots \end{bmatrix} + K^{UA} \cdot \begin{bmatrix} r_1 \\ r_2 \\ \vdots \\ t_1 \\ t_2 \\ \vdots \end{bmatrix}, \quad (7.104)$$

and

$$\vec{I}(ka/2) = K^{IE} \cdot \begin{bmatrix} q_1 \\ q_2 \\ \vdots \\ s_1 \\ s_2 \\ \vdots \end{bmatrix} + K^{IA} \cdot \begin{bmatrix} r_1 \\ r_2 \\ \vdots \\ t_1 \\ t_2 \\ \vdots \end{bmatrix}. \quad (7.105)$$

By substituting Eqs. (7.104) and (7.105) into Eq. (7.90), the scattering parameters can be determined through

$$\begin{bmatrix} r_1 \\ r_2 \\ \vdots \\ t_1 \\ t_2 \\ \vdots \end{bmatrix} = S \cdot \begin{bmatrix} q_1 \\ q_2 \\ \vdots \\ s_1 \\ s_2 \\ \vdots \end{bmatrix}, \quad (7.106)$$

where S is the scattering matrix, which is

$$S = \{K^{UA} - Z(ka/2) \cdot K^{IA}\}^{-1} \cdot \{Z(ka/2) \cdot K^{IE} - K^{UE}\}. \quad (7.107)$$

If the short plane is included in the computation region, the above matrix equation has to be modified. Supposing that the short plane is located at the $z = L$ plane, then the PEC condition requires that

$$t_m = -s_m e^{2jk_{zm}L}. \quad (7.108)$$

When using this method, one difficulty is to calculate the elements of K^{UE} , K^{UA} , K^{IE} , and K^{IA} . The integrals cannot be calculated analytically. Although these can be evaluated by numerical methods, it will require much time. An alternative method is expanding the terms $\sin(m\pi x/a)e^{\pm jk_{zm}z}$ as Bessel-Fourier series,

$$\sin\left(\frac{m\pi}{2} + \frac{m\pi\rho \sin\phi}{a}\right)e^{\pm jk_{zm}\rho \cos\phi} = \sum_{i=-\infty}^{\infty} \sin\left(i\phi + \frac{m\pi}{2}\right)J_i(k\rho) \begin{cases} e^{\pm ji \arctan \frac{k_{zm}a}{m\pi}}, & m = 1; \\ \left(\frac{m\pi+a\sqrt{-k_{zm}^2}}{m\pi-a\sqrt{-k_{zm}^2}}\right)^{\pm \frac{i}{2}}, & m \geq 1. \end{cases} \quad (7.109)$$

Since the variables ρ and ϕ have been separated, the integrals can be calculated analytically. When using this transformation, the calculation must be done with caution. To obtain good results, the summation must include enough terms. However, with the increase of the absolute value of i , the value of the Bessel function $J_i(k\rho)$ decreases rapidly while $\left(\frac{m\pi+a\sqrt{-k_{zm}^2}}{m\pi-a\sqrt{-k_{zm}^2}}\right)^{\pm \frac{i}{2}}$ increases rapidly, thus the results are highly sensitive to the number of digits used in the calculation. Based on our numerical experiences, the calculations should be done with 30-digit precision. We use *Mathematica* to perform these calculations.

Generating matrices K^{UE} , K^{UA} , K^{IE} , and K^{IA} costs much time in the computing process. However, these matrices are independent of the material properties. Once these matrices have been generated, the scattering parameters of the material with varying properties can be calculated quickly.

Solutions

In this section, we present the calculation results by the OEM. The mode numbers are set to be 30, 31, 31, and 31 in the regions WI, WII, I, and II. The material used

in the calculation is mullite. Its dielectric properties, obtained from reference [50], are replotted in Fig. 7.10. Since the dielectric constant is a complex number, in some figures, temperature is used to represent the dielectric properties.

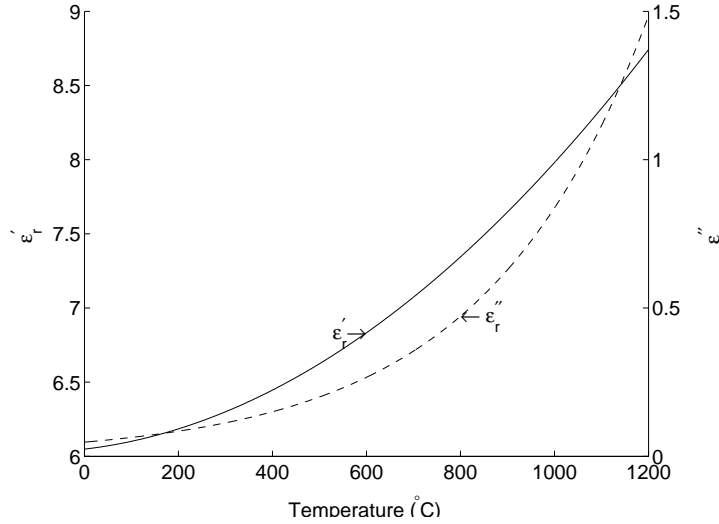


Figure 7.10: Dielectric property of mullite

Equivalent circuit parameters

As the first application, the OEM is used to calculate the parameters of the equivalent circuit. For the rod, two lumped parameters Z_b and Z_c , as illustrated in Fig. 6.6, need to be determined. These parameters are dependent on the radius and dielectric properties of the material. The calculated normalized impedances of mullite rods with radius 2.25 mm and 4.5 mm are shown in Figs. 7.11 and 7.12. In the figures, R_b , X_b and R_c , X_c are the resistances and reactances of Z_b and Z_c . The results given by *Waveguide Handbook*^[48] are also plotted for comparison. It can be seen that the differences are negligible. Indeed, the handbook values were calculated by a similar method. The fields inside the rod were also expanded in terms of Bessel functions. Since at that time it was impossible to select so many modes as we did, the authors applied variational methods to increase the accuracy^[64]. From these results, it is clear that the values given in *Waveguide Handbook*^[48] are accurate enough if we are only concerned with the equivalent circuit parameters.

Fields scattered by the rod

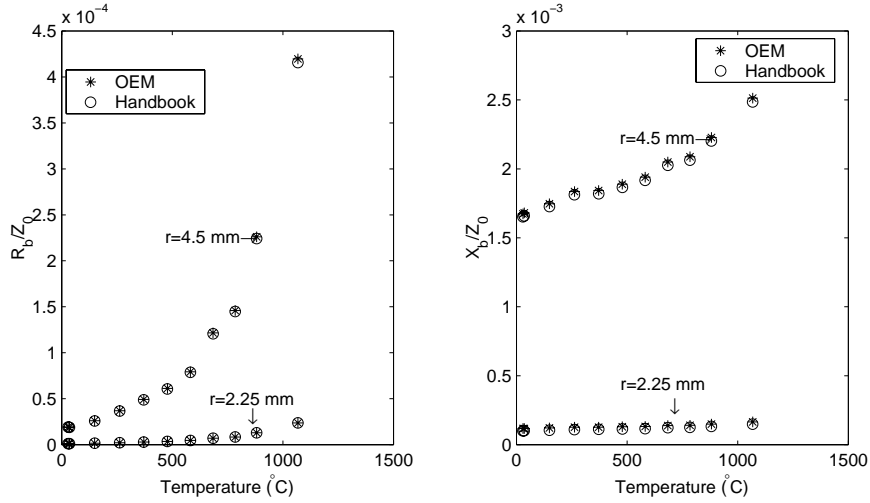


Figure 7.11: Comparison of the normalized impedance z_b .

Fig. 7.13 shows the electric field scattered by the rod. The calculation region includes the rod and the short plane, but not the iris. The rod is placed $0.75\lambda_g$ away from the short plane, where an electric field maximum exists if the rod is absent. The mullite rod is assumed to be at 1068°C . The corresponding dielectric constant and the radius are given in the figure. It can be seen that a small hump appears at the rod location. To see this clearly, Fig. 7.14 zooms in the local field around the rod.

We have discussed that the field pattern in the cavity is determined by the TE_{10} mode, thus it is interesting to compare the field obtained from the OEM with that obtained by only including the TE_{10} mode effect. We expect that the fields should be the same far away from the rod. This is verified by Fig. 7.15. In the figure, the unperturbed field, which is the field if the rod is absent, is also included. The curve labeled with WME stands for the electric field calculated by the waveguide mode extrapolation, i.e., we extrapolate the field in regions WI and WII to region I and II. It is clear that the field in the imaginary region can be calculated by WME. However, if we use WME to calculate the field inside the rod, errors occur. To see this clearly, the field inside and just outside the rod are illustrated in Fig. 7.16. It appears that WME and TE_{10} mode overestimates and underestimates the correct value of the field, respectively. Such errors vary with the dielectric constant of the rod. For the rod

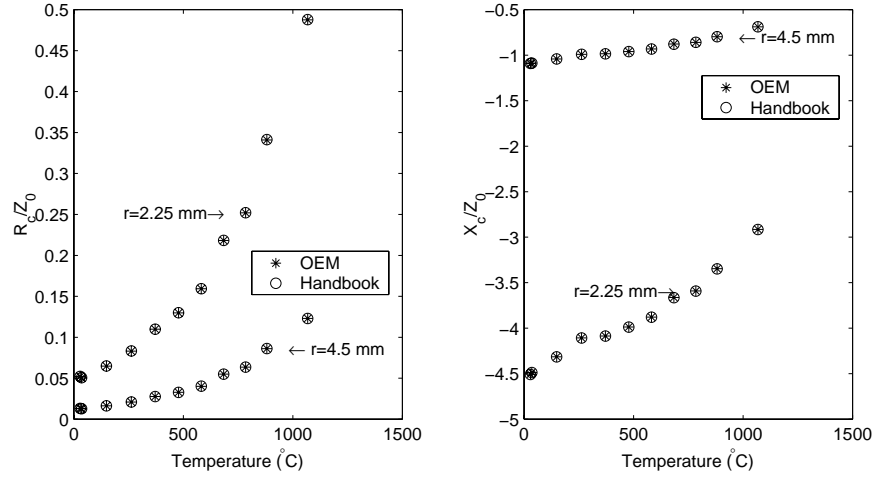


Figure 7.12: Comparison of the normalized impedance z_c .

with 2.25 mm, the values of the field and the relative error are shown in Fig. 7.17. Within the temperature range of 25°C to 1068°C , the relative error is less than 8% if we use the equivalent circuit to calculate the field. This is acceptable for general analysis.

With increasing radius, the distortion of the original field becomes more obvious. Fig. 7.18 shows the field pattern for a rod with a radius of 4.5 mm. A local field comparison is given in Fig. 7.19. The values of the electric fields at $r = 0$ calculated by different methods and the relative errors are shown in Fig. 7.20. It is seen that the relative error could be larger than 15% when using TE_{10} mode approximation.

The next interesting point is to estimate the electric field nonuniformity inside the rod in both the ρ and ϕ directions. Fig. 7.21 gives the electric field distribution along the ρ direction, where ϕ is set to zero. Indeed, this figure includes another curve, which is the electric field calculated by selecting only two modes inside the rod. From Eq. (7.58), this approximate electric field is

$$E_{y,ap} = a_0^i J_0(k_i \rho) \frac{1}{\sqrt{2\pi}} + \left[a_1^{is} J_1(k_i \rho) \frac{\sin \phi}{\sqrt{\pi}} + a_1^{ic} J_1(k_i \rho) \frac{\cos \phi}{\sqrt{\pi}} \right]. \quad (7.110)$$

These two curves coincide with each other in the figure. Next, we consider the electric field variation along the ϕ direction. Fig. 7.22 shows the OEM results

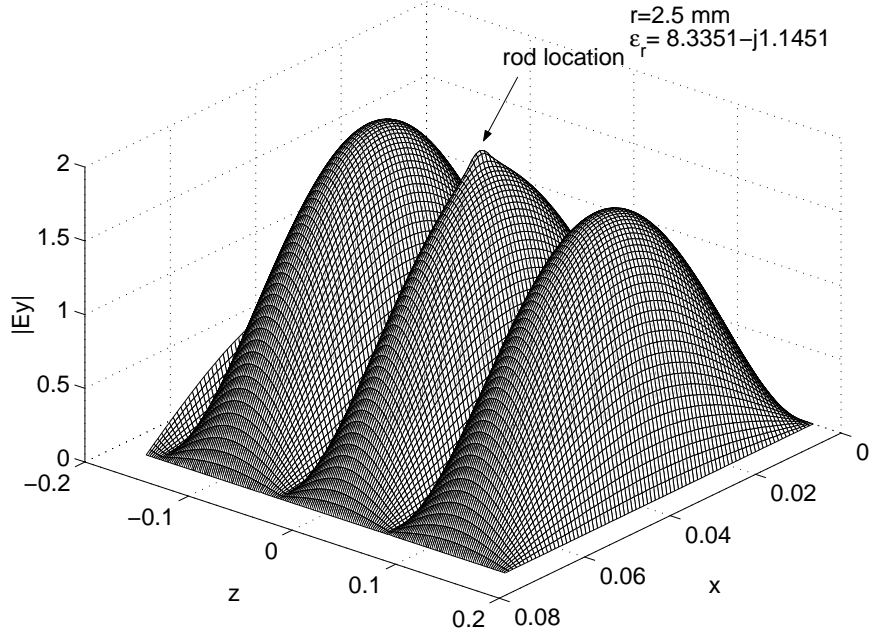


Figure 7.13: Electric field (y component) inside a cavity.

and the two term approximation. It is clear that Eq. (7.110) gives a very accurate representation of the field inside the rod. If we notice that the TE_{10} mode is an even function relative to the $x = a/2$ plane, the *sin* term will disappear, thus Eq. (7.110) can be simplified to be

$$E_{y,ap} = a_1 J_0(k_i \rho) + a_2 J_1(k_i \rho) \cos \phi, \quad (7.111)$$

where a_1 and a_2 are constants. Our interest here is to obtain the average electric field. From the two term approximate formulas, the average field is

$$E_{y,av} = \frac{1}{\pi r^2} \int_0^{2\pi} \int_0^r E_{y,ap} \rho d\rho d\phi. \quad (7.112)$$

The result of this integration is a hypergeometric function. For $r = 4.5 \text{ mm}$ and $\epsilon_r = 8.3351 - j1.1451$, $E_{y,av} = 0.945403|a_1|$. The constant a_2 does not appear in the result since *cos* function make the integration of the second term zero. If we want to use the electric field on the rod surface to approximate the average electric field inside the rod, a natural choice is to select the point $\rho = r$, $\phi = \pi/2$ since the constant a_2 can be canceled.

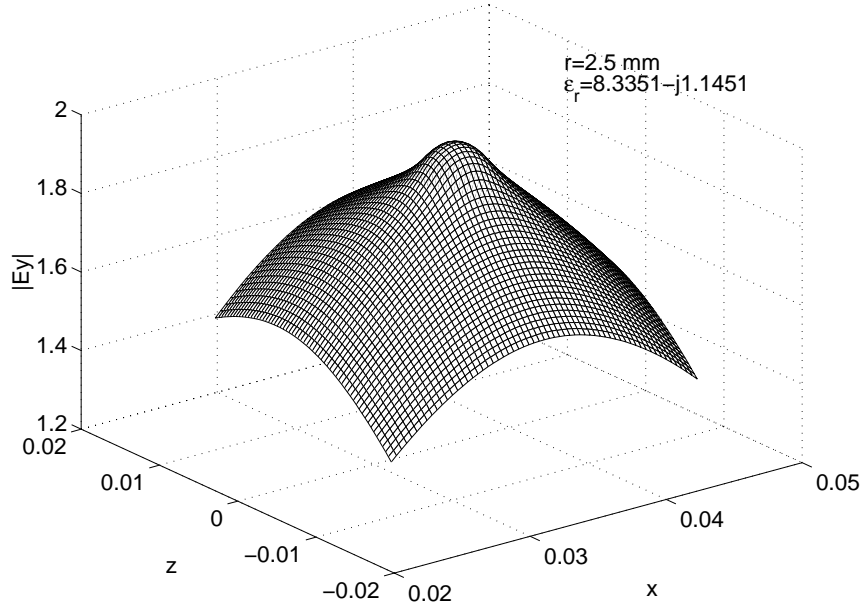


Figure 7.14: Electric field (y component) around the rod.

The absolute value of the electric field at this point is $0.891861|a_1|$ and the relative error is -5.7%.

We should notice that if the radius or the dielectric constant decreases, the relative error could be very small. For example, with $r = 2.25$ mm and the same ϵ_r , the relative error is only -1.4%. When doing numerical calculation, such relative errors are thought to be small enough since there are so many other factors which cannot be included in the numerical model.

7.2.2 Line source approximation

Based on the discussions in the previous section, if the radius and the dielectric constant of the rod are relatively small, the variation of the electric field along the ρ direction can be neglected. A qualitative measure of smallness is $k_i r \ll 1$. The properties of the material used in our experiment can approximately satisfy this condition. For example, the value of $k_i r \ll 1$ for a mullite rod with $r=2.25$ mm radius at the temperature of $1068^\circ C$ is 0.335. If this condition is satisfied, the rod

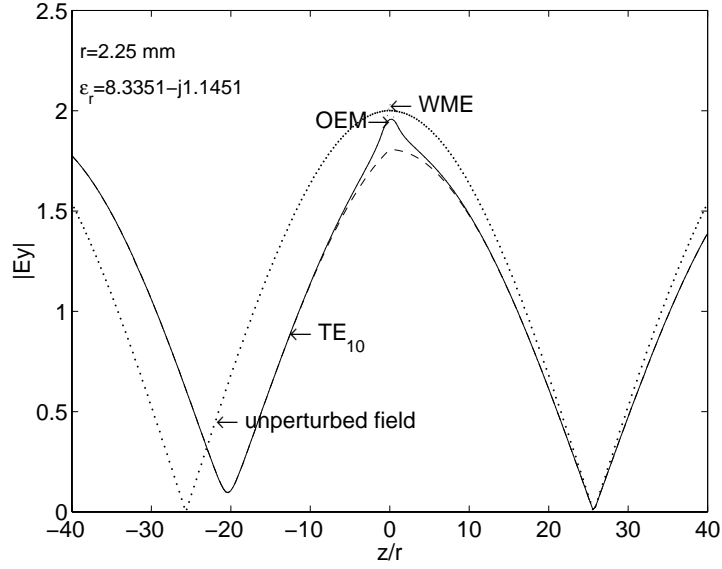


Figure 7.15: Comparison of the fields calculated by different methods.

can be replaced by a line source, which will make the analysis easier.

In the following sections, we will discuss the line source approximation. We will use the electric dyadic Green's function to derive the desired formulas. Although other methods, such as mode matching methods, can be used to obtain the same results, the introduction of Green's function will make the process more concise and straightforward.

Some useful theory tools in electromagnetics such as the source concept, image theory and equivalence principle will be used in this section. It is not possible and not necessary to give detailed descriptions of these subjects in this dissertation. The interested reader can find them in references^[18, 31].

Dyadic Green's function

The electric dyadic Green's function in a rectangular waveguide is the solution of the differential equation

$$(\nabla \times \nabla \times - k^2) \overline{\overline{\mathbf{G}}} = \overline{\overline{\mathbf{I}}} \delta(\mathbf{r} - \mathbf{r}') \quad (7.113)$$

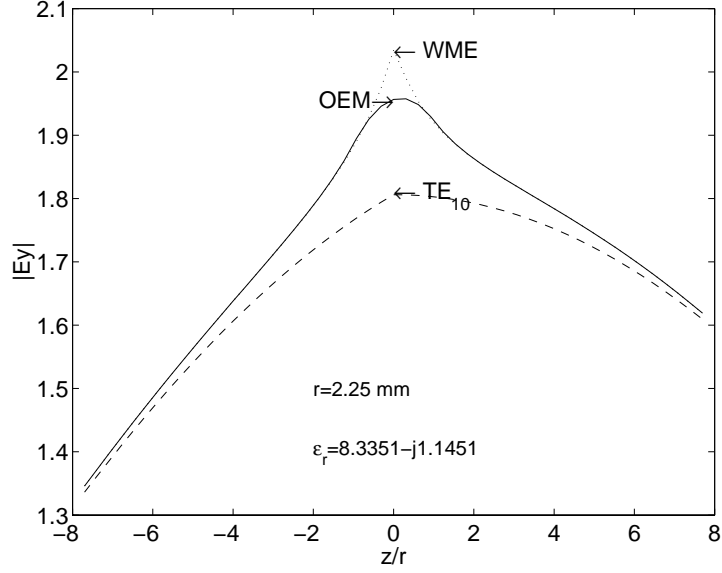


Figure 7.16: Comparison of the local fields calculated by different methods.

with the boundary condition

$$\hat{\mathbf{n}} \times \overline{\mathbf{G}} = 0 \quad \text{on the conducting boundary.} \quad (7.114)$$

The derivation of $\overline{\mathbf{G}}$ is given by Tai^[74] and Deshpande^[24]. Here we only list the results:

$$\overline{\mathbf{G}}(\mathbf{r}, \mathbf{r}') = p.v.\overline{\mathbf{G}}(\mathbf{r}, \mathbf{r}') - \frac{\hat{\mathbf{z}}\hat{\mathbf{z}}}{k^2}\delta(\mathbf{r} - \mathbf{r}'). \quad (7.115)$$

In the above expression, $p.v.\overline{\mathbf{G}}(\mathbf{r}, \mathbf{r}')$ is the conventional electric dyadic Green's function valid only outside the source region. The expression of $p.v.\overline{\mathbf{G}}(\mathbf{r}, \mathbf{r}')$ is

$$p.v.\overline{\mathbf{G}}(\mathbf{r}, \mathbf{r}') = \frac{1}{2abk^2} \sum_{m=0}^{\infty} \sum_{n=0}^{\infty} \frac{\epsilon_{0m}\epsilon_{0n}}{\gamma_{mn}} e^{-\gamma_{mn}|z-z'|} (\hat{\mathbf{x}}\hat{\mathbf{x}}g_{xx} + \hat{\mathbf{y}}\hat{\mathbf{x}}g_{yx} \pm \hat{\mathbf{z}}\hat{\mathbf{x}}g_{zx} \\ + \hat{\mathbf{x}}\hat{\mathbf{y}}g_{xy} + \hat{\mathbf{y}}\hat{\mathbf{y}}g_{yy} \pm \hat{\mathbf{z}}\hat{\mathbf{y}}g_{zy} \mp \hat{\mathbf{x}}\hat{\mathbf{z}}g_{xz} \mp \hat{\mathbf{y}}\hat{\mathbf{z}}g_{yz} + \hat{\mathbf{z}}\hat{\mathbf{z}}g_{zz}) \quad \text{for } z > z' \text{ or } z < z' \quad , \quad (7.116)$$

where

$$\epsilon_m^0 = \begin{cases} 2 & , \quad m = 0; \\ 1 & , \quad m \neq 0, \end{cases}$$

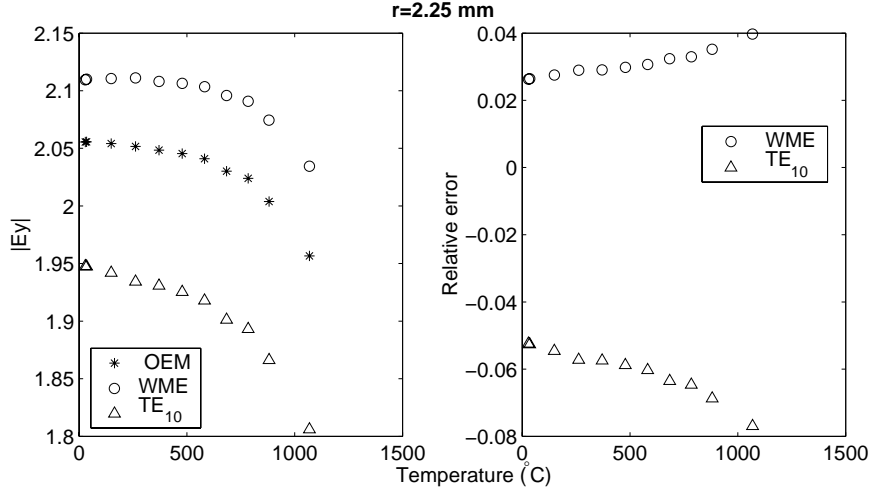


Figure 7.17: Comparison of the electric field at $\rho=0$ calculated by different methods.

and the components of the Green's Function are

$$g_{xx} = \left[k^2 - \left(\frac{m\pi}{a} \right)^2 \right] C_x C_{x'} S_y S_{y'}, \quad (7.117)$$

$$g_{yx} = \left(-\frac{m\pi}{a} \frac{n\pi}{b} \right) S_x C_{x'} C_y C_{y'}, \quad (7.118)$$

$$g_{zx} = \left(\pm \gamma_{mn} \frac{m\pi}{a} \right) S_x C_{x'} S_y S_{y'}, \quad (7.119)$$

$$g_{xy} = \left(-\frac{m\pi}{a} \frac{n\pi}{b} \right) C_x S_{x'} S_y C_{y'}, \quad (7.120)$$

$$g_{yy} = \left[k^2 - \left(\frac{n\pi}{b} \right)^2 \right] S_x S_{x'} C_y C_{y'}, \quad (7.121)$$

$$g_{zy} = \left(\pm \gamma_{mn} \frac{n\pi}{b} \right) S_x S_{x'} S_y C_{y'}, \quad (7.122)$$

$$g_{xz} = \left(\mp \gamma_{mn} \frac{m\pi}{a} \right) C_x S_{x'} S_y S_{y'}, \quad (7.123)$$

$$g_{yz} = \left(\mp \gamma_{mn} \frac{n\pi}{b} \right) S_x S_{x'} C_y S_{y'}, \quad (7.124)$$

$$g_{zz} = \left[\left(\frac{m\pi}{a} \right)^2 + \left(\frac{n\pi}{b} \right)^2 \right] S_x S_{x'} S_y S_{y'}. \quad (7.125)$$

In the above expressions, S_x , S_y , C_x and C_y stand for $\sin(m\pi x/a)$, $\sin(n\pi y/b)$, $\cos(m\pi x/a)$ and $\cos(n\pi y/b)$.

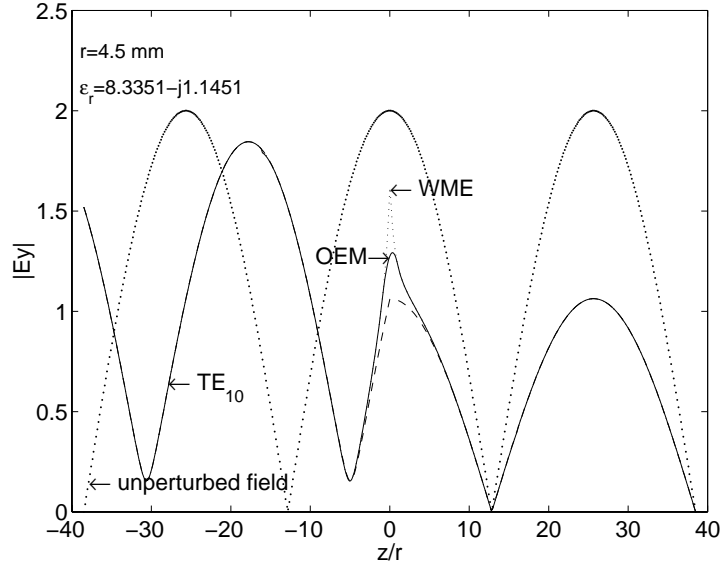


Figure 7.18: Comparison of the fields calculated by different methods.

Electric field induced by a line source

By the use of the electric dyadic Green's function, the electric field induced by a current density \vec{J} is

$$\vec{E} = -j\omega\mu \int \overline{\overline{\mathbf{G}}} \cdot \vec{J} dv. \quad (7.126)$$

In the following discussions, we consider the electric field induced by a line source oriented in the y direction,

$$\vec{J} = J(x, y, z)\hat{y} = I_y\delta(x - x')\delta(z - z')\hat{y}, \quad (7.127)$$

where I_y is the current, which could be y dependent.

Before substituting this expression into Eq. (7.126), it is necessary to change its variables as

$$\vec{J} = I_y\delta(x' - x'')\delta(z' - z'')\hat{y}, \quad (7.128)$$

thus the electric field produced by this line current is

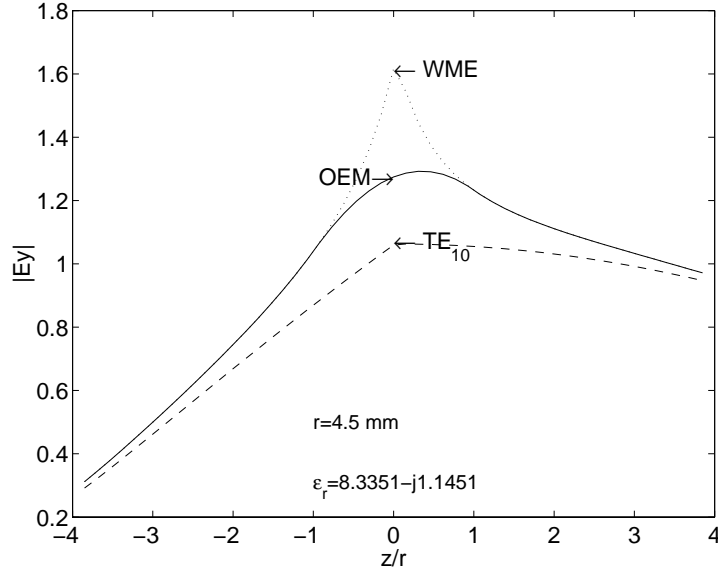


Figure 7.19: Comparison of the local fields calculated by different methods.

$$\begin{aligned}
\vec{E} &= -j\omega\mu \int \vec{\overline{G}} \cdot \vec{J} dv = -\omega\mu \int p.v. \vec{\overline{G}} \cdot \vec{J} dv' \\
&= -j \frac{\omega\mu}{2abk^2} \sum_{m=0}^{\infty} \sum_{n=0}^{\infty} \int I_y \frac{\epsilon_{0m}\epsilon_{0n}}{\gamma_{mn}} e^{-\gamma_{mn}|z-z'|} (\hat{x}g_{xy} + \hat{y}g_{yy} \pm \hat{z}g_{zy}) \delta(x-x')\delta(z-z') dv' \\
&= -j \frac{\omega\mu}{2abk^2} \sum_{m=0}^{\infty} \sum_{n=0}^{\infty} \frac{\epsilon_{0m}\epsilon_{0n}}{\gamma_{mn}} e^{-\gamma_{mn}|z-z'|} \left\{ \hat{x} \left(-\frac{m\pi}{a} \frac{n\pi}{b} \right) C_x S_{x''} S_y \right. \\
&\quad \left. + \hat{y} \left[k^2 - \left(\frac{n\pi}{b} \right)^2 \right] S_x S_{x''} C_y \pm \hat{z} \gamma_{mn} \frac{n\pi}{b} S_x S_{x''} S_y \right\} \int I_y C_{y'} dy'. \tag{7.129}
\end{aligned}$$

The y component of the electric field is

$$E_y = -j \frac{\omega\mu}{2abk^2} \sum_{m=0}^{\infty} \sum_{n=0}^{\infty} \frac{\epsilon_{0m}\epsilon_{0n}}{\gamma_{mn}} e^{-\gamma_{mn}|z-z'|} \left[k^2 - \left(\frac{n\pi}{b} \right)^2 \right] S_x S_{x''} C_y \int I_y(y') C_{y'} dy'. \tag{7.130}$$

Eq. (7.130) is the expression of the y component of the electric field produced by a line source in a waveguide.

Application to the rod problem

If we assume the electric field inside the rod is only dependent on y , a line source can be used to replace the rod based on the equivalence principle. If we use E_{rod} to

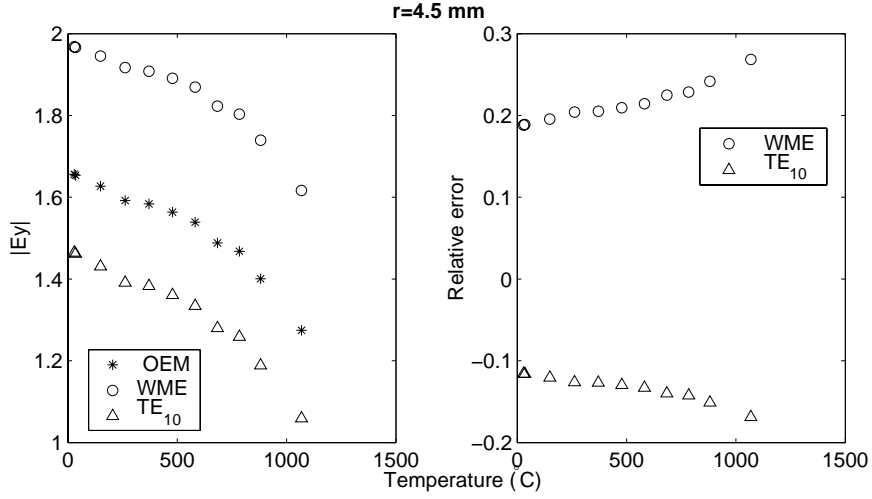


Figure 7.20: Comparison of the electric field at $\rho=0$ calculated by different methods.

represent the electric field along the rod, the equivalent current density is^[31]

$$J = j\omega(\varepsilon_r - 1)\varepsilon_0 E_{rod}, \quad (7.131)$$

and the current is

$$I_y = \pi r^2 J = j\pi r^2 \omega(\varepsilon_r - 1)\varepsilon_0 E_{rod}. \quad (7.132)$$

By substituting this expression into Eq. (7.130), the electric field produced by the rod is found to be

$$E_y = \frac{\pi r^2}{2ab} \sum_{m=0}^{\infty} \sum_{n=0}^{\infty} \frac{\varepsilon_{0m} \varepsilon_{0n}}{\gamma_{mn}} e^{-\gamma_{mn}|z-z''|} \left[k^2 - \left(\frac{n\pi}{b} \right)^2 \right] S_x S_{x'} C_y \int (\varepsilon_r - 1) E_{rod} C_{y'} dy'. \quad (7.133)$$

This is the integral equation used to solve for the electric field in the rod. To help understand this equation, we first consider a special case.

Constant line source

If I_y is independent of y , or is a constant, then $(\varepsilon_r - 1)E_{rod}$ can be moved out of the

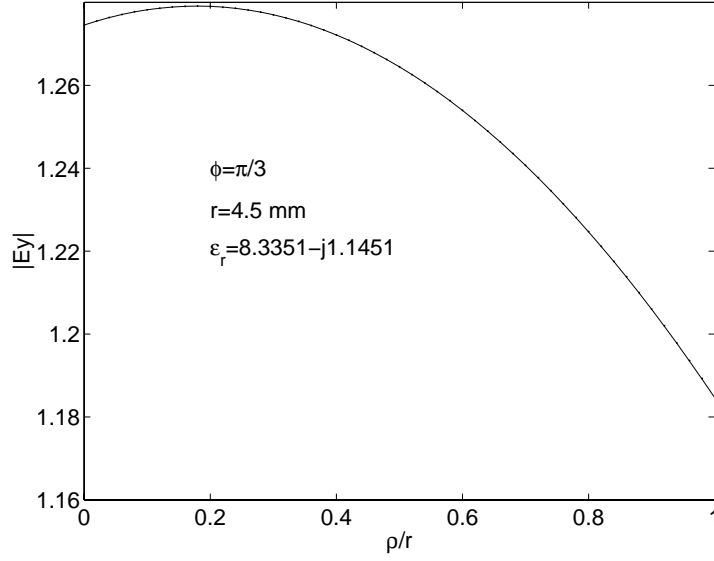


Figure 7.21: Electric field variation along ρ direction inside the rod.

integrand, so that Eq. (7.133) becomes

$$E_y = \frac{\pi r^2}{2ab} (\epsilon_r - 1) E_{rod} \sum_{m=0}^{\infty} \sum_{n=0}^{\infty} \frac{\epsilon_{0m} \epsilon_{0n}}{\gamma_{mn}} e^{-\gamma_{mn}|z-z''|} \left[k^2 - \left(\frac{n\pi}{b} \right)^2 \right] S_x S_{x'} C_y \int C_{y'} dy'. \quad (7.134)$$

If we notice that

$$\int C_{y'} dy = \int_0^b \cos\left(\frac{n\pi y}{b}\right) dy = \begin{cases} b & , \quad n = 0; \\ 0 & , \quad n \neq 0, \end{cases} \quad (7.135)$$

the above equation can be simplified to

$$E_y = \frac{\pi r^2 k^2}{a} (\epsilon_r - 1) E_{rod} \sum_{m=1}^{\infty} \frac{1}{\gamma_{m0}} e^{-\gamma_{m0}|z-z''|} \sin\left(\frac{m\pi x}{a}\right) \sin\frac{m\pi x''}{a}. \quad (7.136)$$

This equation can be used to calculate the reflection coefficient^[45]. If the rod is located at $x'' = a/2$ and $z'' = 0$, Eq. (7.136) becomes

$$E_y = \frac{\pi r^2 k^2}{a} (\epsilon_r - 1) E_{rod} \sum_{m=1}^{\infty} \frac{1}{\gamma_{m0}} e^{-\gamma_{m0}|z|} \sin\left(\frac{m\pi x}{a}\right) \sin\left(\frac{m\pi}{2}\right). \quad (7.137)$$

Obviously, the TE₁₀ mode reflection coefficient is

$$\Gamma_{10} = \frac{\pi r^2 k^2}{a} (\epsilon_r - 1) E_{rod} \frac{1}{\gamma_{10}}. \quad (7.138)$$

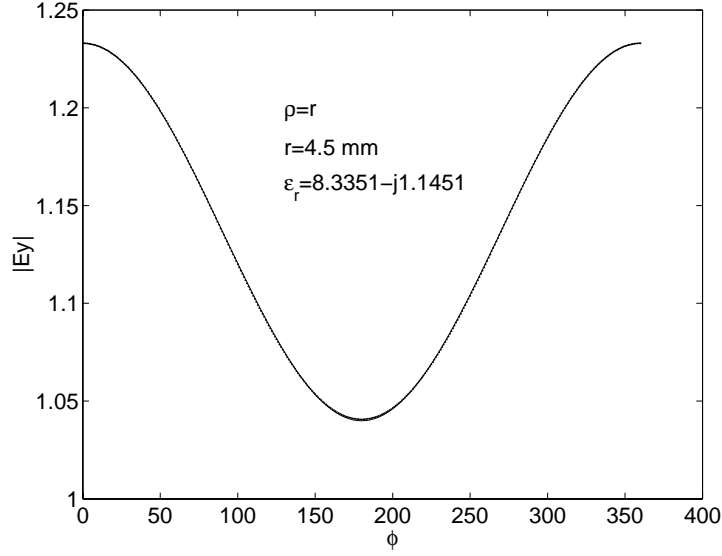


Figure 7.22: Electric field variation along ϕ direction inside the rod.

To obtain Γ_{10} , we must determine E_{rod} . Supposing the incident field is a TE_{10} mode with unit amplitude and the rod is located at $x'' = a/2$ and $z'' = 0$, then the total field is the summation of the incident field and the field produced by the rod,

$$E_t = e^{-\gamma_{10}z} \sin(\pi x/a) + \frac{\pi r^2 k^2}{a} (\epsilon_r - 1) E_{rod} \sum_{m=1}^{\infty} \frac{1}{\gamma_{m0}} e^{-\gamma_{m0}|z|} \sin\left(\frac{m\pi x}{a}\right) \sin\left(\frac{m\pi}{2}\right). \quad (7.139)$$

Although this is the total electric field produced by the incident field and the field scattered by the rod, this expression might not be valid inside the rod. When we use OEM method to solve the same problem, we showed that the extrapolation of the waveguide modes could overestimate the field. A more serious problem is the singularity property of the electric dyadic Green's function. The discussion is outside the scope of this dissertation, however, we can understand such a singularity through the following observation: suppose we use this expression to calculate the electric field at the point $(a/2, 0)$, then

$$E_{a/2,0} = 1 + \frac{\pi r^2 k^2}{a} (\epsilon_r - 1) E_{rod} \sum_{m=1}^{\infty} \frac{1}{\gamma_{m0}} \sin\left(\frac{m\pi}{2}\right) \sin\left(\frac{m\pi}{2}\right). \quad (7.140)$$

The summation in the above equation may be written as

$$S = \sum_{m=1}^{\infty} \frac{1}{\gamma_{m0}} \sin\left(\frac{m\pi}{2}\right) \sin\left(\frac{m\pi}{2}\right) = \sum_{m=1}^{\infty} \frac{1}{\sqrt{[(2m-1)\pi/a]^2 - k^2}}. \quad (7.141)$$

As m becomes large, the summation can be written as

$$S \approx \sum_{m=1}^M \frac{1}{\sqrt{[(2m-1)\pi/a]^2 - k^2}} + \frac{a}{\pi} \sum_{m=M+1}^{\infty} \frac{1}{2m-1}. \quad (7.142)$$

It is obvious that the second summation does not converge. Physically, we cannot apply Eq. (7.139) to the point $(a/2, 0)$ since this point coincides with the source point. Recall in last section, we divided the whole computational domain into four regions. If we only use the waveguide regions WI and WII to represent the field, the same difficulty occurs. Indeed, the point $(a/2, 0)$ is a singular point if the field is expressed in terms of only waveguide modes. A formal discussion can be found in reference [46].

To overcome this difficulty, we can evaluate Eq. (7.139) at a surface point. Based on the discussion in the OEM section, a good point is $(a/2 + r, 0)$. By putting $x = a/2 + r$ and $z = 0$ into Eq. (7.139), we obtain

$$E_{rod} = \sin\left[\frac{\pi(a/2 + r)}{a}\right] + \frac{\pi r^2 k^2}{a} (\varepsilon_r - 1) E_{rod} \sum_{m=1}^{\infty} \frac{1}{\gamma_{m0}} \sin\left[\frac{m\pi(a/2 + r)}{a}\right] \sin\left(\frac{m\pi}{2}\right). \quad (7.143)$$

Since the assumption of this method is that $r/a \ll 1$, we can set $r = 0$ in the first term but not in the series, thus

$$E_{rod} = 1 + \frac{\pi r^2 k^2}{a} (\varepsilon_r - 1) E_{rod} \sum_{m=1}^{\infty} \frac{1}{\gamma_{m0}} \sin\left[\frac{m\pi(a/2 + r)}{a}\right] \sin\left(\frac{m\pi}{2}\right). \quad (7.144)$$

If we set

$$S = \sum_{m=1}^{\infty} \frac{1}{\gamma_{m0}} \sin\left[\frac{m\pi(a/2 + r)}{a}\right] \sin\left(\frac{m\pi}{2}\right), \quad (7.145)$$

and

$$C = \frac{\pi r^2 k^2}{a} (\varepsilon_r - 1), \quad (7.146)$$

then

$$E_{rod} = \frac{1}{1 - CS} . \quad (7.147)$$

Next, we will include the short plane in the system. The easiest way to do this is by image theory. Supposing the short plane is at $z = L$, we add an image line source at $z'' = 2L$ with negative amplitude, and thus Eq. (7.136) becomes

$$E_y = \frac{\pi r^2 k^2}{a} (\varepsilon_r - 1) E_{rod} \sum_{m=1}^{\infty} \frac{1}{\gamma_{m0}} (e^{-\gamma_{m0}|z|} - e^{-\gamma_{m0}|z-2L|}) \sin\left(\frac{m\pi x}{a}\right) \sin\left(\frac{m\pi}{2}\right). \quad (7.148)$$

The field point at $(a/2 + r, 0)$ is

$$E_y = \frac{\pi r^2 k^2}{a} (\varepsilon_r - 1) E_{rod} \sum_{m=1}^{\infty} \frac{1}{\gamma_{m0}} (1 - e^{-\gamma_{m0}2L}) \sin\left[\frac{m\pi(a/2 + r)}{a}\right] \sin\left(\frac{m\pi}{2}\right). \quad (7.149)$$

As a general assumption, the local electric field around the rod will not be affected by the higher order modes produced by the short plane, or all $e^{-\gamma_{m0}2L}$ terms are negligible as $m > 1$. If we still use S to represent the series summation, under this assumption, the summation is

$$S = \sum_{m=1}^{\infty} \frac{1}{\gamma_{m0}} \sin\left[\frac{m\pi(a/2 + r)}{a}\right] \sin\left(\frac{m\pi}{2}\right) - \frac{e^{-\gamma_{10}2L}}{\gamma_{10}}. \quad (7.150)$$

Comparing this expression with Eq. (7.145), we notice that the only difference is the last term which accounts for the short plane effect.

When we use image theory, we must also add an image for the incident field, which is a TE_{10} mode with a negative unity amplitude originating from $z = 2L$ and propagating in the $-z$ direction; thus the total incident field is

$$E_{inc} = e^{-\gamma_{10}z} \sin(\pi x/a) - e^{\gamma_{10}(z-2L)} \sin(\pi x/a). \quad (7.151)$$

At the point $(a/2 + r, 0)$, the total incident field is

$$E_{inc} = \sin\left[\frac{\pi(a/2 + r)}{a}\right] (1 - e^{-2\gamma_{10}L}). \quad (7.152)$$

By adding the incident field and the field produced by the rod, the electric field at the $(a/2 + r, 0)$ point is

$$E_{rod} = CSE_{rod} + (1 - e^{-2\gamma_{10}L}). \quad (7.153)$$

In the above equation, we have taken $r = 0$ if the $\sin [(m\pi(a/2 + r)/a)]$ term is not in the summation series. The expressions for C and S are given by Eq. (7.146) and (7.150). Therefore, the electric field at the rod is computed as

$$E_{rod} = \frac{1 - e^{-2\gamma_{10}L}}{1 - CS}. \quad (7.154)$$

When using this method to calculate the reflection coefficient and the electric field in the rod, the only difficulty is the calculation of the series summation. As we have discussed, if we set $x = a/2$ rather than $x = a/2 + r$, the series is not convergent. Since r is small, it is expected that the series converges very slowly. This problem can be solved by extracting the dominant part of the summation as a closed-form expression. The remainder is a rapidly converging series^[18].

The summation excluding the term $e^{-\gamma_{m0}2L}/\gamma_{10}$ can be written as

$$S' = \sum_{m=1}^{\infty} \frac{1}{\gamma_{m0}} \sin \left[\frac{m\pi(a/2 + r)}{a} \right] \sin \left(\frac{m\pi}{2} \right) = (S' - D) + D, \quad (7.155)$$

where

$$D = \frac{a}{\pi} \sum_{m=1}^{\infty} \frac{1}{m} \sin \left[\frac{m\pi(a/2 + r)}{a} \right] \sin \left(\frac{m\pi}{2} \right) = \frac{a}{2\pi} \log \left(\frac{2a}{\pi r} \right), \quad (7.156)$$

and

$$S' - D = \frac{a}{\pi} \sum_{m=1}^{\infty} \left(\frac{1}{\sqrt{m^2 - (ka/\pi)^2}} - \frac{1}{m} \right) \sin \left[\frac{m\pi(a/2 + r)}{a} \right] \sin \left(\frac{m\pi}{2} \right). \quad (7.157)$$

The convergence rates are compared in Fig. 7.23.

From the figure, it is apparent that only 20 terms are necessary to obtain a convergent result. Such a summation method is a very important part in the Schwinger transformation^[64].

The results calculated by this method are shown in Figs. 7.24 and 7.25. For comparison, we also include the results calculated by other methods described in last section. It is seen that this method can lead to fairly accurate estimation of the electric field inside the rod. The relative error for the rod with $r=2.25$ mm and $r=4.5$ mm are around 2% and 5%, respectively. These errors are much smaller than those obtained by the equivalent circuit calculation.

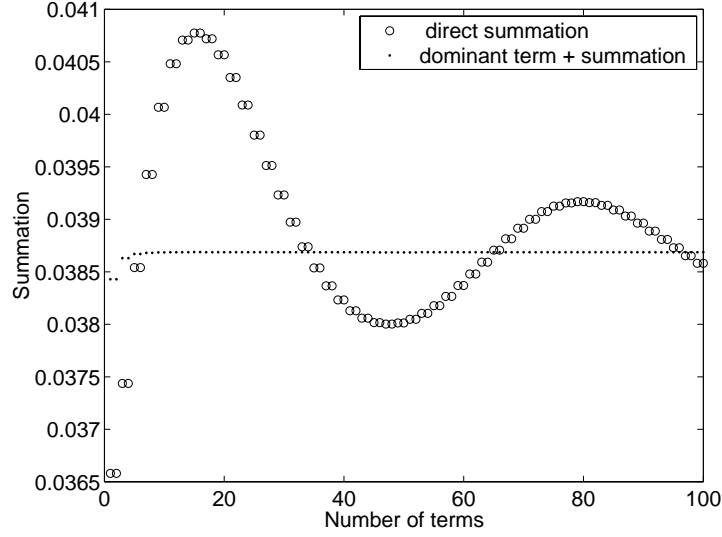


Figure 7.23: Comparison of the convergence rate by different summation methods.

Since this method can give an accurate estimation of the electric field in the rod, we are confident in using it to handle the problem where the dielectric properties of the rod vary along the y direction.

Varying line source

Suppose the rod and the short are located at the $z = 0$ and $z = L$ planes. By the use of image theory, the electric field scattered by the rod is

$$E_y = \frac{\pi r^2}{2ab} \sum_{m=0}^{\infty} \sum_{n=0}^{\infty} \frac{\epsilon_{0m} \epsilon_{0n}}{\gamma_{mn}} (e^{-\gamma_{mn}|z|} - e^{-\gamma_{mn}|z-2L|}) \left[k^2 - \left(\frac{n\pi}{b} \right)^2 \right] \sin\left(\frac{m\pi}{2}\right) \sin\left(\frac{m\pi x}{a}\right) \cos\left(\frac{n\pi y}{b}\right) \int (\epsilon_r - 1) E_{rod} \cos\left(\frac{n\pi y'}{a}\right) dy'. \quad (7.158)$$

This equation is obtained by summing the fields produced by the two line sources

$$J_1 = I_y \delta(x' - a/2) \delta(z' - 0), \quad (7.159)$$

and

$$J_2 = -I_y \delta(x' - a/2) \delta(z' - 2L), \quad (7.160)$$

where I_y is given by Eq. (7.132).

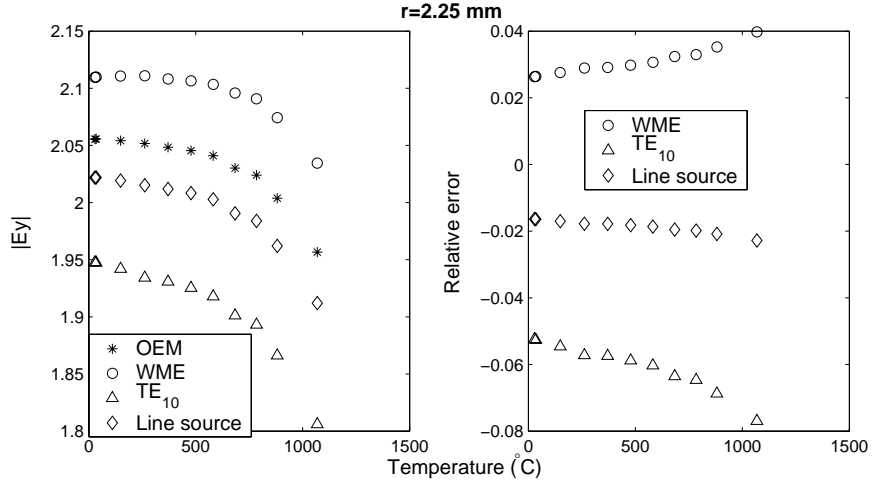


Figure 7.24: Comparison of the electric field at $\rho=0$ calculated by OEM and line source methods.

From Eq. (7.158), the TE_{10} mode reflection coefficient due to the rod and short plane is⁴

$$\Gamma_{10} = \frac{\pi r^2 k^2}{ab\gamma_{10}} (1 - e^{-2\gamma_{10}L}) \int (\varepsilon_r - 1) E_{rod} dy'. \quad (7.161)$$

If we define

$$\overline{(\varepsilon_r - 1) E_{rod}} = \frac{\int (\varepsilon_r - 1) E_{rod} dy'}{b}, \quad (7.162)$$

then TE_{10} mode reflection coefficient is

$$\Gamma_{10} = \frac{\pi r^2 k^2}{a\gamma_{10}} (1 - e^{-2\gamma_{10}L}) \overline{(\varepsilon_r - 1) E_{rod}}, \quad (7.163)$$

thus Γ_{10} is determined by the average value of $(\varepsilon_r - 1) E_{rod}$ along the rod.

Our remaining task is to determine the electric field along the rod.

As we discussed previously, when we calculate the electric field using the image theory, the incident field is composed of the original incident field and its image, as shown in Eq. (7.151), thus the total fields along the surface line ($x = a/2 + r, z = 0$)

⁴This Γ_{10} does not include the incident image. The correct value should add a term $-e^{-2\gamma_{10}L}$.

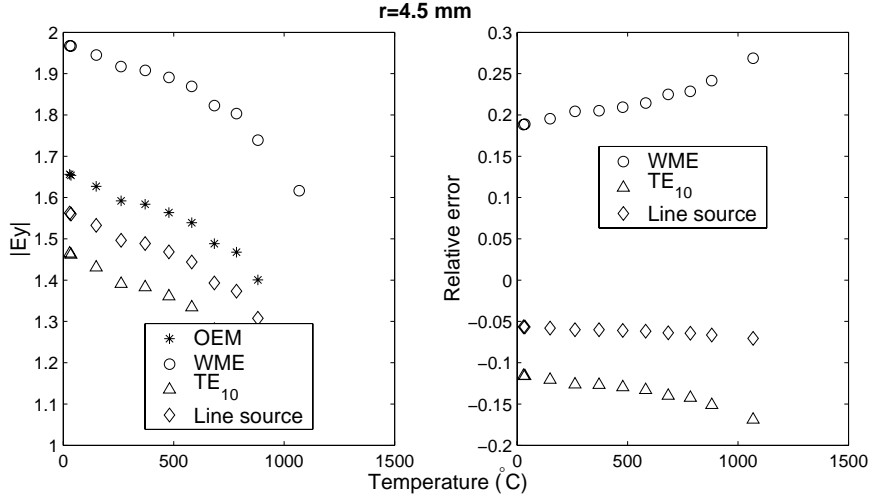


Figure 7.25: Comparison of the electric field at $\rho=0$ calculated by OEM and line source methods.

are

$$\begin{aligned}
 E_{rod}(y) = & \frac{\pi r^2}{2ab} \sum_{m=0}^{\infty} \sum_{n=0}^{\infty} \frac{\epsilon_{0m} \epsilon_{0n}}{\gamma_{mn}} (1 - e^{-\gamma_{mn} 2L}) \left[k^2 - \left(\frac{n\pi}{b} \right)^2 \right] \sin\left(\frac{m\pi}{2}\right) \sin\left[\frac{m\pi(a/2+r)}{a}\right] \\
 & \left[\int (\epsilon_r(y') - 1) E_{rod}(y') \cos\left(\frac{n\pi y'}{a}\right) dy' \right] \cos\left(\frac{n\pi y}{b}\right) \\
 & + \sin\left[\frac{\pi(a/2+r)}{a}\right] (1 - e^{-2\gamma_{10}L}).
 \end{aligned} \tag{7.164}$$

This is a Fredholm integral equation, where the unknown $E_{rod}(y)$ appears on both sides. This equation could be solved by expanding E_{rod} in terms of $\cos(n\pi y'/a)$. However, due to the nonlinear term of $[\epsilon_r(y') - 1]E_{rod}(y')$, the advantage of the expansion method is not obvious. We will use point matching (collocation) methods to solve this integral equation. Indeed, one advantage of the integral form of the equation is that the solution region is confined in the rod. This can significantly reduce the necessary number of points to obtain reasonable results.

As in the constant line source problem, the main difficulty in this problem is still the summation. Unlike the problem we discussed in the last section, we encounter a summation of double infinite series. This is much more difficult than the summation of a single infinite series and no widely acknowledged techniques are available.

One trouble in the double infinite series summation is the term $k^2 - (n\pi/b)^2$.

This term increases rapidly with increasing n . For our problem, we assume that $E_{rod}(y)$ can be accurately described by a few term expansion of $\cos(n\pi y/b)$. This means the summation for n can be truncated at some small number. This assumption is reasonable because E_y is uniform before the introduction of the rod. The nonuniformity of E_y is due to the temperature variation along the rod. We expect that heat conduction reduces the nonuniformity of the temperature field along the rod inside the cavity.

We write the term including m in Eq. (7.164) as

$$\Xi(n) = \sum_{m=1}^{\infty} \frac{\epsilon_{0n}}{\gamma_{mn}} (1 - e^{-\gamma_{mn}2L}) \sin\left(\frac{m\pi}{2}\right) \sin\left[\frac{m\pi(a/2+r)}{a}\right]. \quad (7.165)$$

We have dropped the factor ϵ_{0m} since $m \neq 0$ in our problem. Also we notice the term $e^{-\gamma_{mn}2L}$ is important only when $m = 1$ and $n = 0$, thus

$$\Xi(0) = 2\left\{-\frac{e^{-\gamma_{10}2L}}{\gamma_{10}} + \sum_{m=1}^{\infty} \frac{1}{\gamma_{m0}} \sin\left(\frac{m\pi}{2}\right) \sin\left[\frac{m\pi(a/2+r)}{a}\right]\right\}, \quad (7.166)$$

and

$$\Xi(n) = \sum_{m=1}^{\infty} \frac{1}{\gamma_{mn}} \sin\left(\frac{m\pi}{2}\right) \sin\left[\frac{m\pi(a/2+r)}{a}\right] \quad n \neq 0. \quad (7.167)$$

By applying the same techniques we discussed in the constant line source section, the values of these terms can be obtained quickly. We must point out that we do not solve the double infinite series summation problem. If n were very large, the proposed method will fail or at least require for much time to compute the summations. Fortunately, the Fourier coefficient of a function decreases rapidly, thus our assumption should be valid.

Since the point matching technique is a common method in every computational field, we will not list the solution procedure. Detailed information can be found in several references^[25, 87].

The calculated results will be shown in the next Chapter, where this method is incorporated into the heat transfer model developed by Goodson^[29] and McConnell^[50].

Chapter 8

Interpretation of the Experimental Results

Contrary to most conclusions from theoretical modeling, we find that middle branch of the S-shaped curve is stable for the mullite and alumina rods we used in our experiments. In Section 8.1, we will use the equivalent circuit model to explain this phenomenon. This model is an improvement of a model developed by Davis^[89]. In Section 8.2, the results of a full numerical model are provided.

8.1 Equivalent Circuit Model

The equivalent circuit model has been discussed in Chapter 6. We incorporate the equivalent circuit parameters calculated in Chapter 7 into the model to explain the experimental results. In the following discussion, we use the mullite rod as the sample.

For convenience, we replot Figs. 6.6 and 6.7 as Figs. 8.1 and 8.2. Since the value of z_b is small, the voltage at plane 3 and 4 are almost the same. We select V_3 as the voltage in the rod. As we have discussed, V_3 is a measure of the electric field E_y in the rod, thus we use E_y to replace V_3 in the following discussion. E_y is a function of z_a , z_b , z_c , L_1 and L_2 . In our heating system, z_a and L_1 are fixed. z_b and z_c are functions of the diameter of the rod and the temperature of the rod through the dielectric constant. Therefore, E_y is a function of the diameter and temperature

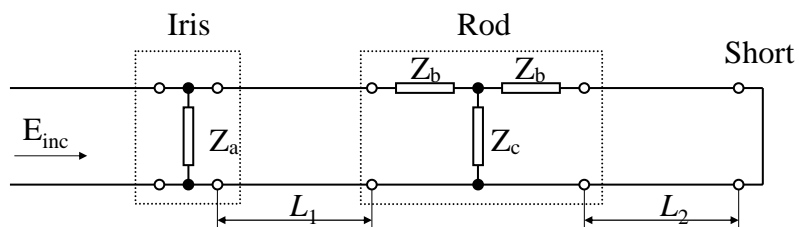


Figure 8.1: The equivalent circuit for the microwave heating system

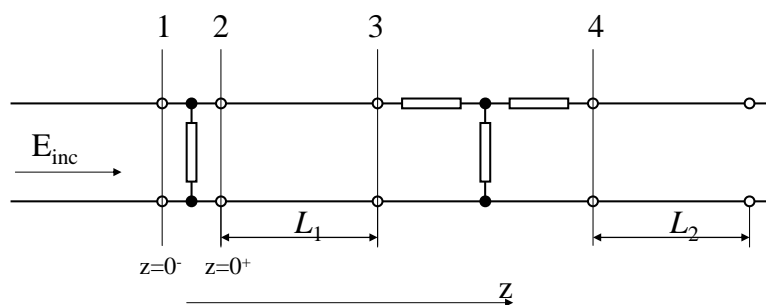


Figure 8.2: Four planes in the equivalent circuit model

of the rod and L_2 . Although the expression of E_y is an algebraic equation, it is very complex, thus we use figures to help in discussing the results.

In Fig. 8.3, we plot the variation of the electric field in the rod with L_2 for various rod temperatures. First, there is a maximum electric field for any temperature. This maximum value is a function of L_2 . This means at the specified temperature, the efficiency of heating the rod varies with L_2 , thus with the cavity length. It is also shown that to heat the rod from low temperature to high temperature, decreasing the cavity length is a natural choice. From this figure, we see that the maximum electric field decreases with increasing temperature. This means if the output power is set too low, the power level has to be increased when temperature increases.

If the incident power level is suitable, then the direction of movement of the short plane is important. Starting with the cavity highly detuned, decreasing the cavity length tends to tune the cavity and the temperature of the sample increases. This is illustrated by Fig. 8.4. In the figure, every curve represents the variation

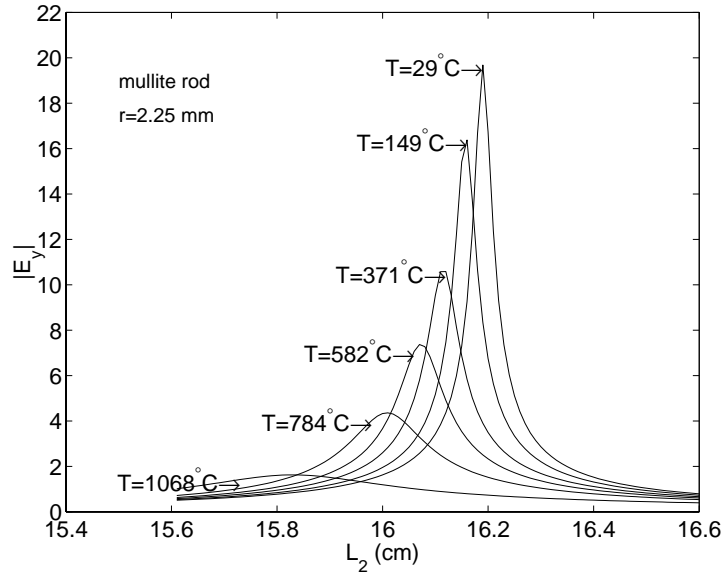


Figure 8.3: The variation of the electric field in the rod with the temperature and L_2

of the electric field with the temperature while L_2 is fixed. These curves give the dynamic heating process at fixed cavity length. On these curves, the electric field is determined by the temperature through the dielectric properties of the rod, then the electric field can be used to calculate the power dissipation. To illustrate the dynamic process clearly, we plotted these curves on the experimentally obtained S-shaped curve of the mullite rod in the following paragraphs. Since every point on the S-shaped curve represents a thermally balanced state, the heat loss is equal to the power dissipation at these points. On the dynamic heating process curves, by comparing the power dissipation with the heat loss, the variation trend of the temperature can be determined.

If we continue to decrease the cavity length, we will pass the critical point a . Around this point, the electric field will increase first if we shorten the length of the cavity. The energy balance forces the temperature of the sample to rise, which detunes the cavity. Although the cavity is detuned, the absorbed energy is still larger than the heat loss, thus temperature continues increasing until it reaches the S curve. This process is also illustrated in Fig. 8.4.

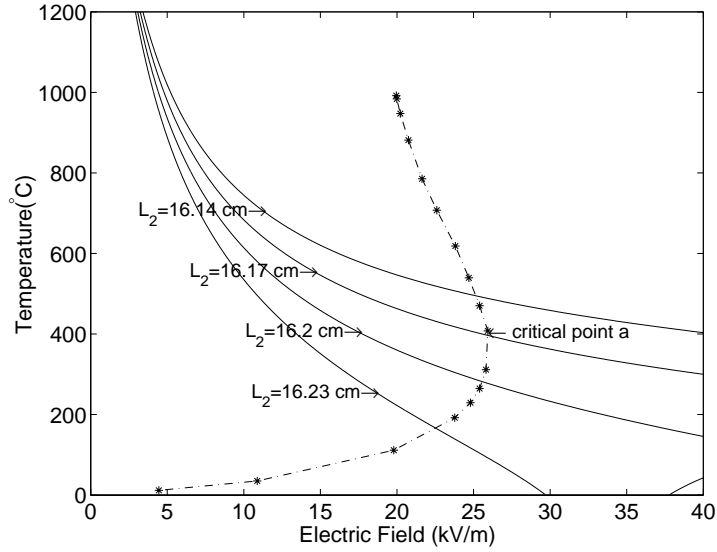


Figure 8.4: Behavior of electric field and temperature for decreasing cavity length. The dashed curve is the experimentally obtained S-shaped curve of the mullite rod, while the solid curves represent the electric field solutions at fixed cavity length.

If the cavity is highly detuned because the length of the cavity is too small, we must increase the cavity length to tune the cavity to heat the sample. At first the process is stable, but around the critical point c , if the length of the cavity is increased, the process becomes unstable since the electric field versus temperature curves will circumvent the S curve. This process may end at a higher temperature, or thermal runaway may occur. The process is shown in Fig. 8.5.

From Fig. 8.5, we can observe an interesting phenomenon. If the cavity length is increased to tune the cavity, the maximum temperature can be attained by the rod is smaller than that attained by decreasing the cavity length. Starting from the equilibrium point e_1 at $L_2 = 15.67$ cm, increasing the cavity length will lead to the equilibrium point e_2 at $L_2 = 15.69$ cm. The temperature at point e_2 is smaller than that at point e_1 . If we continue increasing the cavity length, the temperature continues decreasing; thus the temperature at point e_1 is the maximum temperature of the rod can be attained. Apparently, the temperature at point e_3 is higher than that at point e_1 . This higher temperature can be attained only by decreasing the cavity length. This phenomenon is observed when heating the alumina rod with a diameter

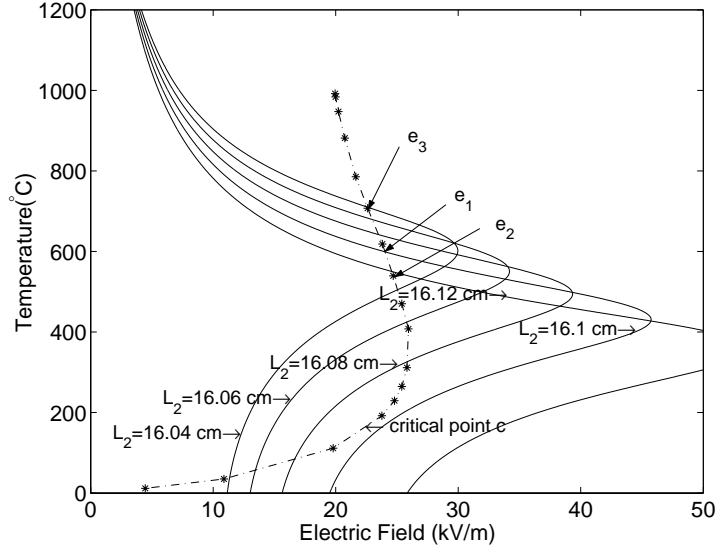


Figure 8.5: Behavior of electric field and temperature for increasing cavity length. The dashed curve is the experimentally obtained S-shaped curve of the mullite rod, while the solid curves represent the electric field solutions at fixed cavity length.

of 4.5 mm (Figs. 5.8 and 5.9).

Next, we consider another heating method which has been used by some researchers^[80, 93]. During the heating process, the cavity length is fixed while the input power is increased to heat the material to a higher temperature. This heating process could be stable if the cavity length is selected so that the cavity is not at a highly tuned state, as illustrated in Fig. 8.6. In the figure, E_{in} is the incident electric field with units kV/m, which is a measure of the output power from the generator. As the incident field increases 9 fold from the initial electric field, the rod can be heated to 500°C. Normally, in the experiments, the cavity is set to be at a tuned state. Under such condition, the heating process could become unstable, as illustrated in Fig. 8.7. In this figure, the rod can be heated to temperatures higher than 500°C when E_{in} is around 4. However, with the increasing power level, the thermal excursion occurs.

In Fig. 8.8, we show the effects of the rod size on the electric field in the cavity. Compared with the results shown in Fig. 8.3, the maximum electric field inside the rod is much lower. This make it difficult to heat a thick rod, as we observed in the experiment.

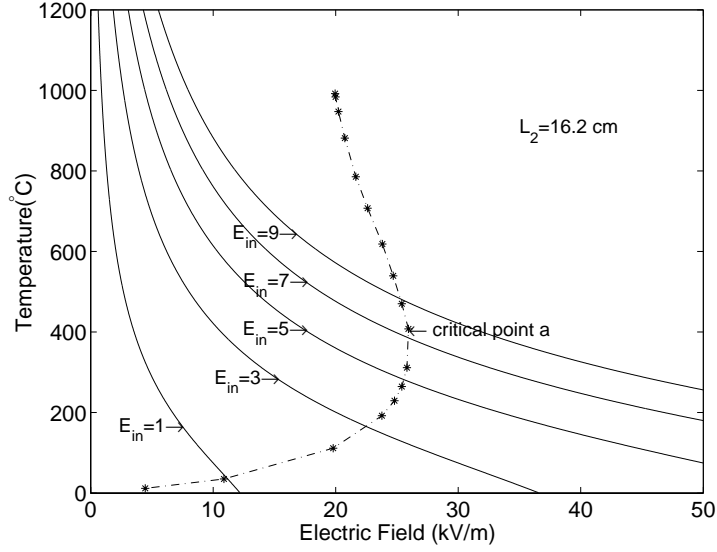


Figure 8.6: A stable heating process achieved by increasing the output power of the generator.

The equivalent circuit model can explain most phenomena occurring in the experiments. However, it cannot demonstrate that if the output power of the generator is set too high, a thermal excursion cannot be avoided even by decreasing the cavity length, as observed in the experiment. Davis developed a model to explain this phenomenon^[22]. This model was developed by also simulating the cavity by an equivalent circuit, as shown in Fig. 8.9.

The electric field at the sample is written as:

$$E = \frac{kI_s}{G_s + G_x + j[B_x - Y_0 \cot(k_{10}L_2)]} = \frac{E_0}{1 + g_x + j[b_x - y_0 \cot(k_{10}L_2)]} \quad (8.1)$$

where E_0 represents the peak electric field in the cavity without a sample. Since g_x and b_x represent the sample properties, they can be defined by

$$g_x + jb_x = \omega c_0 (\epsilon_r'' + \epsilon_r'). \quad (8.2)$$

Thus

$$E = \frac{E_0}{1 + \omega c_0 \epsilon_r'' + j[\omega c_0 \epsilon_r' - y_0 \cot(k_{10}L_2)]} \quad (8.3)$$

where k_{10} is the wavenumber of the TE₁₀ mode in the waveguide.

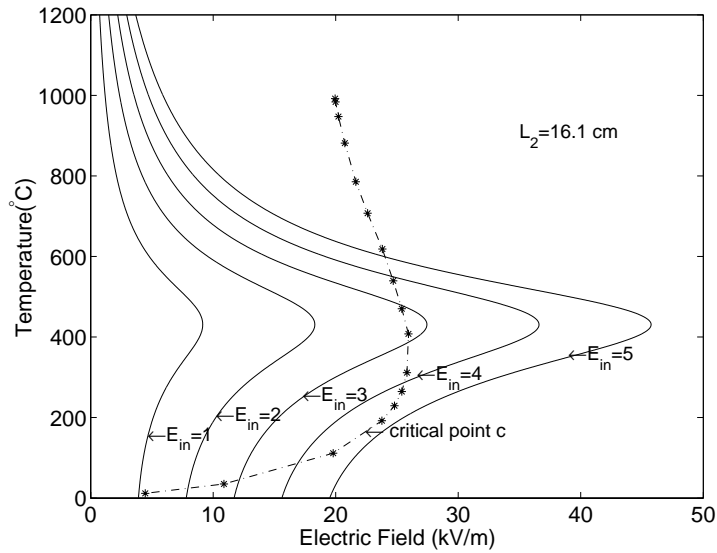


Figure 8.7: An unstable heating process by increasing the output power of the generator.

The two unknown numbers c_0 and y_0 represent the properties of the sample and waveguide. By correctly selecting the values of c_0 and y_0 , this model can explain all phenomena occurring in the experiment. For example, if the incident power level is too high, the process around critical point a is unstable even when decreasing the cavity length, as shown in Fig. 8.10.

The inclusion of the loss is the major difference between this model and the model we are currently using. However, the loss effects cannot be easily incorporated into the equivalent circuit model because some sources are difficult to evaluate, such as the loss on the iris plane.

Although the equivalent circuit model does not perfectly explain the experimental results, it is an easy and useful tool. It can provide a guideline for microwave heating in a resonant cavity.

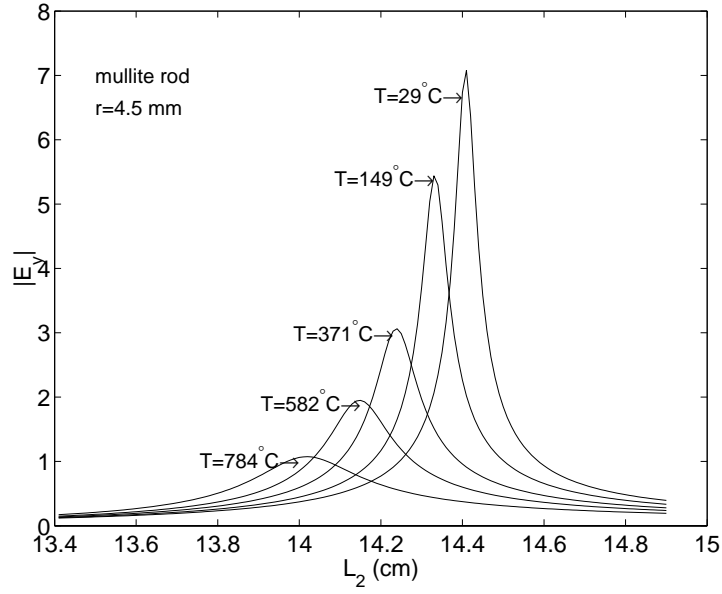


Figure 8.8: The variation of the electric field in the rod with the temperature and L_2

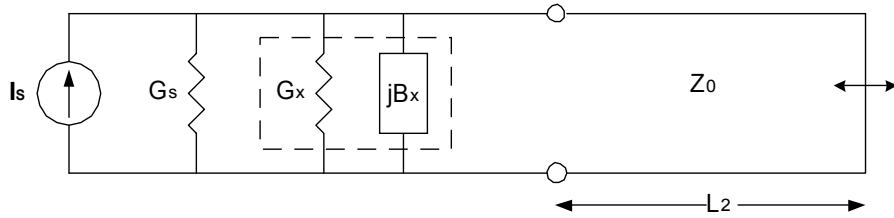


Figure 8.9: Transmission line model for cavity.

8.2 Numerical Model

In this section, we show the results obtained from a coupled heat transfer and electromagnetic field model. The governing equations of the heat transfer model are^[29]

$$\rho_d C_p \frac{\partial T}{\partial t} = \frac{1}{\rho} \frac{\partial}{\partial \rho} (\rho \kappa \frac{\partial T}{\partial \rho}) + \frac{\partial}{\partial y} (\kappa \frac{\partial T}{\partial y}) + q_{abs}, \quad (8.4)$$

with the boundary conditions

$$T = T_\infty \quad \text{at} \quad y = 0, \quad (8.5)$$

$$T = T_\infty \quad \text{at} \quad y = L, \quad (8.6)$$

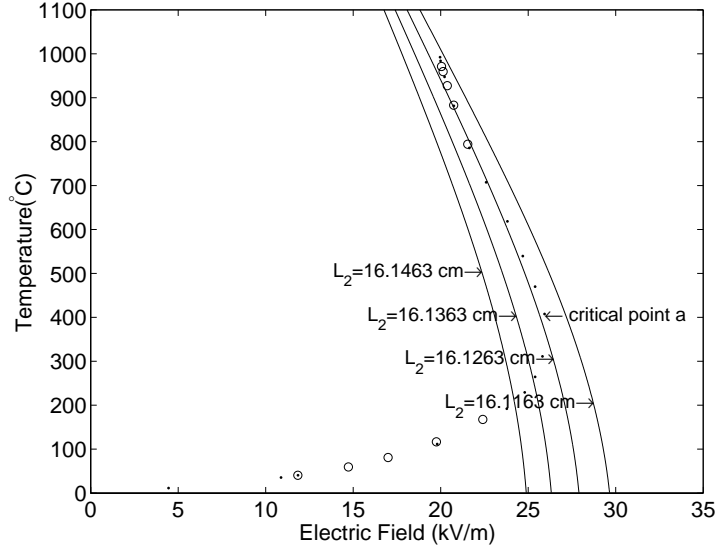


Figure 8.10: Behavior of electric field and temperature for decreasing cavity length; high power level, short position around critical point a .

$$-\kappa \frac{\partial T}{\partial \rho} = 0 \quad \text{at} \quad \rho = 0, \quad (8.7)$$

$$-\kappa \frac{\partial T}{\partial \rho} = \sigma \varepsilon (T^4 - T_{wall}^4) + h(T - T_{\infty}) \quad \text{at} \quad \rho = r, \quad (8.8)$$

and the initial condition

$$T = T_{\infty} \quad \text{at} \quad t = 0. \quad (8.9)$$

In the above equations, ρ_d , C_p , κ , and ε are the density, specific heat, thermal conductivity and emissivity of the material, respectively. T_{∞} and T_{wall} are ambient temperature and the temperature of the cavity wall. In the calculations, two temperatures are selected to be the same. σ is the Stefan-Boltzmann constant and h is the convective heat transfer coefficient. The definition of q_{abs} is given by Eq. (2.2). L is the length of the rod. The coordinate system is the same as that used in Chapter 7 when we solved the electric field in the rod.

Goodson^[29] incorporated all temperature-dependent properties into this two-dimensional model. He used a finite volume method to discretize these equations. The detailed description of this model can be found in his thesis. Our task is to incorporate the value of q_{abs} into his model.

We use the varying line source model to calculate the electric field in the rod; thus these two models do not match very well because the electromagnetic model is indeed one dimensional. However, as we discussed in Chapter 7, the variation of the electric field along the ρ direction is small. Therefore, we expect the results to be reasonably accurate.

8.2.1 S-shaped curve

Figs. 8.11 and 8.12 show the numerical results for heating of a mullite rod by decreasing the cavity length. The amplitude of the incident TE_{10} mode is set to 10 kV/m, which corresponds to 172 W output power of the generator. Fig. 8.11 shows a portion of an S-shaped curve which includes the lower and middle branches, which is similar to the experimental result shown in Fig. 5.3. By comparing Fig. 8.12 with Figs. 5.1 and 5.2, we see that reverse thermal runaway around the critical point b is successfully predicted by the numerical model.

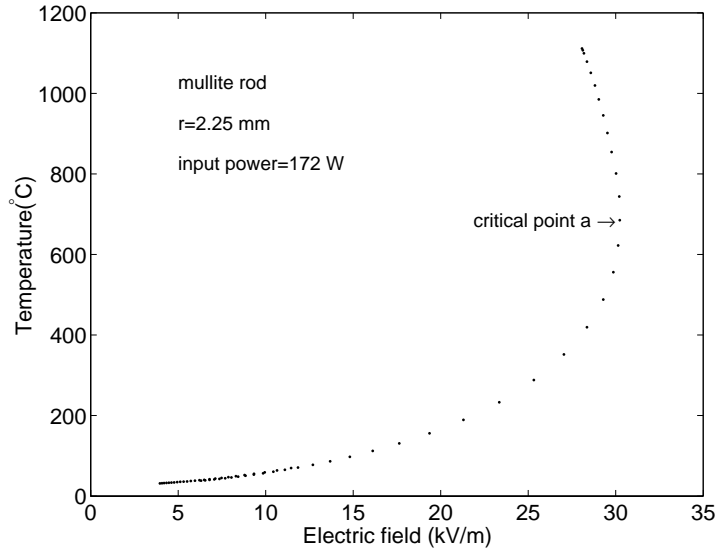


Figure 8.11: Numerical results for heating of a mullite rod by decreasing the cavity length : Electric field versus temperature.

However, several differences exist between the numerical and experimental results. First, the critical point a in the numerical results is at 700°C, which is a much

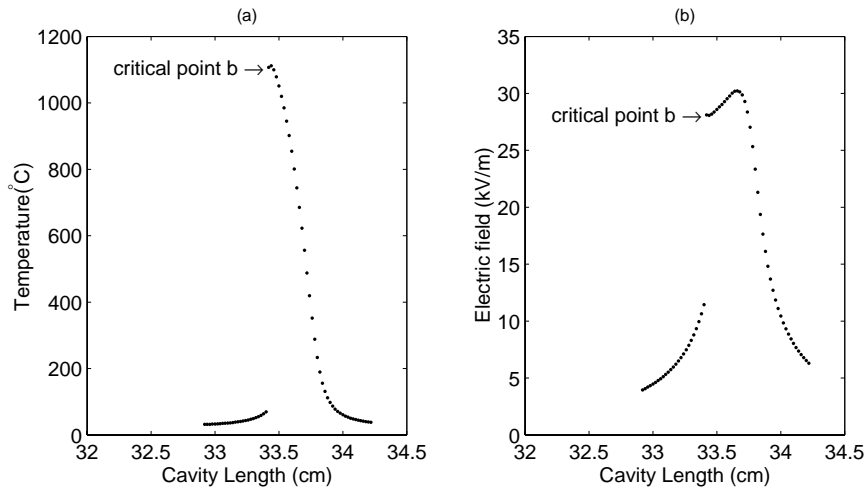


Figure 8.12: Numerical results for heating of a mullite rod by decreasing the cavity length : (a) Cavity length versus temperature. (b) Cavity length versus electric field.

higher temperature than that at the experimental critical point *a*, which is around 400°C. Secondly, it appears that the numerical model overestimates the required electric field to heat the rod to a specified temperature. Since all the points on the S-shaped curve represent equilibrium states, the S-shaped curve is mainly determined by the energy balance; thus we have solid reason to believe that the numerical value should be correct. Although an uncertain factor, emissivity, can affect both the numerical and experimental results, the effects are in the same direction. We attribute this difference to the inaccuracy of the electric field measurement. In the experiment, we cannot measure the electric field in the rod directly, thus we measure the electric field at a point one half wavelength away from the rod. As we discussed in Chapter 7, with the introduction of the rod in the cavity, the field is distorted. This can introduce large errors.

Figs. 8.13 and 8.14 show the numerical results for heating of a mullite rod by increasing the cavity length. The numerical results successfully predict the thermal excursion around the critical point *c*.

Fig. 8.15 shows the numerical results for heating of an alumina rod by decreasing the cavity length. The numerical results successfully predict a full S-shaped curve, as observed in the experiment.

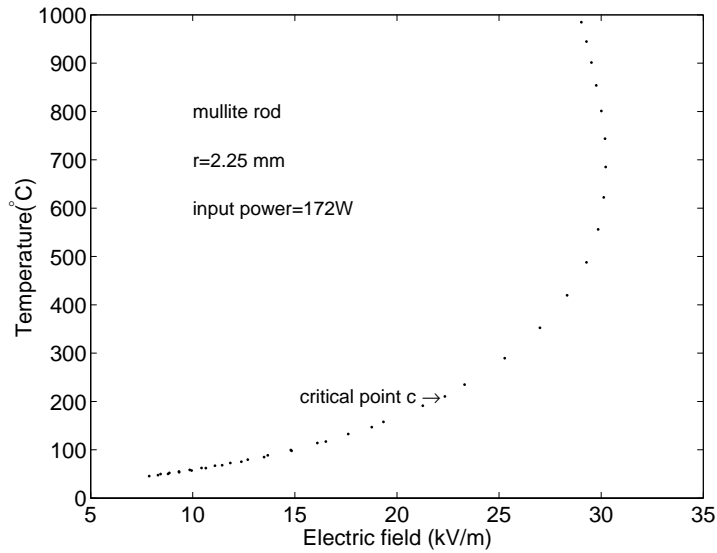


Figure 8.13: Numerical results for heating of a mullite rod by increasing the cavity length : Electric field versus temperature.

8.2.2 Temperature and electric field distribution in the rod

Fig. 8.16 shows the numerical prediction of the temperature distribution in an alumina rod with a radius of 2.25 mm. Along the ρ direction, the temperature varies less than 5% while along the y direction, the variation is more than 30%. Since we have selected the highest average temperature, the nonuniformity during the heating process will not exceed these two numbers.

Fig. 8.17 shows the corresponding electric field along the y direction. Although the temperature variation exceeds 30%, the variation of the electric field is less than 3%. The two humps in the electric field near the center of the figure may be due to numerical effects.

For comparison, we also show the temperature and electric field distribution in a rod with a diameter of 9 mm in Figs. 8.18 and 8.19. It appears that the variations of both the temperature and electric field along the y direction are similar to those of the thinner rod, while the temperature variation along the ρ direction increases to 9%.

Finally, the temperature along the whole rod is shown in Fig. 8.20.

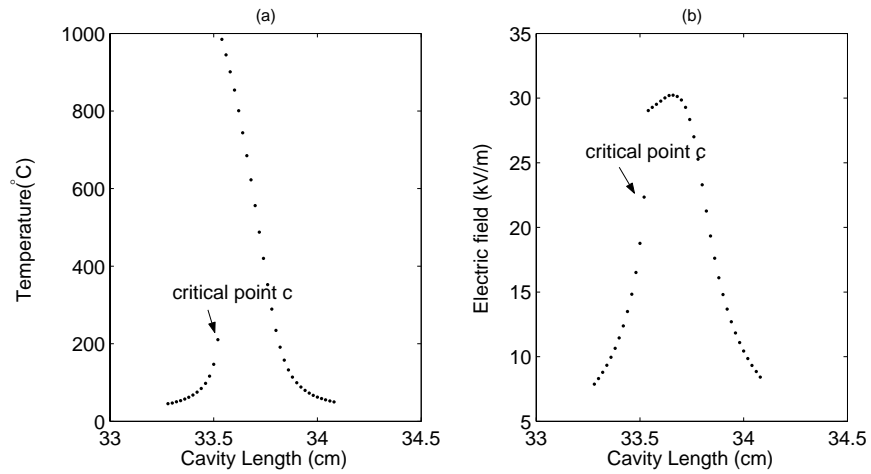


Figure 8.14: Numerical results for heating of a mullite rod by increasing the cavity length : (a) Cavity length versus temperature. (b) Cavity length versus electric field.

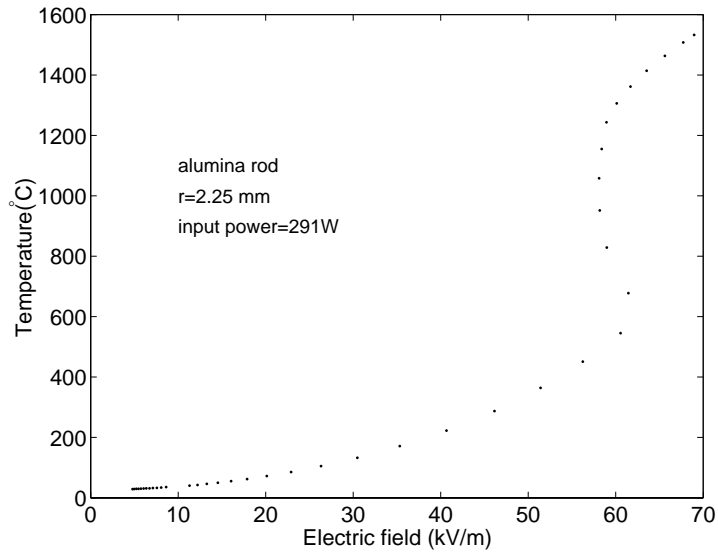


Figure 8.15: Numerical results for heating of an alumina rod by decreasing the cavity length : Electric field versus temperature.

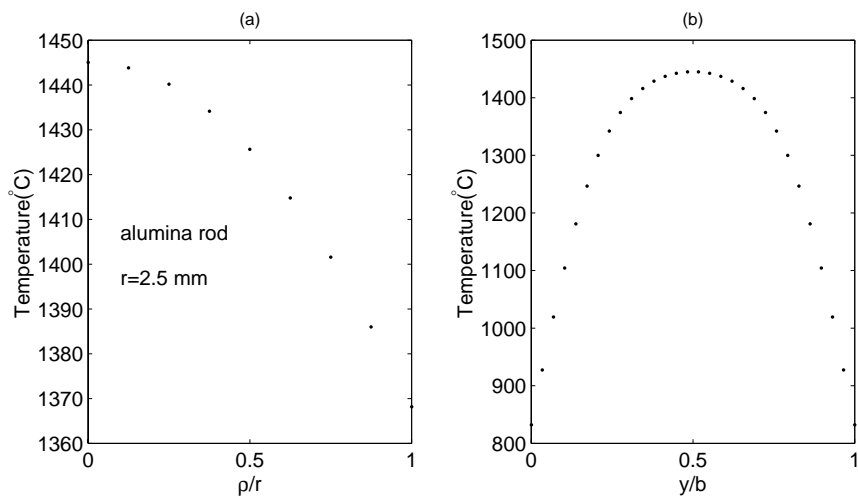


Figure 8.16: Numerical prediction of the temperature distribution in an alumina rod : (a) ρ direction (b) y direction.

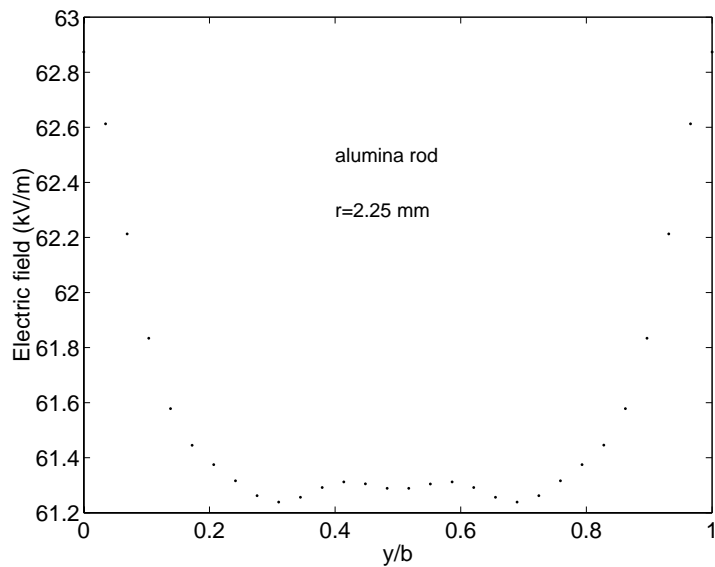


Figure 8.17: Numerical prediction of the electric field distribution in an alumina rod along the y direction.

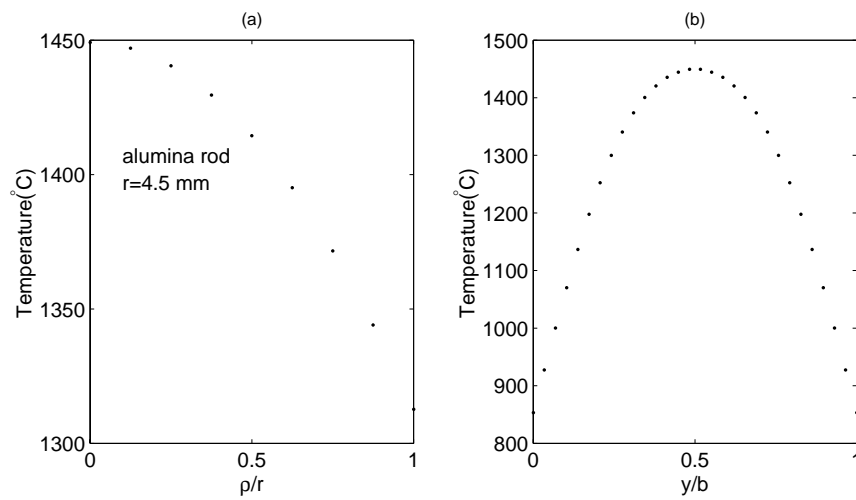


Figure 8.18: Numerical prediction of the temperature distribution in an alumina rod : (a) ρ direction (b) y direction.

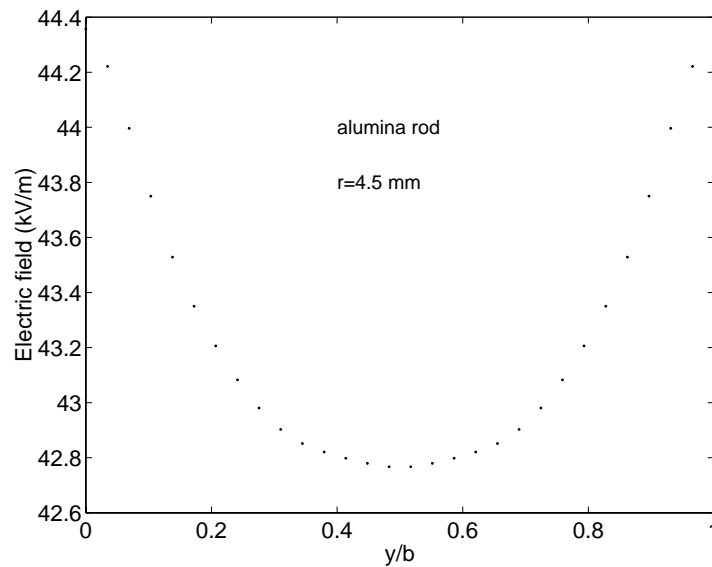


Figure 8.19: Numerical prediction of the electric field distribution in an alumina rod along the y direction.

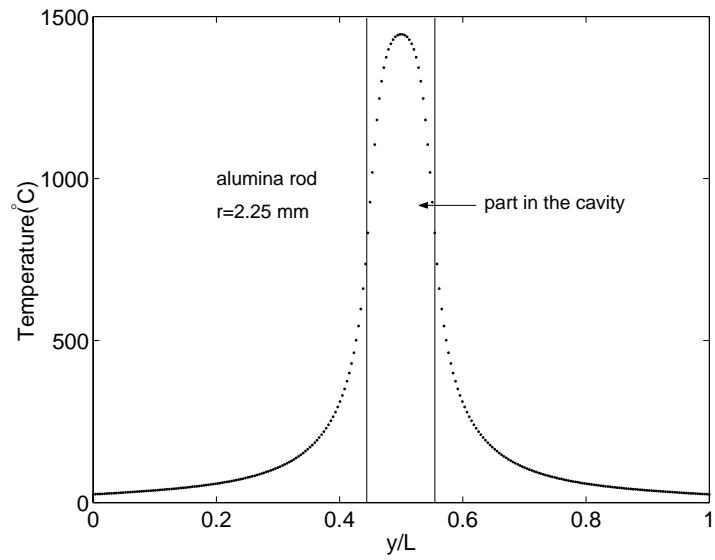


Figure 8.20: Numerical prediction of the temperature distribution in an alumina rod along the y direction.

Chapter 9

Summary, Conclusions and Recommendations

This dissertation has presented an experimental and numerical study of microwave heating of thermal runaway materials in a resonant cavity. Both experimental and numerical results show that thermal runaway materials can be successfully processed in the resonant cavity. This is mainly due to an intrinsic control system inherent to a resonant cavity. In this chapter, we will summarize our work and then give the conclusion and recommendations.

9.1 Summary

In Chapter 3, we discussed the factors which may affect the power absorption by materials. In microwave heating processes, the dielectric constant may change dramatically, thus our discussion is mainly focused on the variation effects of ε'_r and ε''_r . There are two mechanisms which can induce thermal runaway. First, the material could be in the resonant state due to the variation of ε'_r . Once in a resonant state, the fields in the material can be dramatically increased, thus the power absorption increases. The resonant states are determined by the combination of the dielectric

constant and the size of the material¹. Since a finite size material has discrete eigenvalues, resonance may occur with the variation of ε_r . When using microwaves to process small size ceramic materials, the size and the dielectric constant of the ceramic material assure that the material is far away from the first resonant state, thus thermal runaway is induced by a totally different mechanism. When materials with positive temperature dependence of dielectric loss are heated by microwaves, the absorbed power will increase if the electric field in the material does not change. Therefore, to avoid thermal runaway, the only choice is to control the electric field in the material.

In Chapter 5, we use experimental results to show a successful method to control thermal runaway in a resonant cavity. By decreasing the cavity length, we can make the heated rod be stabilized at any desired temperature, even in the middle branch of the S-curve, where the system is believed to be unstable.^[41] Our experimental results can be explained by Figs. 9.1 and 9.2.

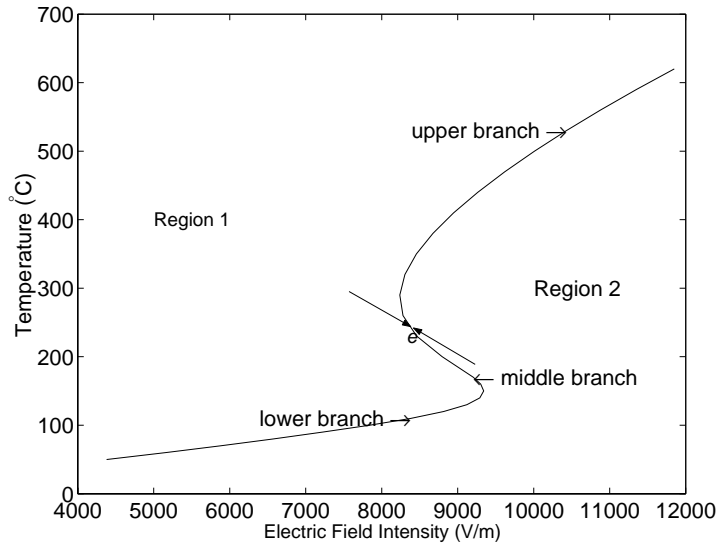


Figure 9.1: Stability analysis using both S-shaped curve and cavity effects

In Fig. 9.1, the whole E-T plane is divided by the S-shaped curve into two

¹When kd is the eigenvalue of the system governed by Maxwell's equations, resonance occurs, where k and d are the wavenumber and the characteristic length of the material, respectively. When we discuss wave problems, it is the value of kd rather than the individual value k or d that determine the state of the material.

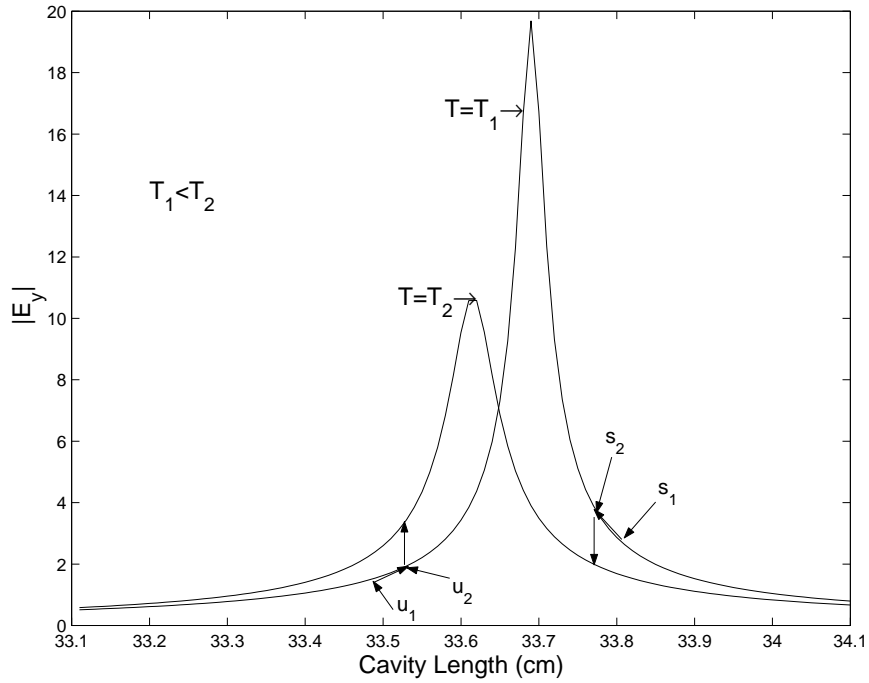


Figure 9.2: Different heating process

regions. In region 1, power absorbed is less than heat loss, thus the temperature tends to decrease while in region 2, power absorbed is larger than heat loss, and the temperature tends to increase. Every point on the S-shaped curve represents a thermally balanced state.

If we intend to heat the materials starting from any thermally balanced state, we must increase the electric field so that the material is in region 2. From Fig. 9.2, we see that we have two choices to increase the electric field. Supposing we choose point u_1 as a starting point, which is to the left of the peak value and on the T_1 curve, we must increase the cavity length to increase the electric field, thus the state point will move to u_2 immediately. Now the point is in region 2 and its temperature will increase. With increasing temperature, it is apparent that the electric field will increase, as shown in the process illustrated in Fig. 9.2. If the starting point is on the lower or higher branch of the S-curve, it is possible that the heating process ends at a neighboring thermally balanced state with higher temperature and electric field. However, if the starting point is around the critical point a , thermal runaway occurs

because the neighboring thermally balanced state with a higher temperature has a lower electric field.

To avoid thermal runaway, we must reach the resonance of the cavity through decreasing the cavity length. For example, if we choose point s_1 as an starting point, which is to the right of the peak value and on the T_1 curve, by decreasing the cavity length we can increase the electric field, and the state point will move to s_2 immediately. Starting from point s_2 , the electric field will decrease with increasing temperature. Depending on the position of the starting point, the value of the electric field at the end state might be either higher or lower than that of the starting point. Therefore, even if the heating process starts from the critical point a , it is still possible that the process ends at a neighboring thermally balanced state with a higher temperature and a lower electric field.

Once the processing point reaches the S-curve, it is in a stable state. If the processing point is in region 1 due to fluctuation, the temperature must decrease since absorbed power is less than heat loss, so the processing point returns to the equilibrium point on the S-shaped curve. If the processing point is in region 2, it also must return to the equilibrium point. Since the response time of the electromagnetic field is much smaller than that of the thermal process, the middle branch of the S-shaped curve is stable. Viewed from this perspective, there is no difference between the lower or middle branch of the S curve.

From the experimental results, it is clear that when investigating stability or instability of a system, all parameters must be considered. In our system, the electric field acts as an automatic feedback control if adjusting the short plane in the correct way. Since the response time of the electromagnetic field is so small, we believe this is a good control system. Fig. 9.3 shows the temperature *vs* time when the mullite rod was heated from 790°C to 990°C. This temperature change was produced simply by changing the cavity length, after which the system evolved automatically. For this system, 990°C is on the middle branch of the S-shaped curve.

The remaining problem is that of whether the processing point can reach the S-curve. Such a process is illustrated in Fig. 8.10, where even if the electric field

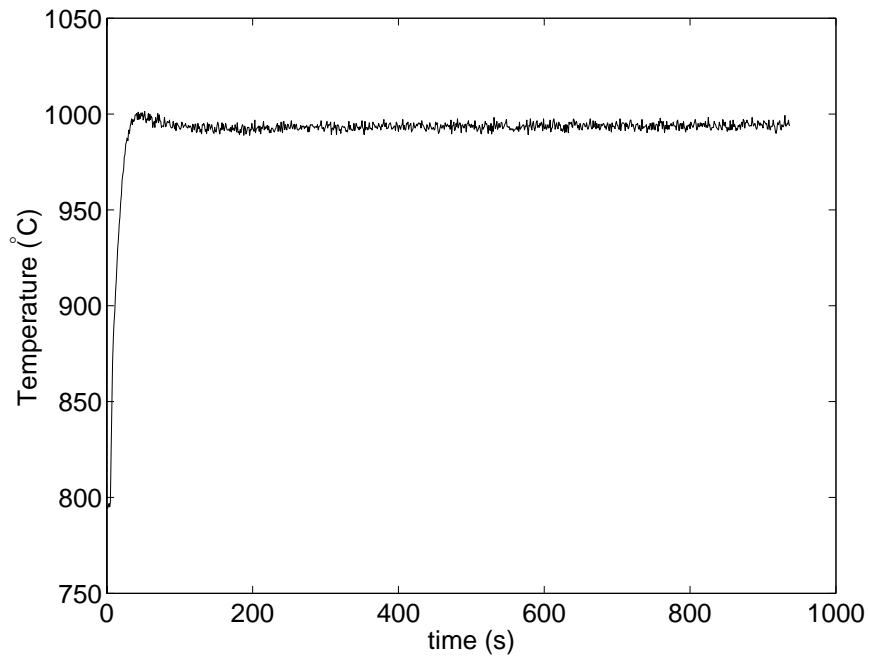


Figure 9.3: Temperature history for heating of a mullite rod with 4.5 mm diameter from 790°C to 990°C

decreases with increasing temperature, thermal runaway still occurs. This needs further study.

In Chapter 6, we developed an equivalent circuit model to simulate our experiment. Such a model has been widely used in microwave engineering. It can represent the key points of the heating process in a simple form. One advantage of this model is that the measurements can be easily incorporated into the model because all elements in the heating system are represented by the lumped parameters. Our current model includes only the cavity part, thus when we use this model to explain the experimental results, some unrealistic assumptions have to be made. For example, we assumed that the incident power was a constant during the heating process. Actually, even if the output power of the generator is set to a constant, the incident power measured in the waveguide varies. It is expected that with the extension of the current model to include more components in the heating system, it can predict the heating process more accurately.

In chapter 7, we developed a numerical model to calculate the electric field in

the cavity by dividing the cavity into the iris part and the rod part. If the shape of the iris is regular, mode matching techniques are believed to be the most accurate method to calculate the reflection coefficient. For a nonregular shaped iris, the finite element method has to be used. Since we used a commercial software package, we had to use an inefficient method to calculate the iris problem. For the scattering problem in the electromagnetic field, it is always more efficient to convert the problem into the integral form before discretization, thus a finite element method based on the integral equation is recommended in future studies. When calculating the electric field in the rod, we used the OEM and line source methods to handle the rod with constant and varying properties in the y direction. The line source model can give reasonable results for the electric field in the rod; however, due to its assumption that the radius of the rod is zero, sometimes it can give incorrect results for the reflection coefficient of the rod. An improvement of this method is expected by incorporating the line source concept into the OEM method. As discussed in Chapter 7, by the use of the two term approximation, the electric field along the ρ and ϕ directions can be accurately predicted; thus the electric field can be assumed in a form with known variation along ρ and ϕ but with unknown coefficients which is dependent on y . By replacing the line source with this type of source, it is expected that the model can predict the fields and reflection coefficient more precisely.

In Chapter 8, we incorporated the electric field model into the heat transfer model. The numerical results can quantitative simulate the heating process. It successfully predict the S-curve and the thermal instability. However, the difference is obvious when comparing with the experimental results. This difference comes from both experimental measurement and numerical calculation. In the experiment, we use two one-color pyrometers to measure the temperature in different ranges. It is observed that the readings from two pyrometers may have a up to 200°C difference. It is expected that a two-color pyrometer can be used to measure the temperature. In the numerical model, the heat loss along the waveguide, on the iris and short plane should be included. This could be done by incorporating the measured data into the model.

9.2 Conclusions

From this study, we can conclude that:

1. The S-curve is a real phenomenon, and not an artifact. It is a valid theory to explain thermal runaway occurring in microwave heating.
2. The middle branch of the S-curve is stable if a resonant cavity is used as an applicator to process thermal runaway materials. Considering both the energy balance and the cavity effects, it is clear that unstable processes are due to the incorrect operation and incomplete understanding of microwave heating phenomenon in a resonant cavity.
3. In a resonant cavity, thermal runaway can be controlled without an automatic control system. Adjusting the short plane correctly can avoid thermal runaway, at least for mullite and alumina heated in a resonant cavity.
4. Most important phenomena of microwave heating in a resonant cavity can be explained by an equivalent circuit model in a simple form.
5. A coupled heat transfer and electromagnetic field model can quantitatively predict microwave heating processes in a resonant cavity.

9.3 Recommendations

Based on this study, we recommend that:

1. To efficiently heat materials with different sizes and properties, an iris whose dimensions can be varied during the experiment is necessary.
2. The temperature measurement accuracy must be improved. A two-color pyrometer is a good solution.
3. The numerical model used to calculate the electric field in the rod should be improved to include the electric field variation along both ρ and y direction.

Bibliography

- [1] K. G. Ayappa and H. T. Davis. Microwave heating: An evaluation of power formulations. *Chemical Engineering Science*, 46(4):1005–1016, 1991.
- [2] C. A. Balanis. *Advanced Engineering Electromagnetics*. John Wiley & Sons, Inc., 1989.
- [3] G. O. Beale and F. J. Arteaga. Automatic control to prevent thermal runaway during microwave joining of ceramics. In Beatty et al. [5], pages 265–270.
- [4] G. O. Beale and M. Li. Robust temperature control for microwave heating of ceramics. *IEEE Transactions on Industrial Electronics*, 44(1):124–131, 1997.
- [5] R. L. Beatty, W. H. Sutton, and M. F. Iskander, editors. *Microwave Processing of Materials III, Materials research society symposium proceedings*, volume 269, 1992.
- [6] D. W. Bible, R. J. Lauf, and C. A. Everleigh. Multikilowatt variable frequency microwave furnace. In Beatty et al. [5], pages 77–81.
- [7] J. V. Bladel. *Singular Electromagnetic Fields and Sources*. Oxford University Press, 1995.
- [8] S. M. Bond. Microwave-assisted processing - from laboratory to production. In D. E. Clark, J. G. P. Binner, and D. A. Lewis, editors, *Microwaves: Theory and Application in Materials Processing V, Ceramic Transactions*, volume 111, pages 489–496, 2000.

- [9] Y. V. Bykov, K. I. Rybakov, and V. E. Semenov. High-temperature microwave processing of materials. *Journal of Physics D-Applied Physics*, 34(13):R55–R75, 2001.
- [10] C. Canuto, M. Y. Hussaini, A. Quarteroni, and T. A. Zang. *Spectral Methods in Fluid Dynamics*. Springer-Verlag, 1988.
- [11] I. J. Chabinsky. Applications of microwave energy past, present and future “brave new world”. In Sutton et al. [73], pages 17–32.
- [12] J. Cheng, R. Roy, and D. Agrawal. Radically different effects on materials by separated microwave electric and magnetic fields. *Mat. Res. Innovat.*, 5:170–177, 2002.
- [13] A. Cherradi, G. Desgardin, J. Provost, and B. Raveau. Electric and magnetic field contribution to the microwave sintering of ceramics. In *Electroceramics IV: Fourth International Conference on electronic ceramic & Applications Proceedings*, volume 2, pages 1219–1224, 1994.
- [14] D. E. Clark, F. D. Gac, and W. H. Sutton, editors. *Microwaves: Theory and Application in Materials Processing*, *Ceramic Transactions*, volume 21, 1991.
- [15] D. E. Clark, W. H. Sutton, and D. A. Lewis. Microwave processing of materials. In Clark et al. [16], pages 61–98.
- [16] D. E. Clark, W. H. Sutton, and D. A. Lewis, editors. *Microwaves: Theory and Application in Materials Processing IV*, *Ceramic Transactions*, volume 80, 1997.
- [17] D. E. Clark, W. R. Tinga, and J. R. Laia, Jr., editors. *Microwaves: Theory and Application in Materials Processing II*, *Ceramic Transactions*, volume 36, 1993.
- [18] R. E. Collin. *Field Theory of Guided Waves*. IEEE Press, 1991.
- [19] J. M. Curtis, Jr. Experimental verification for microwave processing of materials in a single mode rectangular resonant cavity. Master’s thesis, Virginia Polytechnic Institute and State University, 1999.

- [20] M. L. D. Stuerger. Far beyond small perturbations. *Journal of Microwave Power and Electromagnetic Energy*, 28(2):73–83, 1993.
- [21] D. Dadon, D. Gershon, Y. Carmel, K. I. Rybakov, R. Hutcheon, A. Birman, L. P. Martin, J. Calame, B. Levush, and M. Rosen. Observation of an electromagnetically driven temperature wave in porous zinc oxide during microwave heating. In Iskander et al. [35], pages 507–512.
- [22] W. A. Davis. Private Communication, 2001.
- [23] A. De, I. Ahmad, E. D. Whitney, and D. E. Clark. Microwave (hybrid) heating of alumina at 2.45 ghz: I. microstructural uniformity and homogeneity. In Clark et al. [14], pages 319–328.
- [24] M. D. Deshpande. Analysis of discontinuities in a rectangular waveguide using dyadic green’s function approach in conjunction with method of moments. Technical report, NASA Contractor Report 201692, 1997.
- [25] R. S. Elliott. *An introduction to guided waves and microwave circuits*. Prentice Hall, 1993.
- [26] H. Fukushima, T. Yamanaka, and M. Matsui. Microwave heating of ceramics and its application to joining. In Sutton et al. [73], pages 267–272.
- [27] C. Gellings. Dielectric heating: Epri’s perspective on the market and the technology. In Clark et al. [16], pages 27–39.
- [28] R. Gesche and N. Lochel. Scattering by a lossy dielectric cylinder in a rectangular waveguide. *IEEE Transactions on Microwave Theory and Techniques*, 36(1):137–144, 1988.
- [29] C. C. Goodson. Simulation of microwave heating of mullite rods. Master’s thesis, Virginia Polytechnic Institute and State University, 1997.

- [30] N. Gupta, V. Midha, V. Balakotaiah, and D. J. Economou. Bifurcation analysis of thermal runaway in microwave heating of ceramics. *Journal of the Electrochemical Society*, 146(12):4659–4665, 1999.
- [31] R. F. Harrington. *Time-Harmonic Electromagnetic Fields*. McGraw-Hill Inc., 1961.
- [32] R. F. Harrington. Matrix methods for field problems. *Proceedings of the IEEE*, 55(2):136–149, 1967.
- [33] R. F. Harrington. *Field Computation by Moment Methods*. IEEE Press, 1993.
- [34] K. Huie. Private Communication, 2000.
- [35] M. F. Iskander, J. O. Kiggans, Jr., and J.-C. Bolomey, editors. *Microwave Processing of Materials V, Materials research society symposium proceedings*, volume 430, 1996.
- [36] M. F. Iskander, R. J. Lauf, and W. H. Sutton, editors. *Microwave Processing of Materials IV, Materials research society symposium proceedings*, volume 347, 1994.
- [37] H. W. Jackson, M. Barmatz, and P. Wagner. Transient temperature behavior of a sphere heated by microwaves. In Clark et al. [17], pages 189–199.
- [38] M. A. Janney and H. D. Kimrey. Diffusion-controlled processes in microwave-fired oxide ceramics. In Snyder et al. [66], pages 215–228.
- [39] M. A. Janney, H. D. Kimrey, and J. O. Kiggans. Microwave processing of ceramics: Guidelines used at the oak ridge national laboratory. In Beatty et al. [5], pages 173–185.
- [40] H. D. Kimrey and M. A. Janney. Design principles for high-frequency microwave cavities. In Clark et al. [14], pages 367–372.
- [41] G. A. Kriegsmann. Thermal runaway in microwave heated ceramics: A one-dimensional model. *Journal of Applied Physics*, 71(4):1960–1966, 1992.

- [42] G. A. Kriegsmann. Hot spot formation in microwave heated ceramic fibres. *IMA Journal of Applied Mathematics*, 59(2):123–148, 1997.
- [43] G. A. Kriegsmann. Pattern formation in microwave heated ceramics: Cylinders and slabs. *IMA Journal of Applied Mathematics*, 66(1):1–32, 2001.
- [44] S. W. Lee, W. R. Jones, and J. J. Campbell. Convergence of numerical solutions of iris-type discontinuity problems. *IEEE Transactions on Microwave Theory and Techniques*, MTT-19(6):528–536, 1971.
- [45] L. Lewin. *Theory of waveguides*. John Wiley & Sons, Inc., New York, 1968.
- [46] L. Lewin. On the inadequacy of discrete mode-matching techniques in some waveguides discontinuity problems. *IEEE Transactions on Microwave Theory and Techniques*, MIT-18:364–372, 1970.
- [47] X. P. Liang and K. A. Zaki. Modeling of cylindrical dielectric resonators in rectangular waveguides and cavities. *IEEE Transactions on Microwave Theory and Techniques*, 41(12):2174–2181, 1993.
- [48] N. Marcuvitz. *Waveguide Handbook*. Peter Peregrinus Ltd., 1986.
- [49] P. H. Masterman and P. J. B. Clarricoats. Computer field-matching solution of waveguide transverse discontinuities. *Proceedings of the IEE*, 118(1):51–63, Jan 1971.
- [50] B. McConnell. A coupled heat transfer and electromagnetic model for simulating microwave heating of thin dielectric materials in a resonant cavity. Master’s thesis, Virginia Polytechnic Institute and State University, 1999.
- [51] S. L. McGill, J. W. Walkiewicz, and G. A. Smyres. The effects of power level on the microwave heating of selected chemicals and minerals. In Clark et al. [14], pages 247–252.
- [52] A. C. Metaxas and R. J. Meredith. *Industrial Microwave Heating*. Peter Peregrinus, Ltd., London, 1988.

- [53] A. F. Mills. *Heat transfer*. Richard D. Irwin, Inc., 1992.
- [54] M. Mongiardo and T. Rozzi. Singular integral equation analysis of flange-mounted rectangular waveguide radiators. *IEEE Transactions on Antennas and Propagation*, 41(5):556–565, May 1993.
- [55] M. M. Ney. Method of moments as applied to electromagnetic problems. *IEEE Transactions on Microwave Theory and Techniques*, MTT-33(10):972–980, 1985.
- [56] P. E. Parris and V. M. Kenkre. Thermal runaway in ceramics arising from the temperature dependence of the thermal conductivity. *Physica Status Solid I B-Basic Research*, 200(1):39–47, 1997.
- [57] J. A. Pelesko and G. A. Kriegsmann. Microwave heating of ceramic laminates. *Journal of Engineering Mathematics*, 32:1–18, 1997.
- [58] D. M. Pozar. *Microwave Engineering*. John Wiley & Sons, Inc., second edition, 1998.
- [59] G. Roussy, A. Bennani, and J. M. Thiebaut. Temperature runaway of microwave irradiated materials. *Journal of Applied Physics*, 62(4):1167–1170, 1987.
- [60] G. Roussy and J. Mercier. Temperature runaway of microwave heated materials: Study and control. *Journal of Microwave Power*, 20(1):47–51, 1985.
- [61] G. Roussy and J. A. Pearce. *Foundations and industrial applications of microwaves and radio frequency fields*. John Wiley & Sons Ltd, England, 1995.
- [62] R. Roy, D. Agrawal, J. Cheng, and S. Gedevanishvili. Full sintering of powdered-metal bodies in a microwave field. *Nature*, 399:668–670, 1999.
- [63] R. F. Schiffmann. Understanding microwave reactions and interactions. <http://www.foodproductdesign.com/archive/1993/0493DE.html>, April 1994.
- [64] J. Schwinger and D. S. Saxon. *Discontinuities in waveguide: notes on lectures by Julian Schwinger*. Gordon and Breach Science Publishers, New York, NY, 1968.

- [65] R. D. Smith. Present and future uses of microwave power. In Snyder et al. [66], pages 383–390.
- [66] W. B. Snyder, Jr., W. H. Sutton, M. F. Iskander, and D. L. Johnson, editors. *Microwave Processing of Materials II, Materials research society symposium proceedings*, volume 189, 1990.
- [67] M. S. Spatz, D. J. Skamser, and D. L. Johnson. Thermal-stability of ceramic materials in microwave-heating. *Journal of the American Ceramic Society*, 78(4):1041–1048, 1995.
- [68] D. F. Stein, R. H. Edgar, M. F. Iskander, D. L. Johnson, S. M. Johnson, C. G. Lob, J. M. Shaw, W. H. Sutton, P. K. Tien, and T. E. Munns. Microwave processing - an emerging industrial technology. In Iskander et al. [36], pages 3–7.
- [69] W. H. Sutton. Microwave firing of high alumina castables. In Sutton et al. [73], pages 287–295.
- [70] W. H. Sutton. Microwave processing of ceramic materials. *The American Ceramic Society Bulletin*, 68(2):376–386, 1989.
- [71] W. H. Sutton. Microwave processing of ceramics-an overview. In Beatty et al. [5], pages 3–20.
- [72] W. H. Sutton. Key issues in microwave technology. In Clark et al. [17], pages 3–18.
- [73] W. H. Sutton, M. H. Brooks, and I. J. Chabinsky, editors. *Microwave Processing of Materials, Materials research society symposium proceedings*, volume 124, 1988.
- [74] C. T. Tai. *Dyadic Green Functions in Electromagnetic theory*. IEEE Press, second edition, 1994.
- [75] N. D. Terril. Field simulation for the microwave heating of thin ceramic fibers. Master’s thesis, Virginia Polytechnic Institute and State University, 1998.

- [76] J. R. Thomas, Jr., J. M. Curtis, Jr., C. H. Stern, and W. A. Davis. Controlled microwave heating of thermal runaway materials. In D. E. Clark, D. C. Folz, S. J. Oda, and R. Silbergliitt, editors, *Microwaves: Theory and Application in Materials Processing III*, *Ceramic Transactions*, volume 59, pages 345–354, 1995.
- [77] J. R. Thomas, Jr., C. C. Goodson, C. H. Stern, M. Jackson, and G. J. Vogt. Microwave sintering of ceramic rods: Experiments and models. *Journal of Microwave Power and Electromagnetic Energy*, 33(2):113–120, 1998.
- [78] J. R. Thomas, Jr., E. M. Nelson, R. J. Kares, and R. M. Stringfield. Temperature distribution in a flowing fluid heated in a microwave resonant cavity. In Iskander et al. [35], pages 565–569.
- [79] J. R. Thomas, Jr., W. P. Unruhnd, and G. J. Vogt. Mathematical model of thermal spikes in microwave heating of oxide ceramics fibers. In Iskander et al. [36], pages 363–368.
- [80] Y. L. Tian, D. L. Johnson, and M. E. Brodwin. Ultrafine microstructure of Al_2O_3 produced by microwave sintering. In G. L. Messing, E. R. Fuller, Jr., and H. Hausner, editors, *Ceramic Powder Science II*, pages 925–932, 1987.
- [81] V. K. Varadan, Y. Ma, A. Lakhtakia, and V. V. Varadan. Microwave sintering of ceramics. In Sutton et al. [73], pages 45–57.
- [82] G. J. Vogt, W. P. Unruhnd, and J. R. Thomas, Jr. Experimental observations of thermal spikes in microwave heating of oxide ceramics fibers. In Iskander et al. [36], pages 539–544.
- [83] C. A. Vriezanga. Thermal runaway and bistability in microwave heated isothermal slabs. *Journal of Applied Physics*, 79(3):1779–1783, 1996.
- [84] C. A. Vriezanga. Thermal runaway in microwave heated isothermal slabs, cylinders, and spheres. *Journal of Applied Physics*, 83(1):438–442, 1998.

- [85] C. A. Vriezinger. Thermal profiles and thermal runaway in microwave heated slabs. *Journal of Applied Physics*, 85(7):3774–3779, 1999.
- [86] C. A. Vriezinger. Thermal runaway in microwave heated slabs of foodstuffs and ceramics: A comparison. In *7th International Conference on Microwave and High Frequency Heating*, pages 453–456, 1999.
- [87] J. J. H. Wang. *Generalized Moment Methods in Electromagnetics: Formulation and computer solution of integral equations*. John Wiley & Sons, Inc., 1991.
- [88] A. Wexler. Solution of waveguide discontinuities by modal analysis. *IEEE Transactions on Microwave Theory and Techniques*, MTT-15(9):508–517, 1967.
- [89] X. Wu, J. R. Thomas, Jr., and W. A. Davis. Control of thermal runaway in microwave resonant cavity. *Journal of Applied Physics*, 92(6):3374–3380, 2002.
- [90] R. Yang and A. S. Omar. Rigorous analysis of iris coupling problems in waveguide. *IEEE Transactions on Microwave Theory and Techniques*, 41(2):349–352, 1993.
- [91] H. W. Yao, K. A. Zaki, A. E. Atia, and R. Hershtig. Full wave modeling of conducting posts in a rectangular waveguides and its applications to slot coupled combline filters. *IEEE Transactions on Microwave Theory and Techniques*, 43(12):2824–2830, 1995.
- [92] Y. Yin, J. Binner, and T. Cross. Microwave assisted chemical vapour infiltration for ceramic matrix composites. In Clark et al. [16], pages 349–356.
- [93] X. L. Zhang, D. O. Hayward, and D. M. P. Mingos. Microwave dielectric heating behavior of supported mos_2 and pt catalysts. *Industrial and Engineering Chemistry Research*, 40(13):2810–2817, 2001.

Vita

The author, Xiaofeng Wu, son of Shen Wu and Duohua Liu, was born on December 27, 1970, in Beijing, China. He obtained his Bachelor of Science and Master of Science in Thermal Engineering Department in Tsinghua University in 1995 and 1998, respectively. He then went on to Virginia Polytechnic Institute and State University, in Blacksburg, Virginia, where he earned a Ph.D. in Mechanical Engineering in 2002.

Permanent Address: 826-202, ZhongGuanCun,
100080, Beijing, China

This dissertation was typeset with $\text{\LaTeX} 2_{\epsilon}^2$ by the author.

² $\text{\LaTeX} 2_{\epsilon}$ is an extension of \LaTeX . \LaTeX is a collection of macros for \TeX . \TeX is a trademark of the American Mathematical Society. The macros used in formatting this dissertation were written by Greg Walker, Department of Mechanical Engineering, Virginia Tech.